Lie Group Analysis, Direct Numerical Simulation and Wavelet Analysis of a Turbulent Channel Flow Rotating about the Streamwise Direction

Vom Fachbereich Maschinenbau
an der Technischen Universität Darmstadt

zur
Erlangung des Grades eines Doktor-Ingenieurs (Dr.-Ing.)
genehmigte

Dissertation

vorgelegt von

Dipl.-Ing. Tanja Weller
aus Mainz

Berichterstatter:	Prof. Dr.-Ing. M. Oberlack
Mitberichterstatter:	Prof. Dr. rer. nat. M. Schäfer
Tag der Einreichung:	28.11.2006
Tag der mündlichen Prüfung:	24.01.2007

D17
Darmstadt, 2007

Abstract

In this thesis turbulent channel flow with streamwise rotation has been investigated by means of an analytical and a numerical method.
First investigations were done in 1998 by Oberlack employing the symmetry group theory. Oberlack showed that there is a new turbulent scaling law related to the turbulent channel flow rotating about the mean flow direction. The induction of a cross flow in the spanwise direction is the most obvious difference compared to the classical case, rotation about the spanwise direction.

Established on these results the new scaling law was derived using Lie group analysis of the two-point correlation equations. Further it was shown that all six components of the Reynolds stress tensor are non-zero.

To verify these effects a Direct Numerical Simulation was performed. The influence of the rotation was studied at three different Reynolds numbers ($Re_\tau = 180$, 270 and 560) and at a variety of different rotation rates. Both the induced cross flow and the fact that the six components of the Reynolds stress tensor are non-zero could be verified. In addition a significant decay of the streamwise maximum velocity between $Ro = 5.2$ and 10 was noticed. At the same time the cross flow reaches a maximum at about $Ro = 10$ and then decreases for higher rotation rates. These observations are called *rotation drag effect* (RDE).

Furthermore a Wavelet analysis was performed to obtain more insight into the RDE and the corresponding structural effects. Therefore the *coherent vortex extraction* (CVE) method was applied to six selected three-dimensional DNS data sets at $Re_\tau = 180$. The compression rate as well as the enstrophy of the coherent vorticity component show a noticeable reverse between $Ro = 5.2$ and 10. This tendency is supported by the skewness and the flatness of the coherent vorticity component. In general the results confirm a significant change in the flow dynamics.

Kurzfassung

In dieser Arbeit wird mit Hilfe einer analytischen und einer numerischen Methode eine turbulente um die Hauptströmungsrichtung rotierende Kanalströmung untersucht.
Erste Studien wurden 1998 von Oberlack mit der Symmetrie-Gruppen Theorie unternommen. Oberlack zeigte, dass für die um die Hauptströmungsrichtung rotierende turbulente Kanalströmung ein neues turbulentes Skalengesetz existiert. Die Induktion einer Querströmung um die Querachse ist der offensichtlichste Unterschied zum klassischen Fall, der Rotation um die Querachse.

Aufbauend auf diesen Ergebnissen wurde das neue Skalengesetz mit Hilfe der Lie-Gruppen Analysis der Zwei-Punkt Korrelationsgleichungen hergeleitet. Weiter wurde gezeigt, dass alle sechs Komponenten des Reynoldschen Spannungstensors ungleich Null sind.

Um diese Effekte zu verifizieren, wurden Direkte Numerische Simulationen durchgeführt. Der Einfluss der Rotation wurde an drei verschieden Reynoldszahlen (Re_τ = 180, 270 and 560) und einer Serie von verschiedenen Rotationszahlen untersucht. Sowohl die induzierte Querströmung als auch die Tatsache, dass alle sechs Komponenten des Reynoldschen Spannungstensors ungleich Null sind, konnte nachgewiesen werden. Zusätzlich wurde gezeigt, dass die maximale Geschwindigkeit in Strömungsrichtung einen signifikanten Abfall zwischen den Rotationszahlen $Ro = 5.2$ und 10 aufweist. Gleichzeitig erreicht die Querströmung einen maximalen Wert bei ca. $Ro = 10$ and fällt für höhere Rotationszahlen wieder ab. Diese Beobachtungen werden *rotation drag effect* (RDE) genannt.

Weiterhin wurde eine Wavelet Analyse durchgeführt, um weitergehende Einsicht in den RDE und die dazugehörigen strukturellen Effekte zu bekommen. Zu diesem Zweck wurde die *coherent vortex extraction* (CVE) Methode auf sechs ausgewählte dreidimensionale DNS Datensätze bei einer Reynoldszahl von $Re_\tau = 180$ angewandt. Sowohl die Kompressionsrate als auch die Enstrophy der kohärenten Wirbelkomponenten weisen eine deutliche Umkehrung zwischen den Rotationsraten $Ro = 5.2$ und 10 auf. Diese Tendenz untermauern die Schiefe und die Kurtosis der kohärenten Wirbelkomponenten. Allgemein bestätigen diese Ergebnisse einen signifikanten Wechsel in der Strömungsdynamik.

Acknowledgements

First of all I would like to thank my supervisor Prof. Dr.-Ing. M. Oberlack for accepting me as his PhD student and for his valuable and interesting discussions during my work in his group. His scientific support and everyday encouragement helped me to finish this work. I would also like to thank Prof. Dr. rer. nat. M. Schäfer, who agreed to be my co-referee.

I am thankful to Prof. M. Farge from the Ecole Normale Supérieure in Paris, France and Prof. K. Schneider from the Université de Provence in Marseille, France, who made their wavelet code available for me and gave me a first introduction. I would like to thank specially K. Schneider for all of the numerous discussions during the visits and phone calls.

A special thank to the Deutsche Forschungsgemeinschaft (DFG) for its financial support, making my work at all possible.

I would like to express my gratitude to the support teams from HHLR, TU Darmstadt and NIC, Jülich, who helped me to run the code on the IBM supercomputers. I express my gratitude to both for their continuing help during my work on the project.

Thanks also to my colleagues who have always contributed to a great working environment. Special thanks to George, Jörg, Michael and Norma, who agreed to proofread my thesis.

Finally, I would like to address my sincere gratitude to my boy friend and my parents for their patience and respect.

Contents

List of Figures

List of Tables

Nomenclature

$\bar{u}_1$	streamwise mean velocity,
$\bar{u}_3$	spanwise mean velocity,
ϵ	rate of kinetic energy dissipation,
η	Kolmogorov scale,
ν	kinematic viscosity,
$\overline{u'_i u'_j}$	Reynolds Stress Tensor,
$R_{i(jk)}, R_{(ik)j}$	triple correlations,
$R_{ij}(\boldsymbol{x}, \boldsymbol{r}, t)$	two-point correlation tensor,
Re_τ	Reynolds number based on u_τ,
Ro	rotation number based on u_τ,
U_1	mean bulk velocity,
u_τ	friction velocity,
$\boldsymbol{r}(r_1, r_2, r_3)$	vector in correlation space,
$\boldsymbol{x}(x_1, x_2, x_3)$	vector in physical space,
$\overline{p' u'_j}$	pressure-velocity two-point correlations,
$\overline{u'_j p'}$	velocity-pressure two-point correlations,
$\frac{\bar{D}}{Dt}$	mean substantial derivative,
CL	centerline,
CR	Compression rate,
CVE	Coherent Vortex Extraction,
DNS	Direct Numerical Simulation,
FFT	Fast Fourier Transform,
FWT	Fast Wavelet Transform,

MPC	Multi-Point correlation,
MRA	Multi-Resolution Analysis,
PIV	Particle-Image Velocimetry technique,
RANS	Reynolds-averaged Navier-Stokes,
RDE	Rotation drag effect,
S	skewness,
sim.	simulation,
T	flatness,
TPC	Two-Point Correlation,
WR	wall region,
Z	Enstrophy,

1 Introduction

1.1 The Phenomena of Turbulence

Turbulence or turbulent flow is characterized by chaotic, stochastic property changes. This includes low momentum diffusion, high momentum convection as well as rapid variation of pressure and velocity in space and time. The opposite of turbulent flow is laminar flow. The condition leading to laminar or turbulent flow can be determined by the Reynolds number.

In turbulent flow, unsteady vortices appear on many scales and interact with each other. Drag due to boundary layer skin friction increases. The structure and location of boundary layer separation often changes, sometimes resulting in a reduction of overall drag. Because laminar-turbulent transition is governed by the Reynolds number, the same transition occurs if e.g. the size of the object is gradually increased, the viscosity of the fluid is decreased, or the density of the fluid is increased.

Although the mathematical basic equations to describe turbulence were derived independently more than 150 years ago from the French mathematician and physician Claude L.M.H. Navier (1775-1836) and the Irish mathematician and physician George G. Stokes (1819-1903), turbulence remains an important unsolved problem of classical physics. During the last centuries, a lot of researchers worked on this problem. To mention are e.g. Leonardo da Vinci (1452-1519), Osborne Reynolds (1842-1912), Ludwig Prandtl (1875-1953), Theodor von Kármán (1881-1963) and Werner Heisenberg (1901-1976) to name only a few.

Turbulence occurs nearly everywhere, where fluid flow is present: in the oceans, in the atmosphere, in rivers, even in stars and galaxies. In general, turbulent motions are very common in nature. In fact it is easier to find a turbulent flow than a flow that is really laminar. In figures 1.1-1.4 four examples are displayed. Fig. 1.1 shows turbulent swirls and eddies in a fast flowing river, while in fig. 1.2 turbulence is observed in the ash plume of the Mt. Spurr volcano as it erupts. Further in fig. 1.3 turbulent air currents in the atmosphere is visualized and in 1.4 the highly turbulent outer layer of the sun, i.e. the convection zone.

Figure 1.1: Fast flowing river.

Figure 1.2: Mt. Spurr volcano.

Figure 1.3: Atmosphere.

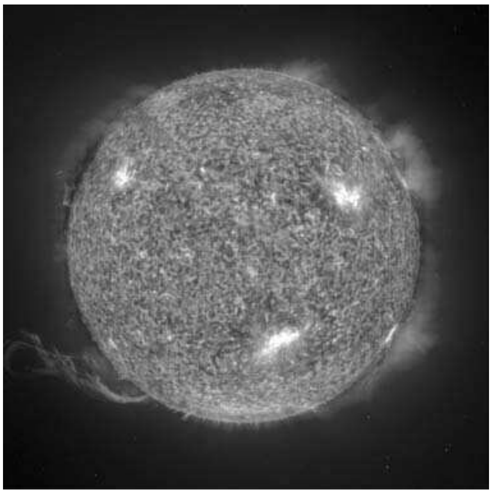

Figure 1.4: Sun.

Turbulence is not only common in nature, it exits also in our everyday life. Four ordinary example are:

- Stirring the milk in the coffee already releases a turbulent flow. Turbulence arises if liquids or gases are moved fast.
- A pot of boiling water. By heating a fluid at the bottom and cooling it at the top the fluid becomes turbulent due to convection.
- The smoke rising from a cigarette. For the first few centimeters it remains laminar, and then it becomes unstable and hence turbulent.
- Flow over a golf ball. If the golf ball were smooth, the boundary layer flow over the front of the sphere would be laminar at typical conditions. However, the boundary layer would separate early, as the pressure gradient switched

from favorable to unfavorable, creating a large region of low pressure behind the ball that creates high form drag. To prevent this from happening, the surface is dimpled to perturb the boundary layer and promote transition to turbulence. This leads to a delayed separation and hence to less form drag.

Turbulence occurs also in the industry. Examples are:

- A jet exhausting from a nozzle into a quiescent fluid. As the flow emerges into this external fluid, shear layers originating at the lips of the nozzle are created. These layers separate the fast moving jet from the external fluid, and at a certain critical Reynolds number they become unstable and break down to turbulence.
- The flow conditions in many industrial equipment, such as pipes, ducts, precipitators, gas scrubbers, etc. and machines, for instance, internal combustion engines and gas turbines.
- The external flow over all kind of vehicles such as cars, airplanes, ships and submarines.

1.2 Motivation

The influence of rotation on turbulent flows is significant. Such flows are of considerable interest in a variety of geophysical and astrophysical applications. Today rotating turbulent flows play more a major role in engineering applications such as in gas turbine blade passages, pumps and rotating heat echangers to name only a few.

In contrast our prediction ability is still rather limited particularly when computing turbulent flows based on Reynolds-averaged Navier-Stokes (RANS) solvers using two-equation models with linear stress-strain relation. As a matter of fact, even higher-order turbulence models such as second-moment closure models disclose serious deficiencies, even though to a lower extent since they explicitly contain Coriolis terms.

Some extensive research has been done experimentally and numerically concerning rotating channel flows. Back in the 70s experimental observations of channel flow rotating about the spanwise axis were undertaken by Hart (1971) and Johnston, Halleen & Lezius (1972), while early numerical analyses of this flow were conducted by Kristoffersen & Andersson (1993) or Tafti & Vanka (1991).

Both numerical and experimental data show a strong influence of the rotation on the main flow profile, which experiences a strong deformation and becomes asymmetric. The investigation of the fluctuation properties of the rotating flow evidences a distinct decrease of the turbulence on the 'suction' side of the channel, while on the 'pressure' side the turbulence level is augmented.

Rotation about the streamwise direction in channel flows has experienced intensive study only recently. First investigations of Oberlack, Cabot & Rogers (1998) employing the symmetry group theory showed, that there is a new turbulent scaling law related to the turbulent channel flow rotating about the mean flow direction. Fig. 1.5 explains the flow geometry.

The flow has several common features with the classical rotating channel flow (Johnston et al. 1972) but also has some different characteristics. The induction of a mean velocity in x_3-direction is the most obvious difference compared to the classical case. This cross flow can be deduced by investigating the mean momentum equation and the Reynolds stress transport equation.

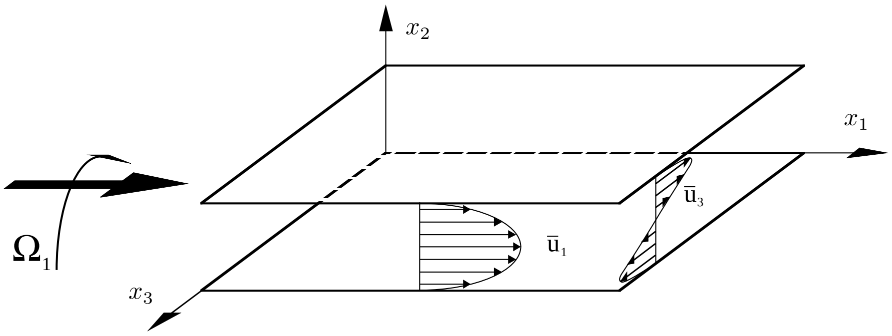

Figure 1.5: Sketch of the flow geometry of a turbulent channel flow rotating about the mean flow direction.

To verify the theoretical results a joint project was established. One part of the project is the Direct Numerical Simulation (DNS) of a turbulent channel flow rotating about the streamwise direction, which is the main subject of this thesis. The second part of the project is the experimental examination of the same flow geometry conducted by Aerodynamisches Institut, RWTH Aachen, Germany. A comparison of the results is also discussed in this work.

The thesis is organized as follows: In the next chapter the governing equations, which are the Navier-Stokes equations, the Reynolds averaged Navier-Stokes equations and the two-point correlation equations are given. Chapter 3 gives a short introduction into Lie-Group Analysis and presents the new scaling law related to the present flow geometry. In chapter 4 the results of Direct Numerical Simulations are discussed. The chapter is divided into two parts. The first part presents results for different rotations rates at Reynolds number $Re_\tau = 180$. In the second part the previous results are compared these at higher Reynolds numbers of $Re_\tau = 270$ and $Re_\tau = 560$. In chapter 5 coherent structures and their statistics are studied. Finally the results are summarized in chapter 6 and relevant conclusions are indicated.

2 Basic Equations

2.1 Navier-Stokes and Euler Equations

The Navier-Stokes equations, named after Claude-Louis Navier and George Gabriel Stokes, are a set of equations that describe the motion of a fluid. The assumption of incompressibility implies that the Mach number is low and the temperature variations negligible. The Navier-Stockes equations correspond to the Euler equation in the case of $\nu = 0$. The continuity equation can be written as:

$$\frac{\partial u_k}{\partial x_k} = 0 \tag{2.1}$$

and the momentum equation:

$$\frac{Du_i}{Dt} = -\frac{1}{\rho}\frac{\partial p}{\partial x_i} + \nu\frac{\partial^2 u_i}{\partial x_k \partial x_k} - 2\Omega_k e_{ikl} u_l \tag{2.2}$$

with

$$\frac{D}{Dt} = \frac{\partial}{\partial t} + u_k \frac{\partial}{\partial x_k}, \tag{2.3}$$

where t and $\boldsymbol{x}$ are time and coordinates in space. $\boldsymbol{u}$, p, ρ, ν and Ω_k are respectively the instantaneous velocity vector, pressure, density, kinematic viscosity and the rotation vector. e_{ikl} is an antisymmetric tensor of third rank, which is denoted permutation tensor.

The permutation tensor e_{ikl} is defined by:

$$e_{ikl} = \begin{cases} 1, & \text{for} \qquad ijk = 123, 312, 231 \\ -1, & \text{for} \qquad ijk = 321, 132, 213 \\ 0, & \text{otherwise} \end{cases} \tag{2.4}$$

Together with the continuity equation, the Navier-Stokes equations yield a system of four equations with four unknowns, namely pressure and three velocity components. Thus, the system of equations (2.1) and (2.2) is closed. Unfortunately, this does not automatically guarantee that the solutions to those equations satisfy the given physics. In fact, it is not even guaranteed a priori that a satisfactory solution exists, see Foias, Manley, Rosa & Temam (2001). It is very important to know the nature of the solutions to the Navier-Stokes equations because the equations must be solved by numerical methods and the nature of the solutions directly influences, which type of method will be most effective.

2.2 Reynolds averaged Navier-Stokes Equations

In engineering applications as well as for the statistical descriptions the mean values for the velocities and the pressure are under focus. Therefore the instantaneous quantities are decomposed into mean and fluctuating components. The Reynolds decomposition can be rewritten as follows:

$$\boldsymbol{u} = \bar{\boldsymbol{u}} + \boldsymbol{u}', \quad p = \bar{p} + p' \tag{2.5}$$

The quantities marked with a bar denote the mean quantities, while the quantities marked with primes are the fluctuations. The average is in general build as:

$$\bar{u} = \lim_{N\to\infty} \big(\frac{1}{N}\sum_{n=1}^{N} u_n\big), \quad \bar{p} = \lim_{N\to\infty} \big(\frac{1}{N}\sum_{n=1}^{N} p_n\big) \tag{2.6}$$

Introducing the Reynolds decomposition (2.5) into (2.1) and (2.2) and averaging gives the Reynolds averaged continuity

$$\frac{\partial \bar{u}_k}{\partial x_k} = 0 \tag{2.7}$$

and momentum equations

$$\frac{\bar{D}\bar{u}_i}{\bar{D}t} = -\frac{\partial \bar{p}}{\partial x_i} + \nu \frac{\partial^2 \bar{u}_i}{\partial x_k \partial x_k} - 2\Omega_k e_{ikl}\bar{u}_l - \frac{\partial \overline{u_i' u_k'}}{\partial x_k}. \tag{2.8}$$

After averaging the advection term in the momentum equations, the so called Reynolds stress tensor is obtained:

$$\overline{u_i'u_k'} = \begin{pmatrix} \overline{u_1'u_1'} & \overline{u_1'u_2'} & \overline{u_1'u_3'} \\ \overline{u_1'u_2'} & \overline{u_2'u_2'} & \overline{u_2'u_3'} \\ \overline{u_1'u_3'} & \overline{u_2'u_3'} & \overline{u_3'u_3'} \end{pmatrix}. \tag{2.9}$$

The Reynolds stress tensor is responsible for the turbulent exchange of the momentum due to the fluctuating motion. Because of this term, the system of equations (2.7) and (2.8) is unclosed. It is possible to derive an exact transport equation for the Reynolds stress tensor in the following form (see (Oberlack 2000)):

$$\begin{aligned} \frac{\partial \overline{u_i'u_j'}}{\partial t} + \bar{u}_k \frac{\partial \overline{u_i'u_j'}}{\partial x_k} &= -\overline{u_i'u_k'}\frac{\partial \bar{u}_j}{\partial x_k} - \overline{u_j'u_k'}\frac{\partial \bar{u}_i}{\partial x_k} - 2\nu \overline{\frac{\partial u_i'}{\partial x_k}\frac{\partial u_j'}{\partial x_k}} + \overline{\frac{p'}{\rho}\Big(\frac{\partial u_i'}{\partial x_j} + \frac{\partial u_j'}{\partial x_i}\Big)} \\ &+ \frac{\partial}{\partial x_k}\Big[- \overline{u_i'u_j'u_k'} + \nu \frac{\partial \overline{u_i'u_j'}}{\partial x_k} - \overline{\frac{p'}{p}(\delta_{kj}u_i' + \delta_{ki}u_j')}\Big] - 2\Omega_k\Big[e_{kli}\overline{u_j'u_l'} + e_{klj}\overline{u_i'u_l'}\Big] \end{aligned} \tag{2.10}$$

or introducing abbreviated notations:

$$\begin{aligned} P_{ij} &= -\Big[\overline{u_i'u_k'}\frac{\partial \bar{u}_j}{\partial x_k} - \overline{u_j'u_k'}\frac{\partial \bar{u}_i}{\partial x_k}\Big], \\ \epsilon_{ij} &= \nu \overline{\frac{\partial u_i'}{\partial x_k}\frac{\partial u_j'}{\partial x_k}}, \\ \Phi_{ij} &= \overline{\frac{p'}{p}\Big(\frac{\partial u_i'}{\partial x_j} + \frac{\partial u_j'}{\partial x_i}\Big)}, \\ D_{ij}^t &= -\frac{\partial \overline{u_i'u_j'u_k'}}{\partial x_k}, \\ D_{ij}^\nu &= \nu \frac{\partial^2 \overline{u_i'u_j'}}{\partial x_k \partial x_k}, \\ D_{ij}^p &= -\frac{\partial}{\partial x_k}\Big[\overline{\frac{p'}{\rho}(\delta_{kj}u_i' + \delta_{ki}u_j')}\Big], \\ C_{ij} &= -2\Omega_k\Big[e_{kli}\overline{u_j'u_l'} + e_{klj}\overline{u_i'u_l'}, \Big] \end{aligned} \tag{2.11}$$

where P_{ij} represents the energy production, ϵ_{ij} the dissipation, Φ_{ij} the pressure strain correlation, D_{ij} the diffusion (turbulent, molecular and pressure diffusion) and C_{ij} the Coriolis term. Because the dissipation, pressure strain correlation and turbulent diffusion (pressure and triple term diffusion) term are unknown, further equations are necessary.

2.3 Multi- and Two-Point Correlation Equations

Because of the complex nature of turbulent flows, sometimes it is an advantage to study multi-point statistics. The motion of any point in a turbulent flow affects the motion at other distant points through the pressure field. For this reason an adequate description cannot be obtained by considering only mean values associated with single fluid particles. To obtain a proper description of a turbilent flow it is necessary to consider two or more fluid particles at two or more positions. The multi-point correlation (MPC) equations can be used for studying the spatial configurations of the flow field. The MPC is suitable to model statistical quantities of turbulence at all scales. To write the MPC equations in a compact form we introduce the definition

$$R_{i_{n+1}} = R_{i_{(0)} i_{(1)} \dots i_{(n)}} = \overline{u'_{i_{(0)}}(\boldsymbol{x}_{(0)}) \cdot \dots \cdot u'_{i_{(n)}}(\boldsymbol{x}_{(n)})} \tag{2.12}$$

at $n+1$ points, where $u'_{i_{(k)}}$ denotes velocity fluctuations about the mean velocity $\bar{u}_{i_{(k)}}$ at the point $\boldsymbol{x}_{(k)}$.

Including the definition of equation (2.12) it is possible to derive the MPC equations from the Navier-Stokes equations (Oberlack 2000)

$$\begin{aligned}
\Theta_{i_{\{n+1\}}} =& \frac{\partial R_{i_{\{n+1\}}}}{\partial t} + \sum_{l=0}^{n} \Bigg[\bar{u}_{k_{(l)}}(\boldsymbol{x}_{(l)}) \frac{\partial R_{i_{\{n+1\}}}}{\partial x_{k_{(l)}}} + R_{i_{\{n+1\}}[i_{(l)} \mapsto k_{(l)}]} \frac{\partial \bar{u}_{i_{(l)}}(\boldsymbol{x}_{(l)})}{\partial x_{k_{(l)}}} \\
&+ \frac{\partial P_{i_{\{n\}}[l]}}{\partial x_{i_{(l)}}} - \nu \frac{\partial^2 R_{i_{\{n+1\}}}}{\partial x_{k_{(l)}} \partial x_{k_{(l)}}} - R_{i_{\{n\}}[i_{(l)}] \mapsto \emptyset} \frac{\partial \overline{u'_{i_{(l)}} u'_{k_{(l)}}}(\boldsymbol{x}_{(l)})}{\partial x_{k_{(l)}}} \\
&+ \frac{\partial R_{i_{\{n+2\}}[i_{(n+1)} \mapsto k_{(l)}]}[\boldsymbol{x}_{(n+1)} \mapsto \boldsymbol{x}_{(l)}]}{\partial x_{k_{(l)}}} + 2 \Omega_k e_{i_{(l)} k m} R_{i_{\{n+1\}}[i_{(l)} \mapsto m]} \Bigg] = 0 \\
&\text{for} \quad n = 1, \dots, \infty.
\end{aligned} \tag{2.13}$$

by using the additional definitions

$$\begin{aligned}
&R_{i_{\{n+1\}}[i_{(l)} \mapsto k_{(l)}]} = \\
&\qquad \overline{u'_{i_{(0)}}(\boldsymbol{x}_{(0)}) \cdot \dots \cdot u'_{i_{(l-1)}}(\boldsymbol{x}_{(l-1)}) u'_{k_{(l)}}(\boldsymbol{x}_{(l)}) u'_{i_{(l+1)}}(\boldsymbol{x}_{(l+1)}) \cdot \dots \cdot u'_{i_{(n)}}(\boldsymbol{x}_{(n)})},
\end{aligned} \tag{2.14}$$

$$R_{i_{\{n+2\}}[i_{(n+1)} \mapsto k_{(l)}]}[\boldsymbol{x}_{(n+1)} \mapsto \boldsymbol{x}_{(l)}] = \overline{u'_{i_{(0)}}(\boldsymbol{x}_{(0)}) \cdot \dots \cdot u'_{i_{(n)}}(\boldsymbol{x}_{(n)}) u'_{k_{(l)}}(\boldsymbol{x}_{(l)})}, \tag{2.15}$$

$$R_{i_{\{n\}}[i_{(l)}\mapsto\emptyset]} = \overline{u'_{i_{(0)}}(\boldsymbol{x}_{(0)})\cdot\ldots\cdot u'_{i_{(l-1)}}(\boldsymbol{x}_{(l-1)})u'_{i_{(l+1)}}(\boldsymbol{x}_{(l+1)})\cdot\ldots\cdot u'_{i_{(n)}}(\boldsymbol{x}_{(n)})}, \qquad (2.16)$$

and

$$P_{i_n[l]} = \overline{u'_{i_{(0)}}(\boldsymbol{x}_{(0)})\cdot\ldots\cdot u'_{i_{(l-1)}}(\boldsymbol{x}_{(l-1)})p'(\boldsymbol{x}_{(l)})u'_{i_{(l+1)}}(\boldsymbol{x}_{(l+1)})\cdot\ldots\cdot u'_{i_{(n)}}(\boldsymbol{x}_{(n)})}, \qquad (2.17)$$

The notation in the square brackets denotes the replacement of certain variables or indices with some other quantities standing on the right side of the arrow. Each Θ-equation of the tensor oder $n+1$ only contains one unclosed term of the order n+2. For any of the remaining terms (Oberlack 2000), e.g. $P_{i_n[l]}$, exact equations can be derived from the continuity equation or the Poisson equation for the pressure.

The Two-point correlation (TPC) tensor admits two additional identities,

$$\lim_{x_{(k)}\to x_{(l)}} R_{i_{\{2\}}} = \lim_{x_{(k)}\to x_{(l)}} R_{i_{(0)}i_{(1)}} = \overline{u'_{i_{(0)}}u'_{i_{(1)}}}(\boldsymbol{x}_{(l)}) \text{ with } k \neq l \qquad (2.18)$$

where $x_{(k)}$ and $x_{(l)}$ can be an arbitrary position vector taken from $x_{(0)},...,x_{(n)}$ and the null identity

$$R_{i_{\{1\}}[i_{(l)}\mapsto\emptyset]} = 0. \qquad (2.19)$$

The latter is traced back to the fact that the average of a single fluctuating velocity is zero.

The following two sets of equations are derived from the continuity equation, which have to be employed as additional kinematic constrains

$$\frac{\partial R_{i_{\{n+1\}}[i_{(l)}\mapsto i_{(l)}]}}{\partial x_{k_{(l)}}} \text{ for } l = 0,...,n \qquad (2.20)$$

and

$$\frac{\partial P_{i_{\{n\}}[k][i_{(l)}\mapsto m_{(l)}]}}{\partial x_{m_{(l)}}} \text{ for } k,l = 0,...,n \text{ and } k \neq l. \qquad (2.21)$$

For simplification it will be continued with the TPC equations. The TPC equations have a similar structure as the full set of MPC equations, particularly they have the same symmetry properties. In order to simplify the notation, the following short form is introduced

$$R_{i_{\{2\}}} = R_{ii_{\{1\}}} = R_{ij}. \tag{2.22}$$

For the derivation of the TPC equations the transport equation for the turbulent fluctuating velocities at the point $\boldsymbol{x}$ is multiplied with the fluctuyting velocity at the point $\boldsymbol{x}_1$ and vice versa. In the case of adding the resulting equations together, we obtain (Rotta 1972)

$$\begin{aligned}
\Theta_{i_{\{2\}}} =& \frac{\bar{D}R_{ij}}{\bar{D}t} + R_{kj}\frac{\partial \bar{u}_i(\boldsymbol{x},t)}{\partial x_k} + R_{ik}\frac{\partial \bar{u}_j(\boldsymbol{x},t)}{\partial x_k}\Bigg|_{\boldsymbol{x}+\boldsymbol{r}} \\
&+[\bar{u}_k(\boldsymbol{x}+\boldsymbol{r},t) - \bar{u}_k(\boldsymbol{x},t)]\frac{\partial R_{ij}}{\partial r_k} + \frac{\partial \overline{p'u'}_j}{\partial x_i} - \frac{\partial \overline{p'u'}_j}{\partial r_i} + \frac{\partial \overline{u_i'p'}}{\partial r_j} \\
&-\nu\left[\frac{\partial^2 R_{ij}}{\partial x_k \partial x_k} - 2\frac{\partial^2 R_{ij}}{\partial x_k \partial r_k} + \frac{\partial^2 R_{ij}}{\partial r_k \partial r_k}\right] \\
&+\frac{\partial R_{(ik)j}}{\partial x_k} - \frac{\partial}{\partial r_k}[R_{(ik)j} - R_{i(jk)}] + 2\Omega_k\Big[e_{kli}R_{lj} + e_{klj}R_{il}\Big] = 0,
\end{aligned} \tag{2.23}$$

where the difference beetween two points has been introduced according to

$$\boldsymbol{x} = \boldsymbol{x}_{(0)}, \quad \boldsymbol{r} = \boldsymbol{x}_{(1)} - \boldsymbol{x}_{(0)}. \tag{2.24}$$

$\frac{\bar{D}}{\bar{D}t} = \left(\frac{\partial}{\partial t} + \bar{u}_k\frac{\partial}{\partial x_k}\right)$ is the mean substantial derivative. $\boldsymbol{x}$ and $\boldsymbol{r}$ are coordinates in physical and correlation spaces respectively.

The fluctuating pressure-velocity vectors are special cases of $P_{i_{\{n\}}[k]}$ and are specified as

$$\overline{p'u_j'}(\boldsymbol{x},\boldsymbol{r},t) = \overline{p'(\boldsymbol{x},t)u_j'(\boldsymbol{x}+\boldsymbol{r},t)}, \quad \overline{u_i'p'}(\boldsymbol{x},\boldsymbol{r},t) = \overline{u_i'(\boldsymbol{x},t)p_j'(\boldsymbol{x}+\boldsymbol{r},t)}, \tag{2.25}$$

while the triple correlation vectors respectively defined as

$$R_{(ik)j} = \overline{u_i'(\boldsymbol{x},t)u_k'(\boldsymbol{x},t)u_j'(\boldsymbol{x}+\boldsymbol{r},t)}, \quad R_{i(jk)} = \overline{u_i'(\boldsymbol{x},t)u_j'(\boldsymbol{x}+\boldsymbol{r},t)u_k'(\boldsymbol{x}+\boldsymbol{r},t)}. \tag{2.26}$$

For the TPC equations case the continuity equations (2.20) and (2.21) simplify to

$$\frac{\partial R_{ij}}{\partial x_i} - \frac{\partial R_{ij}}{\partial r_i} = 0, \quad \frac{\partial R_{ij}}{\partial r_j} = 0, \quad \frac{\partial \overline{p' u_i'}}{\partial r_i} = 0, \quad \frac{\partial \overline{u_j' p'}}{\partial x_j} - \frac{\partial \overline{u_j' p'}}{\partial r_j} = 0. \tag{2.27}$$

The TPC tensor is defined as

$$R_{ij}(\boldsymbol{x}, \boldsymbol{r}, t) = \overline{u_i'(\boldsymbol{x}, t) u_j'(\boldsymbol{x} + \boldsymbol{r}, t)}. \tag{2.28}$$

3 Lie Group Analysis

3.1 Introduction

Sophus Lie made major advances in the theory of continuous groups of transformations and differential equations. His investigation led to one of the major branches of 20th-century mathematics, the theory of Lie groups and Lie algebras, which are named after him.

Sophus Lie, born 1842 in Nordfjordeide, Norway, studied science at the University of Kristiania (now Oslo). His interest in geometry deepened in 1868 and resulted in his first mathematical paper being published in Crelle's Journal in 1869.

In 1871 Lie became an assistant tutor at Kristiania and submitted his doctoral dissertation on the theory of contact transformations. In 1872 he became professor in Kristiania and began to research continuous transformation groups in 1873. In 1986 he was appointed as a professor in Leipzig. In collaboration with Friedrich Engel, he published *Theory of Transformation Groups* (1888-1893), which contains his investigations of the general theory of continuous groups.

In 1898 Lie returned to Kristiania to accept a special professor post created for him, where he died soon after his arrival. Besides his development of transformation groups, he made contributions to differential geometry. His primary aim, however, was the advancement of the theory of differential equations.

3.2 Symmetries of Differential Equations

A symmetry of a system of differential equations is a transformation that maps any solution to another solution of the system. These groups constitute an important tool in the development in a series of mathematical and physical areas. In engineering applications Lie group analysis is rather unknown. A detailed introduction is given by Oberlack (2000).

Furthermore, a short introduction into the topic is given here. A system of partial differential equations is given by:

$$\boldsymbol{F}(\boldsymbol{x}, \boldsymbol{y}, \boldsymbol{y}^{(1)}, \boldsymbol{y}^{(2)}, ...) = 0 \tag{3.1}$$

where $\boldsymbol{x}$ are the independent and $\boldsymbol{y}$ the dependent variables. A transformation

$$\boldsymbol{x}^* = \boldsymbol{\Phi}(\boldsymbol{x}, \boldsymbol{y}) \qquad \boldsymbol{y}^* = \boldsymbol{\Psi}(\boldsymbol{x}, \boldsymbol{y}) \tag{3.2}$$

is called a symmetry transformation of equation (3.1) if

$$\boldsymbol{F}(\boldsymbol{x}, \boldsymbol{y}, \boldsymbol{y}^{(1)}, \boldsymbol{y}^{(2)}, ...) = 0 \Longleftrightarrow \boldsymbol{F}(\boldsymbol{x}^*, \boldsymbol{y}^*, \boldsymbol{y}^{*(1)}, \boldsymbol{y}^{*(2)}, ...) = 0 \tag{3.3}$$

holds. $\boldsymbol{y}^{(n)}$ refers to the set of all n^{th} order derivatives of $\boldsymbol{y}$ with respect to $\boldsymbol{x}$.

The intention of the symmetry analysis is to find all Lie symmetries

$$\boldsymbol{x}^* = \boldsymbol{\Phi}(\boldsymbol{x}, \boldsymbol{y}; \varepsilon), \qquad \boldsymbol{y}^* = \boldsymbol{\Psi}(\boldsymbol{x}, \boldsymbol{y}; \varepsilon), \tag{3.4}$$

where ε is called the group parameter. Since ε may take any value $\varepsilon \in \boldsymbol{R}$, equation (3.4) is also called continuous group.

Lie's first theorem shows, that if a transformation has group properties it can be represented by its infinitesimal form, which still contains the essential information. This means, that the transformation can be expanded for the small parameter of the transformation:

$$\boldsymbol{x}^* = \boldsymbol{x} + \varepsilon \boldsymbol{\xi}(\boldsymbol{x}, \boldsymbol{y}) + \mathcal{O}(\varepsilon^2), \tag{3.5}$$

$$\boldsymbol{y}^* = \boldsymbol{y} + \varepsilon \boldsymbol{\eta}(\boldsymbol{x}, \boldsymbol{y}) + \mathcal{O}(\varepsilon^2), \tag{3.6}$$

where

$$\boldsymbol{\xi}(\boldsymbol{x}, \boldsymbol{y}) = \left. \frac{\partial \boldsymbol{\Phi}}{\partial \varepsilon} \right|_{\varepsilon=0}, \quad \boldsymbol{\eta}(\boldsymbol{x}, \boldsymbol{y}) = \left. \frac{\partial \boldsymbol{\Psi}}{\partial \varepsilon} \right|_{\varepsilon=0}. \tag{3.7}$$

If the infinitesimal of a transformation is given, their global form can be determined by integrating the first order system using Lie's first theorem (Bluman & Anco 2002):

$$\frac{d\boldsymbol{x}^*(\varepsilon)}{d\varepsilon} = \boldsymbol{\xi}(\boldsymbol{x}^*(\varepsilon), \boldsymbol{y}^*(\varepsilon)), \qquad \frac{d\boldsymbol{y}^*(\varepsilon)}{d\varepsilon} = \boldsymbol{\eta}(\boldsymbol{x}^*(\varepsilon), \boldsymbol{y}^*(\varepsilon)) \tag{3.8}$$

with the initial conditions:

$$\varepsilon = 0 : \boldsymbol{x}^*(\varepsilon) = \boldsymbol{x} \text{ and } \boldsymbol{y}^*(\varepsilon) = \boldsymbol{y}.$$

The advantage of symmetry groups is its algorithm nature. Thus, a variety of software packages are available to find continuous symmetry groups for essentially every differential equation. In the following section 3.4 the software package of Carminati & Vu (2000) is used to obtain symmetry groups for the present flow geometry.

3.3 Invariant Solutions

Invariant solution can be derived from the symmetries of a differential equation. $\boldsymbol{y} = \boldsymbol{\Theta}(\boldsymbol{x})$ is an invarinat solution of a diffential equation if $(\boldsymbol{y} - \boldsymbol{\Theta})(\boldsymbol{x})$ is an invariant function with respect to prolongation of the operator X, which is given by

$$X = \xi_i \frac{\partial}{\partial x_i} + \eta_j \frac{\partial}{\partial y_j}, \tag{3.9}$$

and if $\boldsymbol{y} = \boldsymbol{\Theta}(\boldsymbol{x})$ is a solution of differential equation. Therewith we receive

$$X[\boldsymbol{y} - \boldsymbol{\Theta}(x)] = 0 \quad \text{with} \quad \boldsymbol{y} = \boldsymbol{\Theta}(x). \tag{3.10}$$

Expanding the derivatives in (3.10) by using X according to (3.9), we obtain the hyperbolic system

$$\xi_k(\boldsymbol{x}, \boldsymbol{\Theta}) \frac{\partial \theta_l}{\partial x_k} = \eta_l(\boldsymbol{x}, \boldsymbol{\Theta}) \tag{3.11}$$

and the correspoinding characteristic equation

$$\frac{dx_1}{\xi_1(\boldsymbol{x}, \boldsymbol{\Theta})} = \frac{dx_2}{\xi_2(\boldsymbol{x}, \boldsymbol{\Theta})} = \cdots = \frac{dx_m}{\xi_m(\boldsymbol{x}, \boldsymbol{\Theta})} = \frac{dy_1}{\eta_1(\boldsymbol{x}, \boldsymbol{\Theta})} = \frac{dy_2}{\eta_2(\boldsymbol{x}, \boldsymbol{\Theta})} = \cdots = \frac{dy_n}{\eta_n(\boldsymbol{x}, \boldsymbol{\Theta})}. \tag{3.12}$$

After solving the characteristic equation one receives the new variables. For this reason it is suggestive to take the $m-1$ solutions of the m equations on the left hand side as new independent variables. Each term of the n terms of the right hand side can set equal to one of the m terms on the left hand side. Due to this procedure the set of independent variables in the original partial diffential equation (PDE) reduces at least by one.

By generating invariant solutions, symmetries are partly broken due to extern conditions. Thus, special boundary or initial conditions are given, which are not conform with certain transformations.

3.4 Application to the present Turbulent Rotating Channel Flow

The basis for the analysis of the present flow geometry is the mean momentum equation and the two-point velocity correlation equation in a rotating frame of reference. Assuming the mean velocity parallel to the walls as shown in figure 1.5 and all stresses only depending on x_2 we obtain

$$0 = -\frac{1}{\rho}\frac{\partial \bar{p}}{\partial x_1} - \frac{\partial \overline{u'_1 u'_2}}{\partial x_2} + \nu \frac{\partial^2 \bar{u}_1}{\partial x_2^2} \tag{3.13a}$$

$$0 = -\frac{1}{\rho}\frac{\partial \bar{p}}{\partial x_2} - \frac{\partial \overline{u'_2 u'_2}}{\partial x_2} - 2\,\Omega_1 \bar{u}_3 \tag{3.13b}$$

$$0 = -\frac{\partial u'_2 u'_3}{\partial x_2} + \nu \frac{\partial^2 \bar{u}_3}{\partial x_2^2} \tag{3.13c}$$

and

$$\begin{aligned}0 = &-R_{2j}\delta_{i1}\frac{d\bar{u}_1(x_2)}{dx_2} - R_{2j}\delta_{i3}\frac{d\bar{u}_3(x_2)}{dx_2} - R_{i2}\delta_{j1}\frac{d\bar{u}_1(x_2+r_2)}{d(x_2+r_2)} - R_{i2}\delta_{j3}\frac{d\bar{u}_3(x_2+r_2)}{d(x_2+r_2)}\\ &- \left[\bar{u}_1(x_2+r_2) - \bar{u}_1(x_2)\right]\frac{\partial R_{ij}}{\partial r_1} - \left[\bar{u}_3(x_2+r_2) - \bar{u}_3(x_2)\right]\frac{\partial R_{ij}}{\partial r_3}\\ &- \frac{1}{\rho}\left[\delta_{i2}\frac{\partial \overline{p' u'_j}}{\partial x_2} - \frac{\partial \overline{p' u'_j}}{\partial r_i} + \frac{\partial \overline{u'_i p'}}{\partial r_j}\right] + \nu\left[\frac{\partial^2 R_{ij}}{\partial x_2 \partial x_2} - 2\,\frac{\partial^2 R_{ij}}{\partial x_2 \partial r_2} + 2\,\frac{\partial^2 R_{ij}}{\partial r_k \partial r_k}\right]\\ &- \frac{\partial R_{(i2)j}}{\partial x_2} + \frac{\partial}{\partial r_k}\left[R_{(ik)j} - R_{i(jk)}\right] - 2\,\Omega_1\left[e_{1li}R_{lj} + e_{1lj}R_{il}\right]\end{aligned} \tag{3.14}$$

(see e.g. Rotta (1972)); $\bar{u}_i$, $\bar{p}$, $\overline{u'_i u'_j}$, ν, Ω_1, and e_{ijk} are respectively the mean velocity, the mean pressure, the Reynolds stress tensor, the dynamic viscosity, the rotation rate in x_1-direction, and the alternation tensor. The five two-point correlation tensor functions which appear in equation (3.14) are defined as

$$R_{ij}(\boldsymbol{x}, \boldsymbol{r}; t) = \overline{u_i(\boldsymbol{x}, t)\, u_j(\boldsymbol{x}^{(1)}, t)}\ , \tag{3.15a}$$

$$\overline{p'u'_j}(\boldsymbol{x},\boldsymbol{r};t) = \overline{p'(\boldsymbol{x},t)\,u'_j(\boldsymbol{x}^{(1)},t)} \ , \quad \overline{u'_jp'}(\boldsymbol{x},\boldsymbol{r};t) = \overline{u'_j(\boldsymbol{x},t)\,p'(\boldsymbol{x}^{(1)},t)} \ , \tag{3.15b}$$

and

$$\begin{aligned} R_{(ik)j}(\boldsymbol{x},\boldsymbol{r};t) &= \overline{u'_i(\boldsymbol{x},t)\,u'_k(\boldsymbol{x},t)\,u'_j(\boldsymbol{x}^{(1)},t)} \ , \\ R_{i(jk)}(\boldsymbol{x},\boldsymbol{r};t) &= \overline{u'_i(\boldsymbol{x},t)\,u'_j(\boldsymbol{x}^{(1)},t)\,u'_k(\boldsymbol{x}^{(1)},t)} \ , \end{aligned} \tag{3.15c}$$

where u_i and p correspond to the fluctuating quantities. The tensors (3.15a)-(3.15c) are functions of the physical and the correlation space coordinates $\boldsymbol{x}$ and $\boldsymbol{r} = \boldsymbol{x}^{(1)} - \boldsymbol{x}$ respectively. For the present case all statistical quantities only depend on the wall-normal coordinate x_2 and the correlation coordinate $\boldsymbol{r}$. The double two-point correlation tensor R_{ij}, later on simply referred to as two-point correlation, converges to the Reynolds stress tensor $\overline{u'_iu'_j}$ in the limit of zero separation $|\boldsymbol{r}|$:

$$\overline{u'_iu'_j}(\boldsymbol{x}) = \lim_{r\to 0} R_{ij}(\boldsymbol{x},\boldsymbol{r}) \ . \tag{3.16}$$

It should be noted that the two-point correlation equation only contains the triple correlations as unknown terms. For both two-point velocity-pressure correlations, $\overline{u'_ip'}$ and $\overline{p'u'_j}$ a Poisson equation may be derived (see e.g. Oberlack (1994) and Oberlack (1995)). In addition, all dependent variables in equation (3.14) must satisfy the continuity conditions

$$\frac{\partial R_{ij}}{\partial x_i} - \frac{\partial R_{ij}}{\partial r_i} = 0 \ , \quad \frac{\partial R_{ij}}{\partial r_j} = 0 \ , \quad \frac{\partial \overline{p'u'_j}}{\partial r_j} = 0 \quad \text{and} \quad \frac{\partial \overline{u'_ip'}}{\partial x_i} - \frac{\partial \overline{u'_ip'}}{\partial r_i} = 0 \ . \tag{3.17}$$

For the understanding of the self-similarity of the two-point correlation equation given further below, two identities may give some interesting insight in the structure of the two-point correlation function. They can easily be derived from a geometrical consideration by interchanging the two points $\boldsymbol{x}$ and $\boldsymbol{x}^{(1)} = \boldsymbol{x} + \boldsymbol{r}$:

$$R_{ij}(\boldsymbol{x},\boldsymbol{r}) = R_{ji}(\boldsymbol{x}+\boldsymbol{r},-\boldsymbol{r}) \ , \ \overline{u'_ip'}(\boldsymbol{x},\boldsymbol{r}) = \overline{p'u'_i}(\boldsymbol{x}+\boldsymbol{r},-\boldsymbol{r}) \ . \tag{3.18}$$

The former is particularly interesting for the trace elements of R_{ij} since it defines a functional equation in real- and correlation-space. There also exists a similar identity to (3.18) for the triple correlation, which will not be utilized here.

Some fundamental properties of the flow can already be read from the equations (3.13a)-(3.13c). For high Reynolds number flows, viscous transport terms are only significant in the near-wall region. In regions sufficiently far from solid walls, the viscous terms may be neglected to leading order, and the balance is dominated by the pressure and the turbulent stresses.

From equation (3.13a) the usual linear turbulent shear stress profile for $\overline{u_1'u_2'}$ may be derived because the pressure-gradient in the streamwise (x_1) direction is constant. Since no pressure-gradient in the spanwise (x_3) direction is present, it can be deduced from equation (3.13c) that the shear stress $\overline{u_2'u_3'}$ is uniform. Equation (3.13b) only determines the pressure-gradient in wall-normal direction. Though it is the only mean momentum equation containing the Coriolis force, it has no influence on the mean velocity. It will be seen later that the mean velocity is only determined by the turbulent stresses. This is similar to the usual non-rotating channel flow in which no information for the mean flow can be determined from the mean momentum equation.

At this point it will be anticipated that besides the shear stress $\overline{u_2'u_3'}$ the additional shear stress $u_1'u_3'$ is induced due the rotation. This can be taken from equation (3.14) in which a Coriolis term appears in the R_{13}-equation. From the structure of the '13' equation, it appears that the Coriolis term may not be solely balanced by the pressure-velocity correlation and by the triple correlation. One may naturally expect that the term $[\bar{u}_k(x_2+r_2)-\bar{u}_k(x_2)]\,\partial R_{13}/\partial r_k$ may also contribute to the balance in the equation. Hence $u_1'u_3'$ may be non-zero though this stress has no counterpart in the mean velocities in an eddy-viscosity sense.

3.4.1 Time-scale Analysis

In the present subsection the characteristic time scales of the viscous sublayer and the universal logarithmic region will be compared with the characteristic time scale of the rotation rate. The latter is defined as

$$t_\Omega \equiv \frac{1}{\Omega} \tag{3.19}$$

where Ω is the rotation rate about the x_1-direction, also denoted by Ω_1.

The characteristic time scale of the viscous sublayer and the universal logarithmic region are

$$t_\nu \equiv \frac{\nu}{u_\tau^2} \quad \text{and} \quad t_{\log} \equiv \frac{y}{u_\tau} \tag{3.20}$$

respectively where u_τ is the 'friction velocity' defined as $u_\tau = \sqrt{\nu \left.\frac{\partial \bar{u}_1}{\partial x_2}\right|_{\text{wall}}}$. For sufficiently high Reynolds number, t_ν is a fixed small quantity while $t_{\log}$ increases with the distance from the wall. Comparing the ratio of the latter flow time scales with the rotation time scale we respectively obtain

$$T_1 = \frac{t_\nu}{t_\Omega} = \frac{\nu\Omega}{u_\tau^2} = \frac{\mathrm{Ro}}{2\mathrm{Re}_\tau} \tag{3.21}$$

$$T_2 = \frac{t_{\log}}{t_\Omega} = \frac{y\Omega}{u_\tau} = \mathrm{Ro}\frac{y}{h} \ , \tag{3.22}$$

where $\mathrm{Re}_\tau = hu_\tau/2\nu$ and $\mathrm{Ro} = \Omega h/u_\tau$.

For zero rotation rate both quantities are exactly zero. However, assuming Ro of the order $\mathcal{O}(1)$ and supposing Re to be a large parameter, the time scale ratio T_1 is a small quantity. Hence it is concluded that rotation only perturbs the viscous sublayer, and a significant change may not be observed.

Considering the same order of magnitude assumptions for Ro as above, it can be concluded that T_2 may only be a small parameter for small y/h. This is the flow region close to the wall and next to the viscous sublayer. In contrast, if y/h is of order $\mathcal{O}(1)$, T_2 may become an order $\mathcal{O}(1)$ parameter. Consequently, we conclude that this is the flow region which is affected most by the system rotation. In this region system rotation is a leading order effect. In addition we conclude that the region which is affected most by the rotation extends further to the wall with increasing rotation rate. The mean velocity of a turbulent channel flow is only weakly affected by the system rotation in the near-wall region. However, system rotation has a substantial effect on regions sufficiently far from the wall such as the logarithmic region up to the centerline.

In fact this global effect has been observed both in experiments and in DNS for the classical rotating channel flow with x_3 as the rotation axis (see e.g. Johnston et al. (1972) and Kristoffersen & Andersson (1993)). In contrast to the present case the classical rotating channel case does not reveal a symmetric mean velocity profile about the centerline. Instead a skewed mean velocity profile in the center part of the channel is observed, which will be proven in the next subsection. This is not the case for the present flow, in which u_1 stays symmetric about the centerline.

3.4.2 Reflection Symmetry of Statistical Flow Quantities about the Centerline

Reflection symmetries can be obtained by finding transformations of the form $\tilde{\phi} = -\phi$ where ϕ may represent any dependent and independent variable. The following is observed in a variety of different channel type of flows such as the usual turbulent Poiseuille and the turbulent Couette flow. If the corresponding equations and boundary conditions admit a certain reflection symmetry about the centerline, this is also verified for all statistical quantities.

For the present problem the system (3.14) and (3.17) admits the reflection symmetry where the variables are respectively separated as independent variables, mean quantities, and statistical quantities

$$\tilde{x}_1 = x_1 \ , \ \tilde{x}_2 = -x_2 \ , \ \tilde{x}_3 = -x_3 \ , \ \tilde{r}_1 = r_1 \ , \ \tilde{r}_2 = -r_2 \ , \ \tilde{r}_3 = -r_3 \ , \tag{3.23a}$$

$$\tilde{\bar{u}}_1 = \bar{u}_1 \ , \quad \tilde{\bar{u}}_3 = -\bar{u}_3 \ , \quad \tilde{\bar{p}} = \bar{p} \ , \tag{3.23b}$$

$$\begin{pmatrix} \tilde{R}_{11} & \tilde{R}_{12} & \tilde{R}_{13} \\ \tilde{R}_{21} & \tilde{R}_{22} & \tilde{R}_{23} \\ \tilde{R}_{31} & \tilde{R}_{32} & \tilde{R}_{33} \end{pmatrix} = \begin{pmatrix} R_{11} & -R_{12} & -R_{13} \\ -R_{21} & R_{22} & R_{23} \\ -R_{31} & R_{32} & R_{33} \end{pmatrix} \ , \tag{3.23c}$$

$$\begin{pmatrix} \widetilde{\overline{pu_1}} \\ \widetilde{\overline{pu_2}} \\ \widetilde{\overline{pu_3}} \end{pmatrix} = \begin{pmatrix} \overline{pu_1} \\ -\overline{pu_2} \\ -\overline{pu_3} \end{pmatrix} \quad \text{and} \quad \begin{pmatrix} \widetilde{\overline{u_1p}} \\ \widetilde{\overline{u_2p}} \\ \widetilde{\overline{u_3p}} \end{pmatrix} = \begin{pmatrix} \overline{u_1p} \\ -\overline{u_2p} \\ -\overline{u_3p} \end{pmatrix} \ . \tag{3.23d}$$

The latter reflection symmetries can be generalized as such that any other statistical one-, two-, and multi-point quantity can be determined from the fluctuation quantities according to the transformation for the fluctuations

$$\tilde{u}_1 = u_1 \ , \quad \tilde{u}_2 = -u_2 \ , \quad \tilde{u}_3 = -u_3 \ , \quad \tilde{p} = p \ . \tag{3.24}$$

For example, the transformation of the two-point triple correlations $R_{(ik)j}$ and $R_{i(jk)}$ which are not stated above can be determined in a similar manner.

From (3.23b) it can be determined that $\bar{u}_1$ is symmetric about the centerline and $\bar{u}_3$ is antisymmetric about the centerline.

The transformation of the Reynolds stress tensor can also be obtained by employing equation (3.16) in the transformation (3.23c). The consequences for the stresses are such that all normal stresses and the off-diagonal component $u_2'u_3'$ are symmetric about the centerline. In contrast $u_1'u_2'$ and $u_1'u_3'$ are antisymmetric about the centerline. It should be noted that the results for $u_1'u_2'$ and $u_2'u_3'$ can also be obtained from the mean momentum equations (3.13a) and (3.13c). The reflection properties of other one-point quantities such as the pressure-strain correlation and the dissipation tensor can also be determined by equation (3.24).

3.4.3 Lie Group Analysis

Lie group analysis is applied to the present turbulent rotating channel flow to find symmetries and invariant solutions (see Weller & Oberlack (2005a) and Oberlack, Cabot, Petterson Reif & Weller (2006)). The mechanism is based on the TPC equations.

For simplicity it will be assumed in the following analysis that the Reynolds number tends to infinity so that the viscous terms in the two-point correlation equation

(3.14) may be neglected. The basis for this assumption is the fact that, to leading order only, viscosity has no effect as $R_e \to \infty$. Viscosity only affects the small scales of the order $\mathcal{O}(\eta)$ where η is the Kolmogorov length scale. Hence neglecting viscosity is only valid for $|\boldsymbol{r}| > \eta$. If $|\boldsymbol{r}| < \eta$, the last term of the third line in equation (3.14) corresponds to the dissipation and cannot be neglected. A rigorous asymptotic analysis of the two regions $|\boldsymbol{r}| > \eta$ and $|\boldsymbol{r}| < \eta$, i.e. the derivation of a small and a large scale equation, may be taken from Oberlack (2002) or Oberlack & Guenther (2003).

The general purpose of Lie group analysis, also called symmetry analysis, is twofold. First, the symmetry transformations are to be determined, which give profound knowledge of the flow physics. Second, the symmetries may be used to achieve self-similarity or reduction of the two-point correlation equation. The first step to accomplish this objective is to find symmetry transformations which do not change the form of the equation under investigation. In fact, this is analogous to the analysis presented in the previous subsection where reflection symmetries have been investigated which do not alter the equations. However, the main difference in the present subsection is that the transformations considered therein are finite groups. In order to obtain a reduction, *continuous* groups of transformations need to be considered. The method to find the desired continuous groups of transformations is called Lie group analysis. A good introduction to this method is given in Bluman & Kumei (1989) and Stephani (1989). In the present subsection only a heuristic approach will be presented while some more mathematical details on group methods are presented in Appendix B in Oberlack (2001).

Self-similarity or reduction is always associated with the decrease of the number of independent variables. It is important to note that the independent variables are not necessarily restricted to the usual variables such as space and time. Instead any parameter in the equation under investigation may be considered as independent variable as long as it does not implicitly depend on any other independent parameter in the problem.

Hence, in the first step a reduction will be achieved by rewriting the two-point correlation equation as such that $\Omega_1 \equiv \Omega$ is absorbed into all the remaining independent and dependent variables. The most general form of transformation allowing this reduction is

$$x_i = \tilde{x}_i\gamma(\Omega) \ , \quad r_i = \tilde{r}_i\gamma(\Omega) \ , \quad \bar{u}_i = \tilde{\bar{u}}_i\gamma(\Omega)\Omega \ , \tag{3.25a}$$

$$R_{ij} = \tilde{R}_{ij}\gamma(\Omega)^2\Omega^2 \ , \quad p'u'i = \frac{\partial\widetilde{\overline{p'u'_i}}}{\gamma}(\Omega)^3\Omega^3 \ , \quad u'p'i = \frac{\partial\widetilde{\overline{u'_ip'}}}{\gamma}(\Omega)^3\Omega^3 \ , \tag{3.25b}$$

$$R_{(ik)j} = \tilde{R}_{(ik)j}\gamma(\Omega)^3\Omega^3 \ , \quad R_{i(jk)} = \tilde{R}_{i(jk)}\gamma(\Omega)^3\Omega^3 \ , \tag{3.25c}$$

where the new variables are denoted by tilde, and $\gamma(\Omega)$ is an arbitrary function of Ω. After employing (3.25a)-(3.25c) and imposing the high Reynolds number limit, the two-point correlation equations read

$$\begin{aligned}0 = &-\tilde{R}_{2j}\delta_{i1}\frac{d\tilde{\bar{u}}_1(\tilde{x}_2)}{d\tilde{x}_2} - \tilde{R}_{2j}\delta_{i3}\frac{d\tilde{\bar{u}}_3(\tilde{x}_2)}{d\tilde{x}_2} - \tilde{R}_{i2}\delta_{j1}\frac{d\tilde{\bar{u}}_1(\tilde{x}_2+r_2)}{d(\tilde{x}_2+\tilde{r}_2)} - \tilde{R}_{i2}\delta_{j3}\frac{d\tilde{\bar{u}}_3(\tilde{x}_2+r_2)}{d(\tilde{x}_2+\tilde{r}_2)} \\ &- \left[\tilde{\bar{u}}_1(\tilde{x}_2+\tilde{r}_2) - \tilde{\bar{u}}_1(\tilde{x}_2)\right]\frac{\partial\tilde{R}_{ij}}{\partial\tilde{r}_1} - \left[\tilde{\bar{u}}_3(\tilde{x}_2+\tilde{r}_2) - \tilde{\bar{u}}_3(\tilde{x}_2)\right]\frac{\partial\tilde{R}_{ij}}{\partial\tilde{r}_3} \\ &- \frac{1}{\rho}\left[\delta_{i2}\frac{\partial\widetilde{\overline{p'u'_j}}}{\tilde{x}_2} - \frac{\partial\widetilde{\overline{p'u'_j}}}{\tilde{r}_i} + \frac{\partial\widetilde{\overline{u'_ip'}}}{\tilde{r}_j}\right] \\ &- \frac{\partial\tilde{R}_{(i2)j}}{\partial\tilde{x}_2} + \frac{\partial}{\partial\tilde{r}_k}\left[\tilde{R}_{(ik)j} - \tilde{R}_{i(jk)}\right] - 2\left[e_{1li}\tilde{R}_{lj} + e_{1lj}\tilde{R}_{il}\right] \ .\end{aligned} \tag{3.26}$$

Note that this is essentially the form of equation (3.14) with $\nu = 0$. Obviously the set of independent variables x_2, r_i, and Ω has been reduced by one. From group theory it follows (see Oberlack (2001)) that the latter equation admits a further similarity reduction only for certain mean velocities which obey the equations

$$\begin{aligned}&[a_1(\tilde{x}_2+\tilde{r}_2)+a_3+a_5]\frac{d\tilde{\bar{u}}_1(\tilde{x}_2+\tilde{r}_2)}{d(\tilde{x}_2+\tilde{r}_2)} - a_1\tilde{\bar{u}}_1(\tilde{x}_2+\tilde{r}_2) \\ &\qquad = [a_1\tilde{x}_2+a_5]\frac{d\tilde{\bar{u}}_1(\tilde{x}_2)}{d\tilde{x}_2} - a_1\tilde{\bar{u}}_1(\tilde{x}_2) \ ,\end{aligned} \tag{3.27a}$$

$$\begin{aligned}&[a_1(\tilde{x}_2+\tilde{r}_2)+a_3+a_5]\frac{d\tilde{\bar{u}}_3(\tilde{x}_2+\tilde{r}_2)}{d(\tilde{x}_2+\tilde{r}_2)} - a_1\tilde{\bar{u}}_3(\tilde{x}_2+\tilde{r}_2) \\ &\qquad = [a_1\tilde{x}_2+a_5]\frac{d\tilde{\bar{u}}_3(\tilde{x}_2)}{d\tilde{x}_2} - a_1\tilde{\bar{u}}_3(\tilde{x}_2) \ .\end{aligned} \tag{3.27b}$$

The corresponding similarity variables are obtained from the invariant surface condition (see Bluman & Kumei (1989))

$$\begin{aligned}&\frac{d\tilde{r}_1}{a_1\tilde{r}_1+a_2} = \frac{d\tilde{r}_2}{a_1\tilde{r}_2+a_3} = \frac{d\tilde{r}_3}{a_1\tilde{r}_3+a_4} = \frac{d\tilde{x}_2}{a_1\tilde{x}_2+a_5} \\ &\qquad = \frac{d\tilde{R}_{ij}}{2a_1\tilde{R}_{ij}} = \frac{d\widetilde{\overline{p'u'_i}}}{3a_1\widetilde{\overline{p'u'_i}}} = \frac{d\widetilde{\overline{u'_jp'}}}{3a_1\widetilde{\overline{u'_jp'}}} = \frac{d\tilde{R}_{(ik)j}}{3a_1\tilde{R}_{(ik)j}} = \frac{d\tilde{R}_{i(jk)}}{3a_1\tilde{R}_{i(jk)}}\end{aligned} \tag{3.28}$$

where the constants of integration are taken as the new variables. The equations for the mean velocities above (3.27a) and (3.27b) can only have a unique solution if

$$a_3 = 0. \tag{3.29}$$

Since each equation (3.27a) and (3.27b) on the left-hand side depends on $\tilde{x}_2 + \tilde{r}_2$ and on the right-hand side on $\tilde{x}_2$, they can only be equal if they are both equal to a constant. Hence, by comparing the first brackets on the left and right side respectively, equations (3.27a) and (3.27b) uniquely become

$$[a_1\tilde{x}_2 + a_5]\frac{d\tilde{\bar{u}}_1(\tilde{x}_2)}{d\tilde{x}_2} - a_1\tilde{\bar{u}}_1(\tilde{x}_2) = c_1 \ , \tag{3.30a}$$

$$[a_1\tilde{x}_2 + a_5]\frac{d\tilde{\bar{u}}_3(\tilde{x}_2)}{d\tilde{x}_2} - a_1\tilde{\bar{u}}_3(\tilde{x}_2) = c_3 \ . \tag{3.30b}$$

Each of the parameters a_1-a_5 have a distinct physical meaning. The parameter a_1 corresponds to the scaling group; i.e. equation (3.26) admits a transformation of the form

$$\tilde{x}_2^* = \mathrm{e}^{a_1}\tilde{x}_2 \ , \quad \tilde{r}_i^* = \mathrm{e}^{a_1}\tilde{r}_i \ , \quad \tilde{\bar{u}}_i^* = \mathrm{e}^{a_1}\tilde{\bar{u}}_i \ , \tag{3.31a}$$

$$\tilde{R}_{ij}^* = \mathrm{e}^{2a_1}\tilde{R}_{ij} \ , \quad \widetilde{\overline{p'u_i'}}^{\,*} = \mathrm{e}^{3a_1}\widetilde{\overline{p'u_i'}} \ , \quad \widetilde{\overline{u_i'p'}}^{\,*} = \mathrm{e}^{3a_1}\widetilde{\overline{u_i'p'}} \ , \tag{3.31b}$$

$$\tilde{R}_{(ik)j}^* = \mathrm{e}^{3a_1}\tilde{R}_{(ik)j} \ , \quad \tilde{R}_{i(jk)}^* = \mathrm{e}^{3a_1}\tilde{R}_{i(jk)} \ , \tag{3.31c}$$

which does not alter the functional form of the equation written in the new coordinates. The parameters a_2-a_5 correspond to the translation groups which conform to the fact that (3.26) is autonomous with respect to $\tilde{x}_2$ and $\tilde{r}_i$. As a result (3.26) is invariant under transformations such as

$$\tilde{x}_2^* = \tilde{x}_2 + a_5 \ . \tag{3.32}$$

However, for physical reasons the translation invariance of $\tilde{r}_i$ is not meaningful, and a_2-a_4 must be zero. In order to understand the problem with these ‘artificial’ invariances, one has to call to mind that the translation invariance with respect to $\tilde{r}_i$ gives rise to a new solution where the correlation function is shifted in correlation space. Since R_{ij} reaches its finite maximum at $|\tilde{\boldsymbol{r}}| = 0$ and tends to zero for $|\tilde{\boldsymbol{r}}| \rightarrow \pm\infty$, a shift in the correlation space cannot be a new solution.

Depending on the value of a_1, two fundamentally different cases are to be distinguished for which a similarity reduction may be obtained.

3.4.3.1 $a_1 \neq 0$

This case corresponds to the fact that scaling with respect to space is not inhibited and (3.30a) and (3.30b) integrate to

$$\tilde{\bar{u}}_1 = C_1 \left(\bar{x}_2 + \frac{a_5}{a_1} \right) - \frac{c_1}{a_1} \ , \tag{3.33a}$$

$$\tilde{\bar{u}}_3 = C_3 \left(\bar{x}_2 + \frac{a_5}{a_1} \right) - \frac{c_3}{a_1} \ , \tag{3.33b}$$

where C_1 and C_3 are integration constants. If the transformation (3.25a) to the original coordinates is inferred, the latter equations read

$$\bar{u}_1 = C_1 \, \Omega \, x_2 + \Omega \, \gamma(\Omega) \left(C_1 \frac{a_5}{a_1} - \frac{c_1}{a_1} \right) \ , \tag{3.34a}$$

$$\bar{u}_3 = C_3 \, \Omega \, x_2 + \Omega \, \gamma(\Omega) \left(C_3 \frac{a_5}{a_1} - \frac{c_3}{a_1} \right) \ . \tag{3.34b}$$

It appears that the additive constants may depend on the rotation rate in an unknown manner. In order to resolve this problem, it is helpful to investigate the two-point correlation function.

Though a solid theoretical basis on first principles is still lacking, that to leading order the two-point correlation function does not scale with the rotation rate Ω. This is an empirical observation from DNS data, that R_{ij} is only very weakly influenced. Hence it can be concluded from equation (3.25b) that, in order to have no Ω dependence of R_{ij}, the function γ behaves as $\gamma \sim 1/\Omega$. As a result, the two additive constants appearing in the scaling laws (3.34a) and (3.34b) do not depend on Ω either. Only the slope of the linear scaling laws depends on the rotation rate.

The similarity variables for the case $a_1 \neq 0$ corresponding to the mean velocities (3.33a) and (3.33b) are obtained from the characteristic equations (3.28). Employing $a_2 = a_3 = a_4 = 0$, the integration yields

$$\eta_1 = \frac{\tilde{r}_1}{\tilde{x}_2 + \frac{a_5}{a_1}} \ , \quad \eta_2 = \frac{\tilde{r}_2}{\tilde{x}_2 + \frac{a_5}{a_1}} \ , \quad \eta_3 = \frac{\tilde{r}_3}{\tilde{x}_2 + \frac{a_5}{a_1}} \ , \tag{3.35a}$$

$$\tilde{R}_{ij} = F_{ij} \left(\tilde{x}_2 + \frac{a_5}{a_1} \right)^2 , \ \widetilde{\overline{p'u'_i}} = G_i \left(\tilde{x}_2 + \frac{a_5}{a_1} \right)^3 , \ \widetilde{\overline{u'_j p'}} = H_j \left(\tilde{x}_2 + \frac{a_5}{a_1} \right)^3 , \tag{3.35b}$$

$$\tilde{R}_{(ik)j} = F_{(ik)j} \left(\tilde{x}_2 + \frac{a_5}{a_1} \right)^3 \ , \quad \tilde{R}_{i(jk)} = F_{i(jk)} \left(\tilde{x}_2 + \frac{a_5}{a_1} \right)^3 \ , \tag{3.35c}$$

where the integration constants η_i, F_{ij}, G_i, H_i, $F_{(ik)j}$, and $F_{i(jk)}$ are the new similarity variables. In order to verify the similarity reduction of equation (3.26), the quantities F_{ij}, G_i, H_i, $F_{(ik)j}$, and $F_{i(jk)}$ are introduced as new dependent variables only depending on η_i.

In order to obtain a new identity in similarity space, the latter scaling is substituted into equation (3.18) for R_{ij}. For this purpose the origin of $\tilde{x}_2$ may be chosen as

$$\tilde{x}_2' = \tilde{x}_2 + \frac{a_5}{a_1} \tag{3.36}$$

such that the similarity variable simplifies to

$$\eta_i = \frac{\tilde{r}_i}{\tilde{x}_2'}. \tag{3.37}$$

Introducing the transformations (3.35a)-(3.35c) into equation (3.18), we obtain the relation $F_{ij}(\tilde{x}_2', \tilde{x}_2'\boldsymbol{\eta})(\tilde{x}_2')^2 = F_{ji}(\tilde{x}_2'(1+\eta_2), -\tilde{x}_2'\boldsymbol{\eta})\,(\tilde{x}_2')^2$. Since it was previously assumed that all two-point correlation functions are solely functions of $\boldsymbol{\eta}$, only the ratio of the first and the second parameter can appear in F_{ij}. Thus, we finally obtain

$$F_{ij}(\boldsymbol{\eta}) = F_{ji}\left(\frac{-\boldsymbol{\eta}}{1+\eta_2}\right) \ . \tag{3.38}$$

The latter relation gives valuable insight into the structure of the solution and it connects different $\tilde{\boldsymbol{r}}$ domains to each other.

Interestingly enough, relation (3.38) gives raise to a new symmetry transformation

$$\tilde{\eta}_i = \frac{-\eta_i}{1+\eta_2} \tag{3.39}$$

which is neither a reflection symmetry in the classical sense nor a continuous transformation (Lie group) since it does not contain a continuous parameter. Its validity can be verified by substituting (3.39) into equation (3.26) after the similarity coordinate (3.37) and the linear profiles (3.33a) and (3.33b) have been employed.

An interesting feature of (3.38) is that it can be considered as an algebraic functional equation for the trace element of F_{ij} or R_{ij} in the following, denoted as $F_{[ii]}$ with $i = 1, 2, 3$. The 'equilibrium' plane for (3.38) is $\eta_2 = -2$ with arbitrary η_1 and η_3 where both the argument as well as the value of F_{ij} are the same. In addition $\boldsymbol{\eta} = 0$ is an 'equilibrium' point. Apart from these two regions, equation (3.38) defines a mapping between different $\boldsymbol{\eta}$-domains. There are two pairs of η_2-regions which map into each other, namely

$$\eta_2 : \ \ (-\infty, -2) \leftrightarrow (-2, -1) \quad \text{and} \quad (-1, 0) \leftrightarrow (0, \infty) \ . \tag{3.40}$$

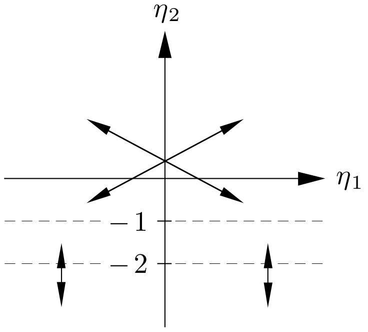

Figure 3.1: Non-locally related correlations in the η_1-η_2 plane according to (3.38).

The latter nomenclature refers to the fact that, once the functional values for $F_{[ii]}$ in the η_2 region $(-2,-1)$ are known, the corresponding values in the region $(-\infty,-2)$ are uniquely determined and vice versa. After a value for η_2 is chosen, the values for η_1 and η_3 map according to

$$\frac{-\eta_1}{1+\eta_2} \to \eta_1 \quad \text{and} \quad \frac{-\eta_3}{1+\eta_2} \to \eta_3 \tag{3.41}$$

A graphical mapping scheme is given in figure 3.1. For clarity only the η_1-η_2 domain is depicted where connected mapping regions are indicated by arrows. The extension to the entire $\boldsymbol{\eta}$-domain is straightforward.

Besides the above symmetry relation for $F_{[ii]}$ with $i = 1,2,3$, equation (3.38) provides solutions for any off-diagonal F_{ij} element with $(i \neq j)$ if F_{ji} is known. Of course, similar features can be given for the pressure-velocity correlation and for the triple correlation.

For the present case $a_1 \neq 0$, the statistical variables scale with the wall distance. This is different in the following subsection.

3.4.3.2 $a_1 = 0$

This case corresponds to the fact that scaling with respect to space is broken as can also be read from the equation (3.31a)-(3.31c). As a result the equation (3.30a) and (3.30b) may be integrated to

$$\tilde{\tilde{u}}_1 = \frac{c_1}{a_5}\tilde{x}_2 + C_3 \ , \quad \tilde{\tilde{u}}_3 = \frac{c_3}{a_5}\tilde{x}_2 + C_4 \ , \tag{3.42}$$

where C_3 and C_4 are integration constants. The characteristic equation (3.28) can not be integrated in the usual way. However, a reduction may still be possible since the correlation equation is autonomous with respect to x_2. Due to the linear profile all statistical functions in equation (3.26) may not depend on the spatial coordinate $\tilde{x}_2$. Obviously, the present case corresponds to a homogeneous shear flow. Even though this does not appear to be a reduction in the usual sense from a group theoretical point of view, this is similar to the case $a_1 \neq 0$. In §3.4.3.1 a reduction was attained by the scaling group (a_1) while in the present case the reduction may be attained by the translation group (a_5). In both cases the dimensionality of the problem is reduced.

It should be noted that for physical reasons the case $a_1 \neq 0$ appears to be more likely to be applicable to the rotating channel flow for the following reason. One of the key observations in Oberlack (2001) was that turbulence has a tendency to establish a maximum degree of symmetry transformations. For the different channel flow cases, the highest degree of symmetry has been observed where the least wall influence is present, namely in the core region of the channel. Hence it may be expected that the same maximum principle applies for the present flow.

To conclude from the analysis, it is to be expected that a cone-shaped mean velocity in the streamwise direction will appear such that the two flanks of the cone are linear. Furthermore, linear profiles for the cross flow will also be established on both sides of the centerline.

4 Direct Numerical Simulation

4.1 Introduction

A direct numerical simulation (DNS) means a complete three-dimensional and time-dependent numerical solution of the Navier-Stokes and continuity equations without any turbulence model (Pope 2000). The whole range of spatial and temporal scales of the turbulence is resolved. All spatial scales of the turbulence must be resolved in the computational mesh, from the smallest, the Kolmogorov scales η, up to the integral scale L, associated with the motions containing most of the kinetic energy.
The Kolmogorov scale η is given by

$$\eta = \left(\frac{\nu^3}{\epsilon} \right)^{1/4} , \tag{4.1}$$

where ν is the kinematic viscosity and ϵ is the rate of kinetic energy dissipation. The integral scale depends on the spatial scale of the flow configuration, through its extended geometry.
To satisfy these resolution requirements, the number N of grid points along a given direction with increments h, must be $Nh > L$, so that the integral scale is contained within the computational domain, and also $h \leq \eta$, so that the Kolmogorov scale can be resolved.

The integration of the solution in time must be done by an explicit method, in order to be accurate. The integration must be done with a time step small enough to be sure that a fluid particle moves only a fraction of the mesh in each step.

The memory storage requirement in a DNS grows very fast with the Reynolds number. This is the reason why a DNS is inapplicable for industrial applications. However, DNS is a useful tool in fundamental research in turbulence (Pope 2000).

DNS allows to extract all possible and important informations, which cannot be obtained in the laboratory experiments. Herewith a better understanding of the physics of turbulence can be achieved. DNS are also useful in the development of turbulence models, such as sub-grid scale models for Large Eddy Simulation (LES) and Reynolds-averaged Navier-Stokes equations (RANS) modeling. The input data for the models can be taken from a DNS and the results produced by a model can be compared with those obtained by DNS.

The largest known high-resolution DNS in the world, so far, using 4096^3 grid points, was carried out on the Japanese Earth Simulator (ES) supercomputer in 2002. The DNS yields an energy spectrum exhibiting a wide inertial subrange, in contrast to previous DNSs with lower resolutions, and therefore provides valuable data for the study of the universal features of turbulence at large Reynolds number. The calculation provides us with detailed data on turbulence that is free of experimantal uncertainty. DNS is therefore not only a powerful means for findings directly applicable solutions to problems in practical application areas that involve turbulent phenomena, but also for advancing our understanding of turbulence itself (see (Yokokawa, Itakura, Uno, Ishihara & Kaneda 2002)).

The first attempt of a DNS was made by Orszag & Patterson Jr. (1972) in 1972 for homogeneous turbulence. Considerably later the DNS for a fully developed turbulent channel flow was performed by Kim, Moin & Moser (1987). In this paper the first DNS of a non-rotating turbulent channel flow was presented at a Reynolds number of $Re_\tau = 180$. Later, more elaborate DNS of a turbulent channel flow were conducted e.g. by Kuroda, Kasagi & Hirata (1989), Kasagi, Tomita & Kuroda (1992) and Moser, Kim & Mansour (1999) primarily to increase the Reynolds number ($Re_\tau = 640$). Recently the DNS of turbulent channel flow for higher Reynolds numbers was done by Abe, Kawamura & Matsuo (2001). Computations at higher Reynolds numbers were also under investigation in the group of Jiménez in Madrid, Spain. Studies were carried out to Reynolds numbers up to $Re_\tau = 2003$ (see Hoyas & Jiménez (2006)).

The first extensive DNS study of a turbulent channel flow with spanwise rotation has been carried out by Kristoffersen & Andersson (1993) at a rather low Reynolds number. The Reynolds number based on the bulk mean velocity U_m and the channel half-width h was about 2900, while the rotation number $Ro = 2\Omega h/U_m$ varied between 0 and 0.5. It was found, that at the low rotation rate $Ro = 0.01$ the turbulent statistics varied only weakly compared to the non-rotating case. Increase of the rotation rate leads to an augmentation and damping of turbulence along the pressure and suction sides respectively. The mean velocity profile and Reynolds stresses became highly asymmetric. Rotation-induced Taylor-Görtler-like counter-rotating streamwise vortices have been identified and it was suggested that vortices are shifted slightly towards the pressure side with increasing rotation rate as it was experimentally observed by Johnston et al. (1972).
Another effect of the rotation were found in DNS data: gradually decrease of

turbulent Reynolds stresses with increasing rotation rate near the suction side, while turbulence intensities in the normal and spanwise direction monotonically increase on the pressure side. Streamwise intensity and the Reynolds shear stress component were also increased on the pressure side at the moderate rotation rate, while at the highest rotation rate considered in the DNS, they were considerably suppressed. With an increasing rotation rate, the mean velocity profile became increasingly asymmetric. In addition, a striking laminarization was visualized along the suctions side at the highest rotation number (Kristoffersen & Andersson 1993).

The most recent DNS of turbulent channel flow with arbitrary rotation was performed by Wu & Kasagi (2004). In this simulations three cases were considered by combining two of the orthogonal rotating vectors. It was found that spanwise rotation effects are still dominant in the flow. The Reynolds number based on bulk mean velocity was $Re = 4560$.

Rotation about the streamwise direction has been intensively studied only recently. In 1998, first investigations by Oberlack et al. (1998) using symmetry theory showed that there is a new turbulent scaling law related to the turbulent channel flow rotating about the mean flow direction. The flow has several common features with the classical rotating channel flow (Johnston et al. 1972) but also has some different characteristics. The induction of a mean velocity in x_3-direction (Oberlack 2001) is the most obvious difference compared to the classical case. This cross flow can be deduced by investigating the mean momentum equation and the Reynolds stress transport equation. Statistical evaluations have shown that all six components of the Reynolds stress tensor are non-zero.

4.2 Numerical Method

The DNS is based on a standard spectral method with Fourier decomposition in the streamwise and spanwise directions as well as Chebyshev decomposition in the wall-normal direction. The original version of the code for non-rotating coordinate systems was developed at KTH in Stockholm (Lundbladh, Henningson & Johansson 1992). Additional features such as the streamwise rotation and statistics were added.

All flow quantities are non-dimensionalized by $h/2$ and u_{CL}, where h is the channel half-height and u_{CL} is the centerline (CL) velocity of the flow field. The boundary conditions are no-slip at $x_2 = \pm 1$ and periodic in x_1- and x_3-direction. For all computations the pressure-gradient is kept constant $\frac{\partial p}{\partial x_1} = const.$. The calcula-

tions start from a laminar velocity channel flow profil.
The time integration is performed using a third order Runge-Kutta scheme. The transformation between physical and spectral space is done by Fast Fourier Transform (FFT). Further details on the numerical scheme may be obtained from Lundbladh et al. (1992).

After the simulations all flow quantities were normalized on the friction velocity u_τ

$$u_\tau = \sqrt{\nu \frac{\partial \bar{u}_1}{\partial x_2} \mid_{Wall}}\ . \tag{4.2}$$

The Reynolds number is defined as follows:

$$Re_\tau = \frac{h u_\tau}{2\nu} \tag{4.3}$$

and the rotation number as

$$Ro = \frac{\Omega h}{u_\tau}. \tag{4.4}$$

The code is parallelized by OpenMP. The OpenMP application programming interface (API) supports multi-platform shared memory multiprocessing programming. All calculations were conducted either at the Hessian High Performance Computer (HHLR) at Technische Universität Darmstadt or at the Jump cluster at John von Neumann Institute for Computing (NIC) in Jülich. Both supercomputers are Shared Memory Computers (SMC), which are particularly well suitable for parallel computations with many of interprocess communication.

Figure 4.1 shows a performance study of the parallelization of the code conducted at NIC in Jülich. The required simulation time in seconds for five time units is plotted respectively for the non-parallelized case and 2, 4, 8, 16 and 32 CPUs. For the study a data set of a rather small mesh of 4.2 Mio grid points was selected.

The curve shows that the code is good parallelized to save simulation time. The biggest gradient of the curve is observed between 1 and 2 CPUs. The simulation time is cut into halves from 3679[sec] to 1852[sec]. Also a lot of the simulation time can be saved from 2 to 4 CPUs and 4 to 8 CPUs. The gradients in these regions of the curve are nearly constant.
For more CPUs the curve decreases only weakly. Therefore the calculation in this example (at 4.2 Mio grid points) was run at 8 CPUs.
With an increasing number of grid points the required number of CPUs are also growing. For example: the simulations at a mesh of about 63 Mio grid points were run at 32 CPUs.

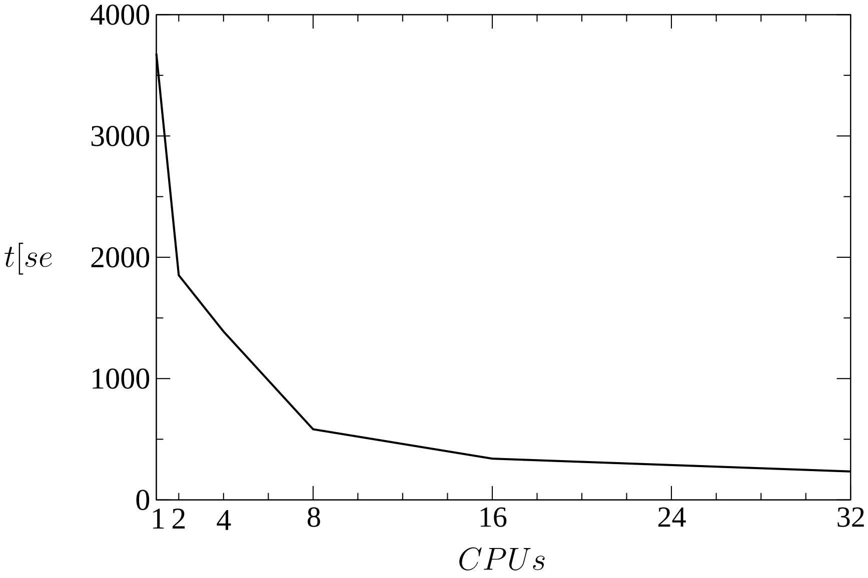

Figure 4.1: Performance study at NIC. The simulation time for five time units is plotted as a function of the number of CPUs.

4.3 Computations at $Re_\tau = 180$

4.3.1 Computations

An overview on the different flow case, the computational domain and the corresponding grid points is given in table 4.1.

A general problem with the DNS of a rotating channel flow is that it requires rather a long integration time to get smooth statistics such as $\overline{u_i'u_j'}$ (Weller, Recktenwald, Oberlack & Schröder 2005). All computations presented in table 4.1 were run for $10000\frac{h/2}{u_a cl}$ time units and the statistics accumulation was performed for the last 5000 time units.

4.3.2 Verification of the Computational Domain

In the DNS of turbulent pipe flow rotating about its axis it was observed by Orlandi & Fatica (1997) that very long coherent structures in the streamwise direction appear. Hence, a large computational domain in the streamwise direction is required

Table 4.1: Computations at $Re_\tau = 180$.

Sim.	Ro	Box($L_1 \times L_2 \times L_3$)	Grid($N_1 \times N_2 \times N_3$)	Grid points
1	0	$4\pi \times 2 \times 2\pi$	$128 \times 129 \times 128$	2.1 Milo
2	1	$4\pi \times 2 \times 2\pi$	$128 \times 129 \times 128$	2.1 Milo
3	3.2	$4\pi \times 2 \times 2\pi$	$128 \times 129 \times 128$	2.1 Milo
4	4	$4\pi \times 2 \times 2\pi$	$128 \times 129 \times 128$	2.1 Milo
5	5.2	$4\pi \times 2 \times 2\pi$	$128 \times 129 \times 128$	2.1 Milo
6	7	$8\pi \times 2 \times 4\pi$	$256 \times 129 \times 128$	4.2 Milo
7	10	$8\pi \times 2 \times 4\pi$	$256 \times 129 \times 128$	4.2 Milo
8	14	$8\pi \times 2 \times 4\pi$	$256 \times 129 \times 128$	4.2 Milo
9	20	$8\pi \times 2 \times 4\pi$	$256 \times 129 \times 128$	4.2 Milo
10	60	$24\pi \times 2 \times 4\pi$	$640 \times 385 \times 256$	63.1 Milo
11	100	$32\pi \times 2 \times 4\pi$	$640 \times 385 \times 256$	63.1 Milo

to achieve a sufficient decay to zero for the two-point correlation functions.

Since the coherent structures in the rotating channel flow are expected to increase at higher rotation rates the domain is increased by a factor of 2 from $Ro = 7$ up to $Ro = 20$. At $Ro = 60$ the domain is increased by a factor of 6 and by a factor of 8 for the largest rotation rate.

The two-point correlation functions are displayed for all rotation rates in figures 4.2 - 4.3. In general, it is ascertained that all curves decay to zero. Therewith it is shown that the computational domains were large enough for all computions.

As the comparison of the two-point correlation functions for different rotation rates shows, the correlation areas increase significantly in the streamwise direction with the rotation. Thus, the length scales within the flow are growing accordingly. At $Ro = 0$ the zero-crossing is at about $x_1/h = 3$ and increases up to $x_1/h = 30$ for the highest rotation rate. As a result it implies larger coherent turbulent structures in the rotating channel flow.

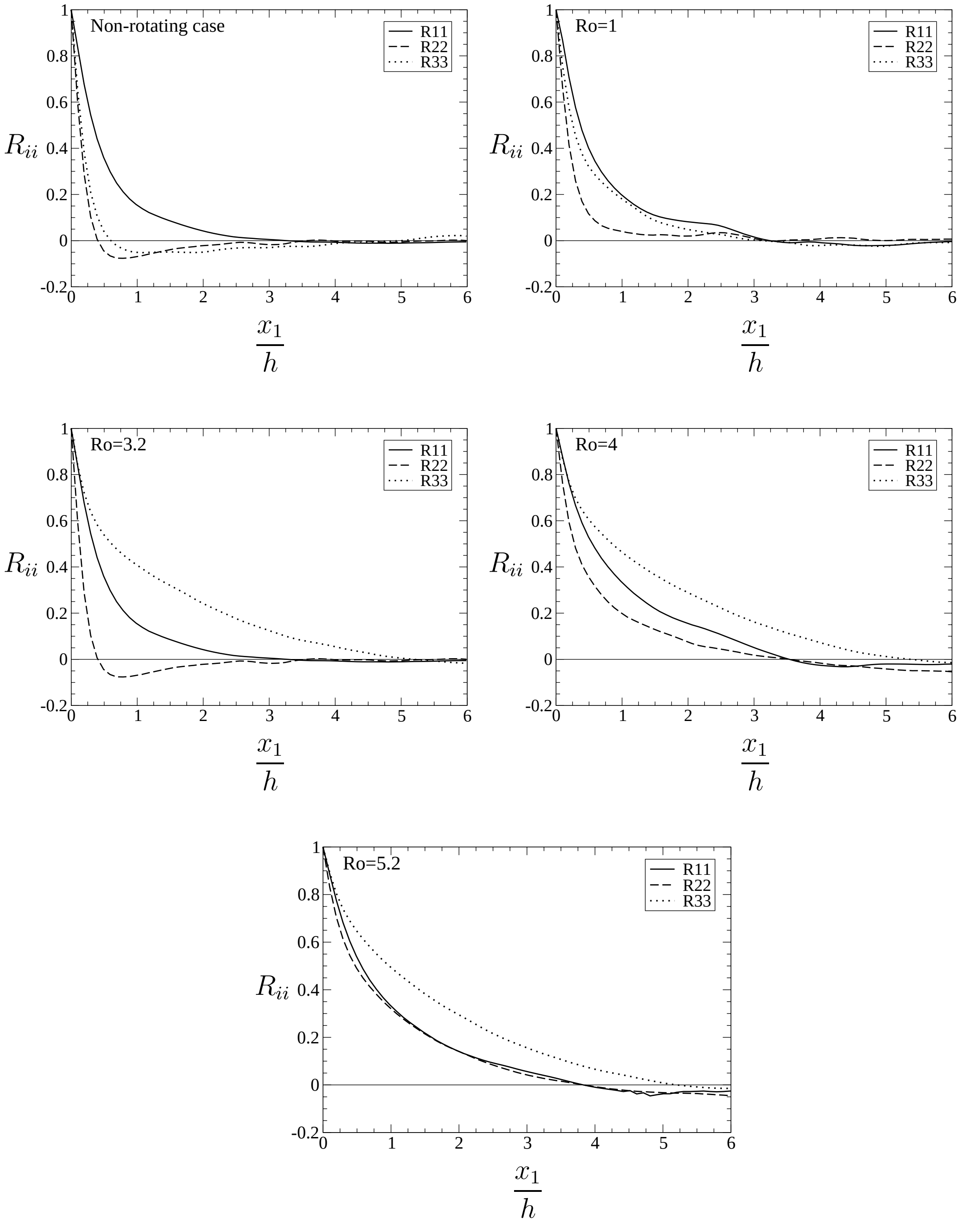

Figure 4.2: TPC R_{ii} in the streamwise direction at CL for the non-rotating case and at $Ro = 1, 3.2, 4,$ and 5.2.

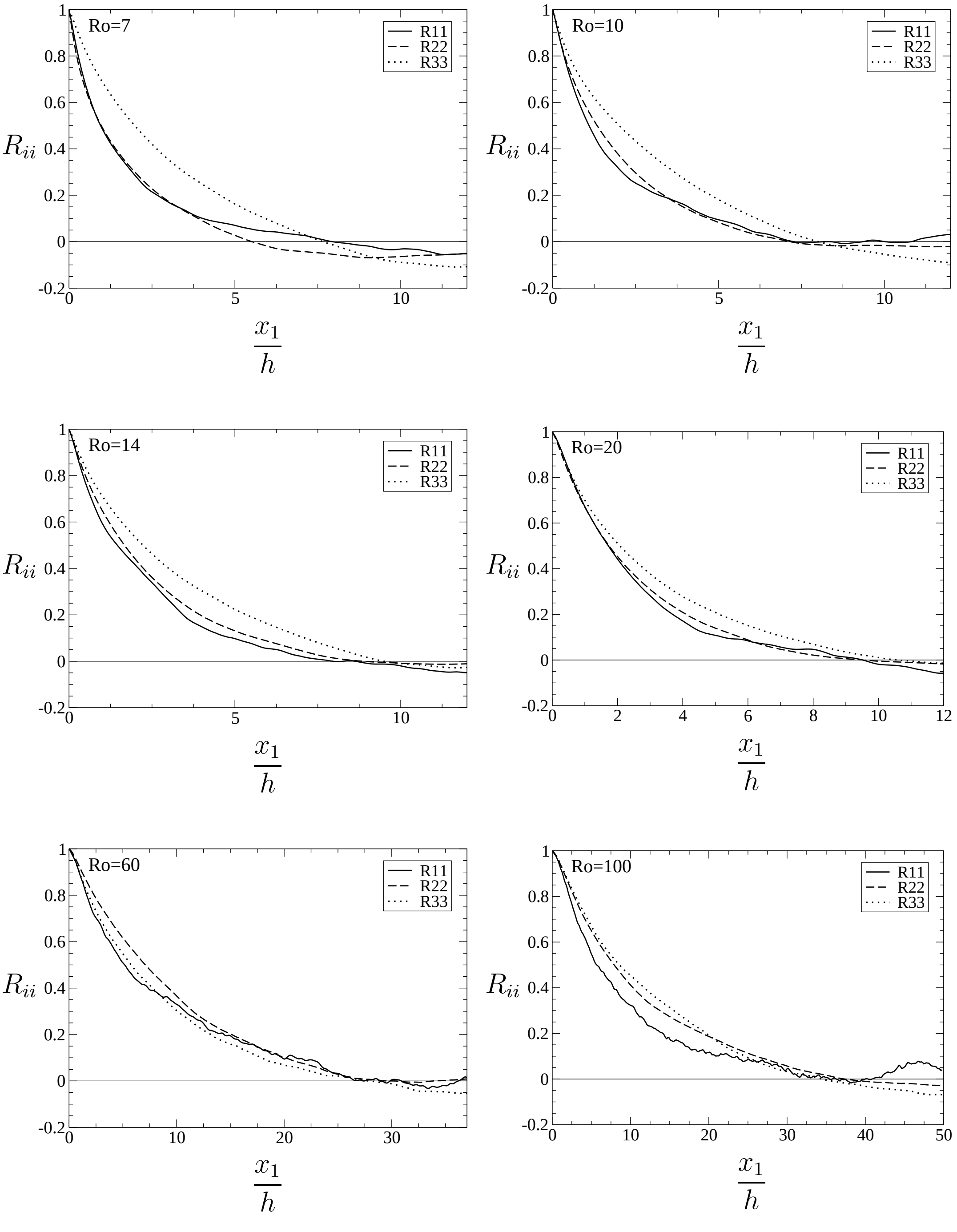

Figure 4.3: TPC R_{ii} in the streamwise direction at the CL at $Ro = 7, 10, 14, 20, 60$ and 100.

4.3.3 Verification of the Grid Resolution

The grid resolutions in the streamwise and spanwise direction were $\Delta x_1^+ \approx 17.67$ (sim. 1-9), $\Delta x_3^+ \approx 8.84$ (sim. 1-5) and $\Delta x_3^+ \approx 17.67$ (sim. 6-9).
As for the resolution in the wall-normal direction it is $\Delta x_2^+ \approx 0.054$ near the wall and becomes more and more coarse away from the wall because of the Chebyshev discretization in this direction. Thus, the resolution in the wall-normal direction is $\Delta x_2^+ \approx 0.05 - 4.42$ (sim. 1-9).
At higher rotation rates the resolutions in the streamwise and spanwise direction had to be increased to $\Delta x_1^+ \approx 21.21$ (sim. 10), $\Delta x_1^+ \approx 28.27$ (sim. 11) and $\Delta x_3^+ \approx 8.84$ (sim. 1-9). The wall-normal resolution varies from $\Delta x_2^+ \approx 0.02$ to 2.62 (sim. 10-11). These values are summarized in table 4.2.

Table 4.2: Grid resolution at $Re_\tau = 180$.

Sim.	Ro	Δx_1^+	$\Delta x_2^+(WR) - \Delta x_2^+(CL)$	Δx_3^+
1-5	0, 1, 3.2, 4, 5.2	17.67	0.054 - 4.417	8.84
6-9	7, 10, 14, 20	17.67	0.054 - 4.417	17.67
10	60	21.21	0.019 - 2.618	8.84
11	100	28.27	0.019 - 2.618	8.84

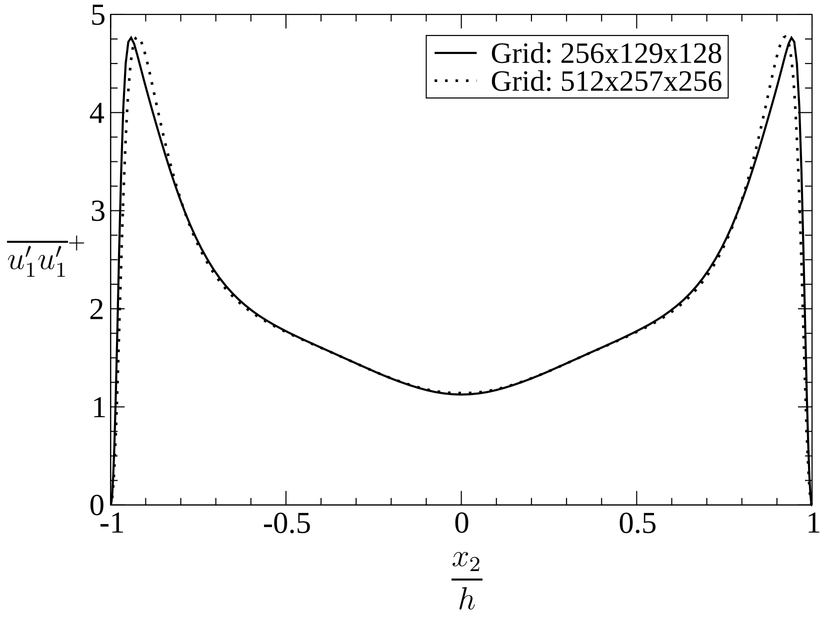

Figure 4.4: Grid resolution study at $Ro = 5.2$ (Sim. 5).

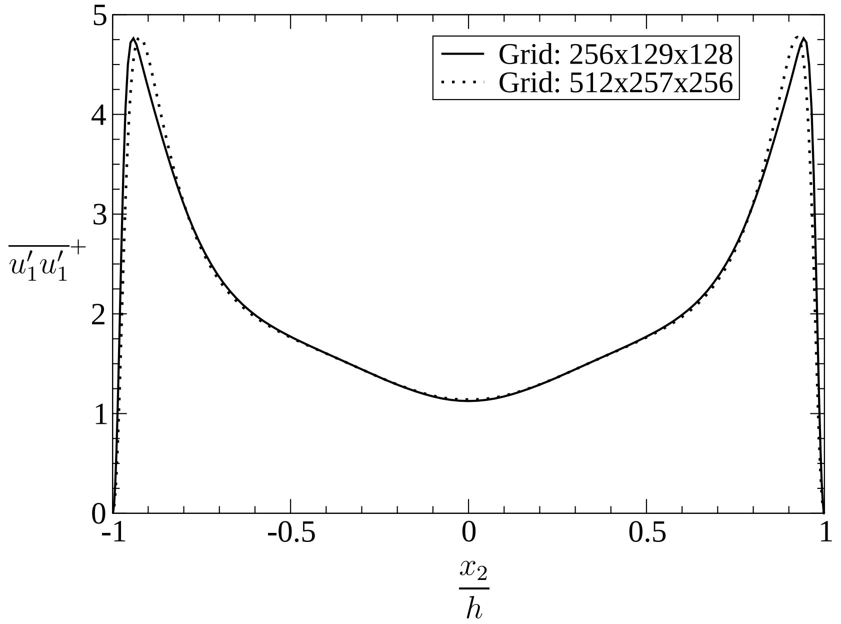

Figure 4.5: Grid resolution study at $Ro = 10$ (Sim. 9).

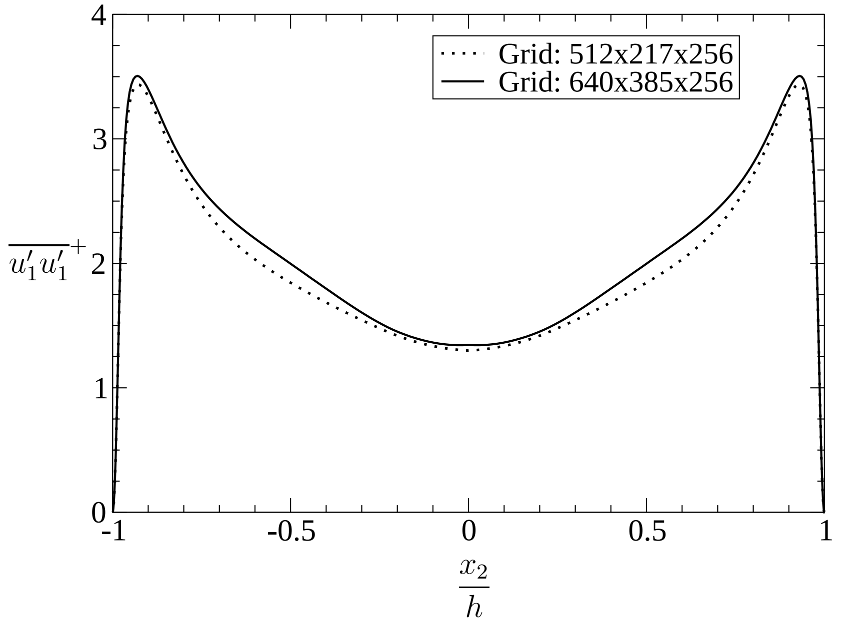

Figure 4.6: Grid resolution study at $Ro = 60$ (Sim. 10).

To verify the computed resolutions from table 4.2, in the following figures a selected

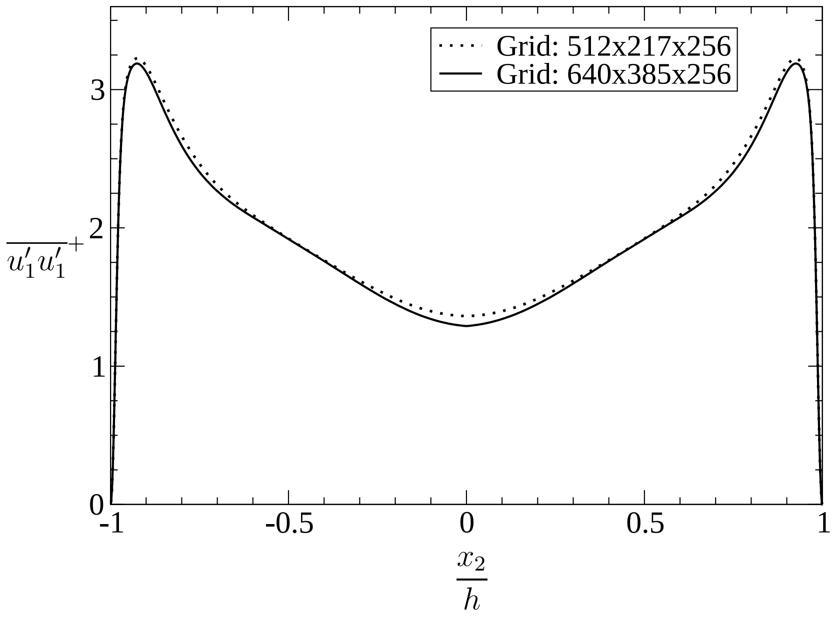

Figure 4.7: Grid resolution study at $Ro = 100$ (Sim. 11).

quantity is plotted at different grid resolutions. For the comparison a quantity at least squared is suitable, because errors are also squared in the results and differences are clearly visible. Here, the normal stress $\overline{u_1'u_1'}^+$ is used.

In the figures 4.4-4.7 the normal stress component $\overline{u_1'u_1'}^+$ is shown at different resolutions. First in the resolution of table 4.1 (solid line), which will be utilized further in this thesis and at one different resolution. In each figure the curves are close to each other, no significant differences are visible. Only a small difference is observed near the wall (see figures 4.4, 4.5, 4.7). We conducted that the utilized grid resolutions of the simulations in table 4.2 are sufficient.

4.3.4 Results

4.3.4.1 Comparison to Kim, Moin, Moser (1987) DNS

As it was shown in table 4.1, one simulation for the non-rotating case was performed. In the following, the results are compared to the results of Kim et al. (1987) at $Re_\tau = 180$. In their DNS also a spectral method was used. The domain sizes used in x_1-, x_2-, and x_3-directions were 4π, 2, and 2π on a $192 \times 129 \times 160$ grid.

In figure 4.8 the streamwise mean velocity profile $\bar{u}_1$ from our DNS is compared to the result of Kim et al. (1987). In figures 4.9 and 4.10 the Reynolds stresses $\overline{u_1'u_1'}$, $\overline{u_2'u_2'}$, $\overline{u_3'u_3'}$ and $\overline{u_1'u_2'}$ are compared.
All presented results for $Ro = 0$ are in good agreement with the data from Kim et al. (1987).

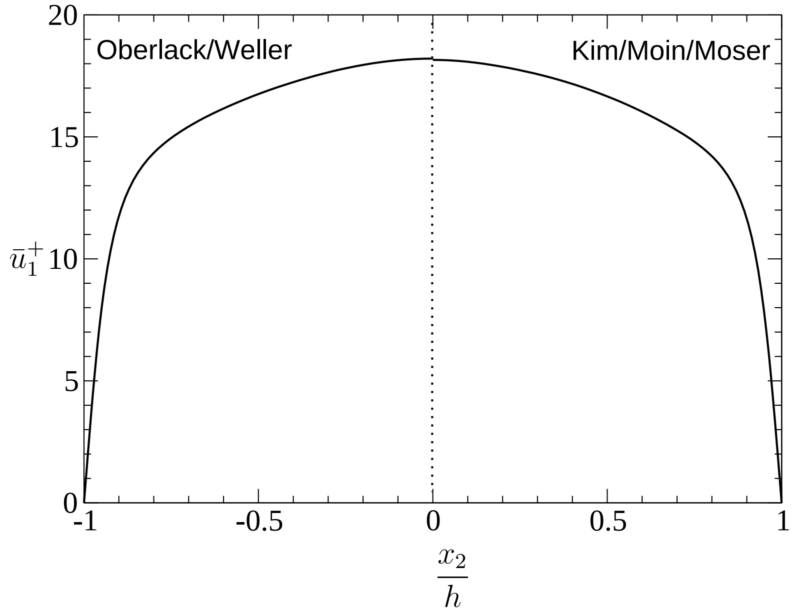

Figure 4.8: Comparison of our DNS results to Kim, Moin, Moser (1987): mean velocity profile $\bar{u}_1$.

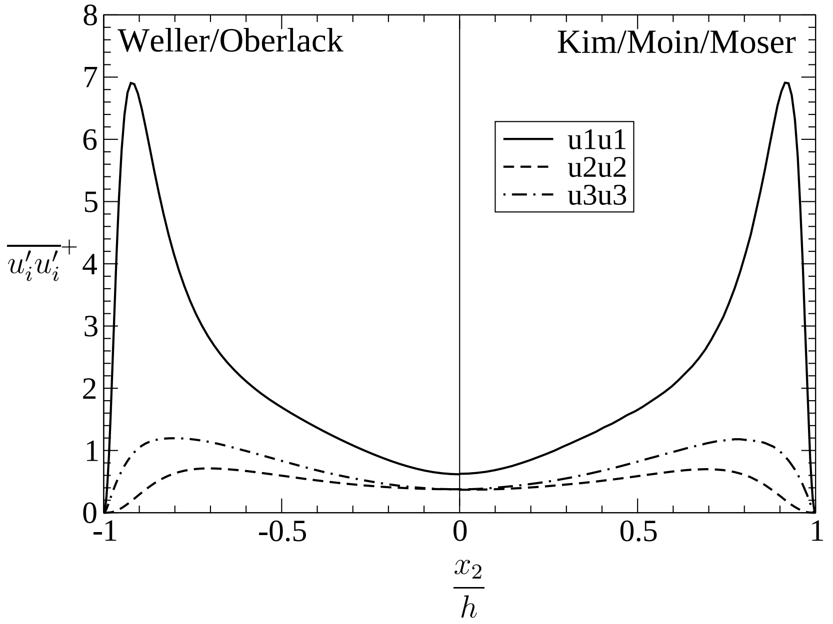

Figure 4.9: Comparison of our DNS results to Kim, Moin, Moser (1987): Reynolds normal stresses $\overline{u_i'u_i'}$.

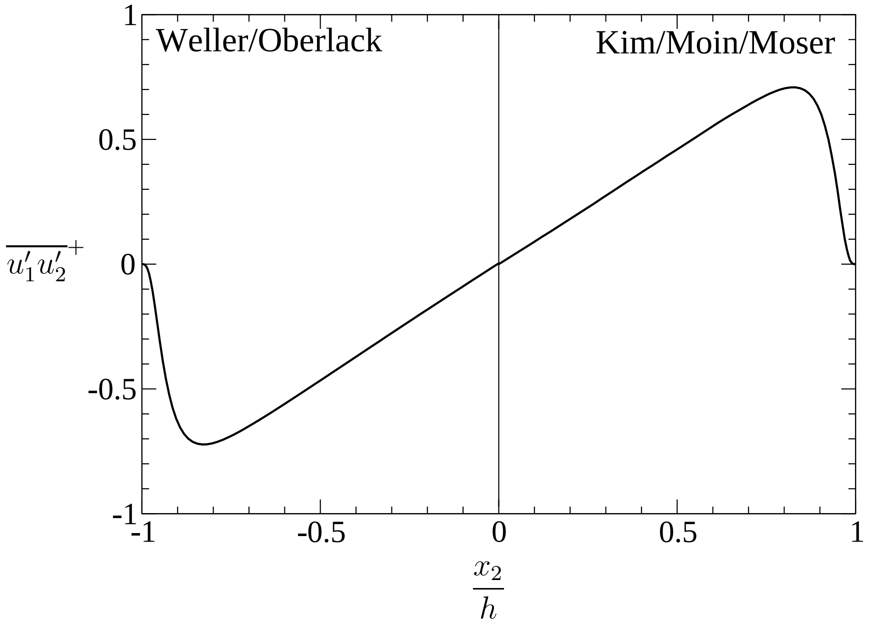

Figure 4.10: Comparison of our DNS results to Kim, Moin, Moser (1987): Reynolds normal stresses $\overline{u_1'u_2'}$.

4.3.4.2 Mean Velocity Profiles

Figure 4.11 shows the streamwise mean velocity profiles at different rotation rates. In general, the profiles decrease monotonically with increasing rotation number.

In particular, a significant decay of the maximum velocity i.e. $\bar{u}_1^+ = 16.94$ down to $\bar{u}_1^+ = 13.98$ between $Ro = 5.2$ and 10 is observed, which at the same time means a significant decrease in mass flux or increase in drag. A more detailed view of this effect can be taken from fig. 4.12, where the development of the mass flux is plotted over the rotation rate. The significant decay is also visible between $Ro = 5.2$ and 10.

For the highest rotation rates $Ro = 60$ and $Ro = 100$ the decrease is only marginally, it seems that a minium is approached as Ro tends to infinity.

As shown by the group analysis, two linear regions appear to emerge on each side of the centerline for smaller rotation rates. A more detailed perspective of the linear region is given in figure 4.13 where only the 'head' of the profile for Ro = 5.2 and Ro = 20 is depicted. For Ro = 5.2 linear regions roughly cover the wide range $x_2 = 0.3 - 0.8$ on both sides of the center line, whereas at Ro = 20 the linear regions disappear and the profile becomes more and more round. It seems that the derived Lie Group theory is limited to smaller rotation rates. For higher rotation rates further research is required.

As predicted from the Lie Group theory by Oberlack et al. (2006) the cross flow can be observed in all DNS. Figure 4.14 displays the spanwise mean velocity profiles at different rotation rates. The location of the linear region is slightly shifted towards the wall region compared to the linear region of the streamwise velocity.

The profiles show an S-shaped skew-symmetric cross flow with a flow reversal in the core region of the channel with three zero-crossings. The larger velocities near the wall can be explained by the Coriolis forces (Alkishriwi, M. & Schröder 2006). The flow reversal, if it occurs at all, is due to another mechanism, which is probably driven by larger turbulent structures, which are encountered at higher rotation rates.

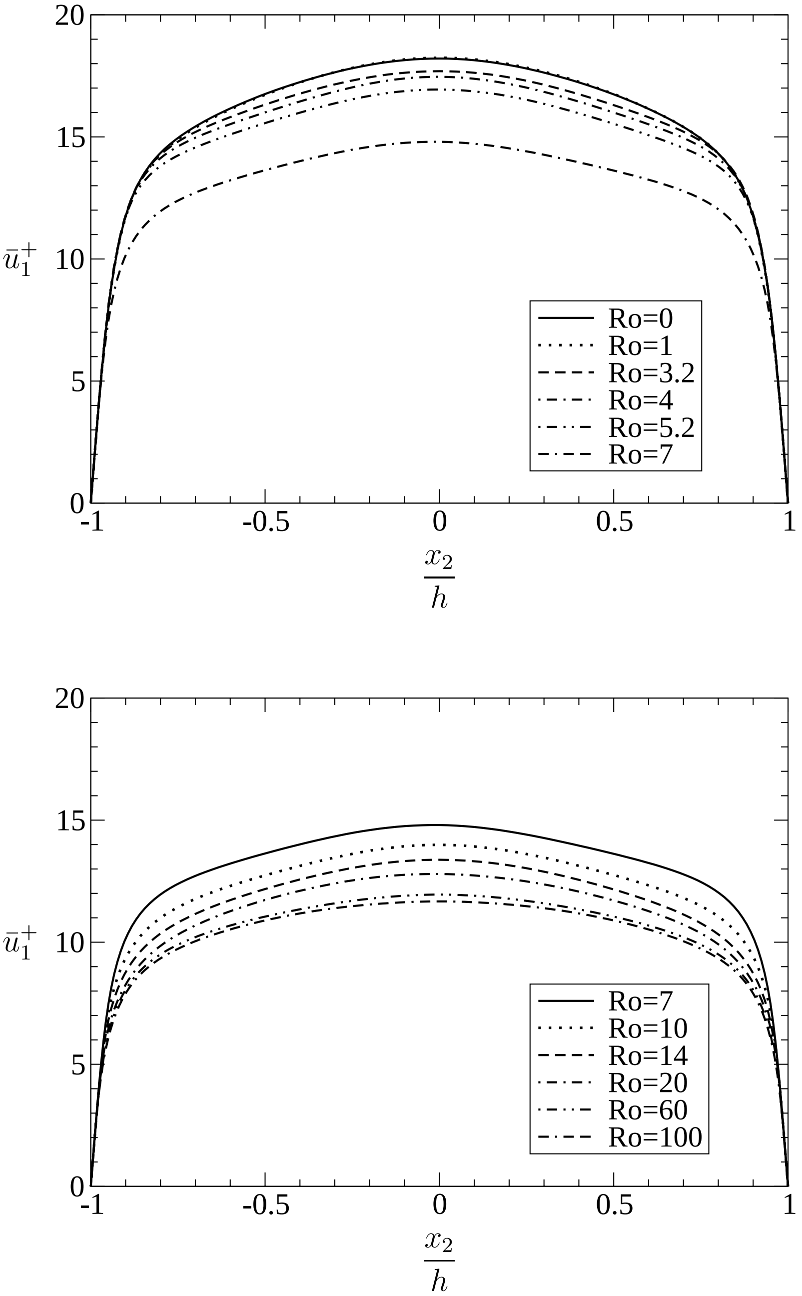

Figure 4.11: Streamwise mean velocity profiles ($\bar{u}_1$) at different rotation rates.

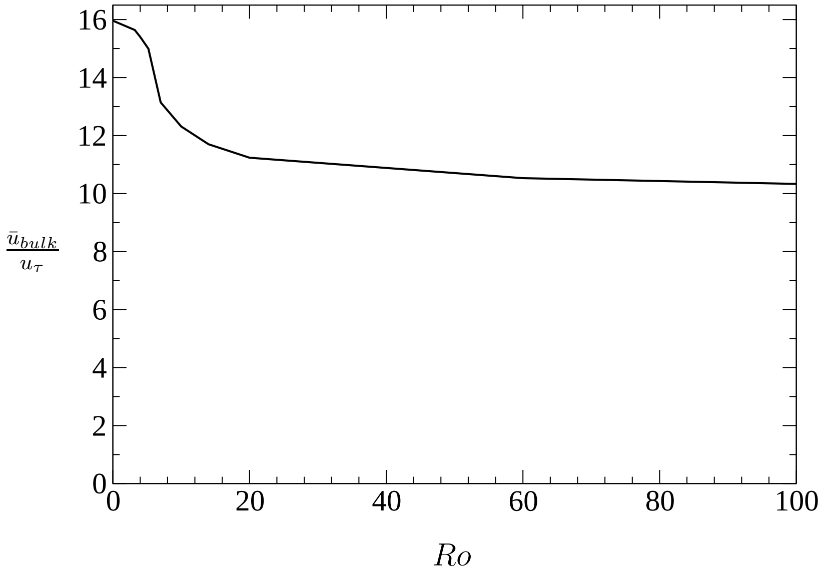

Figure 4.12: Development of $\bar{u}_{bulk}$ for increasing rotation rates.

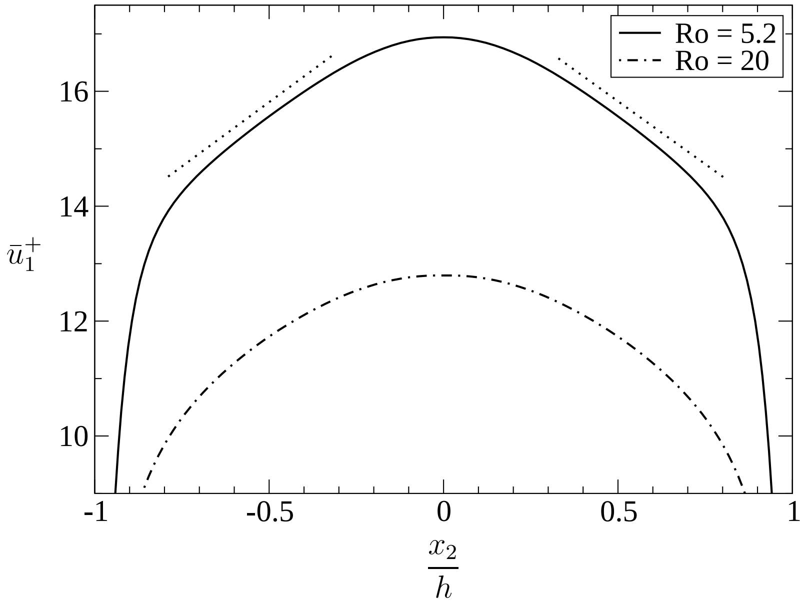

Figure 4.13: Linear region of the streamwise mean velocity profiles $\bar{u}_1$ at $Ro = 5.2$ and its disappearance for higher rotation rates (here $Ro = 20$).

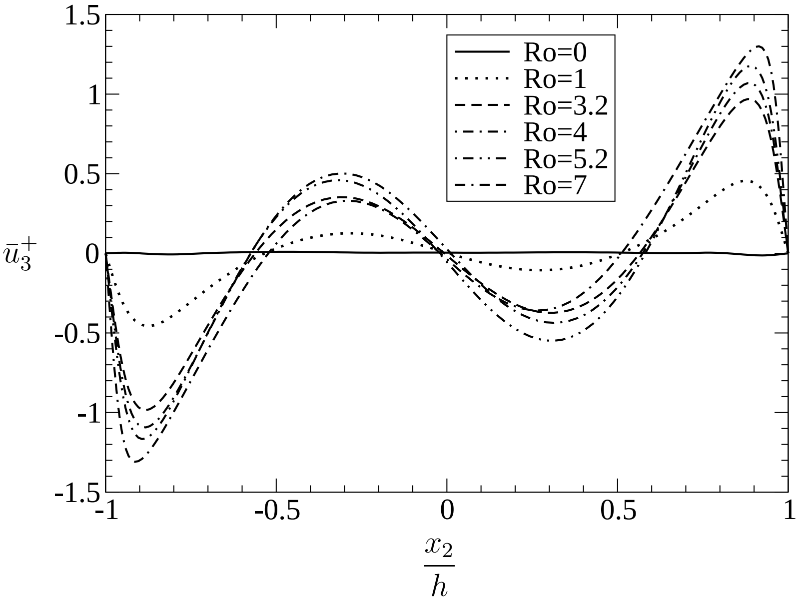

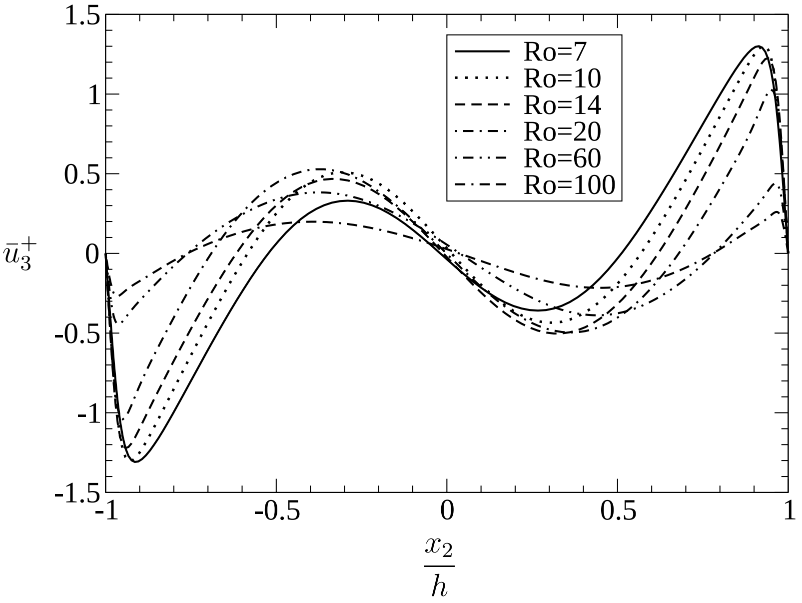

Figure 4.14: Spanwise mean velocity profiles ($\bar{u}_3$) at different rotation rates.

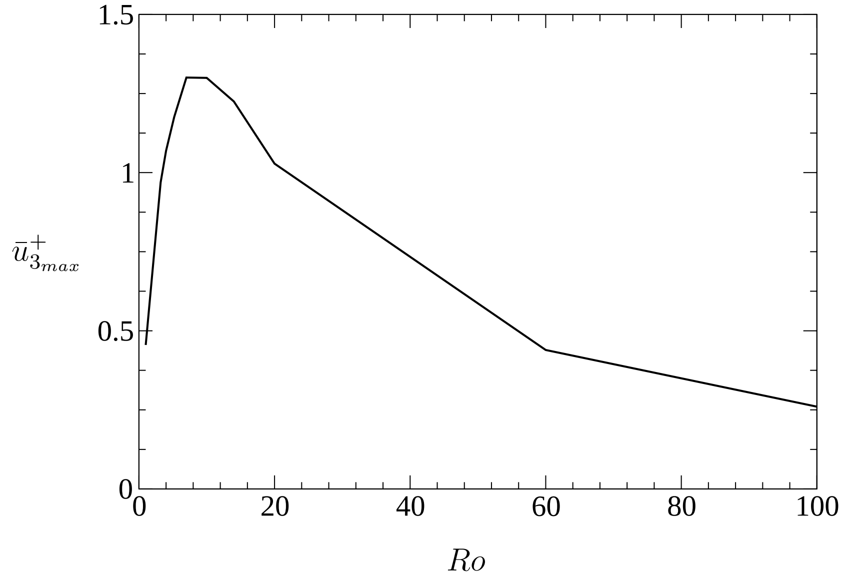

Figure 4.15: Development of $\bar{u}_{3_{max}}$ as a function of the rotation rate.

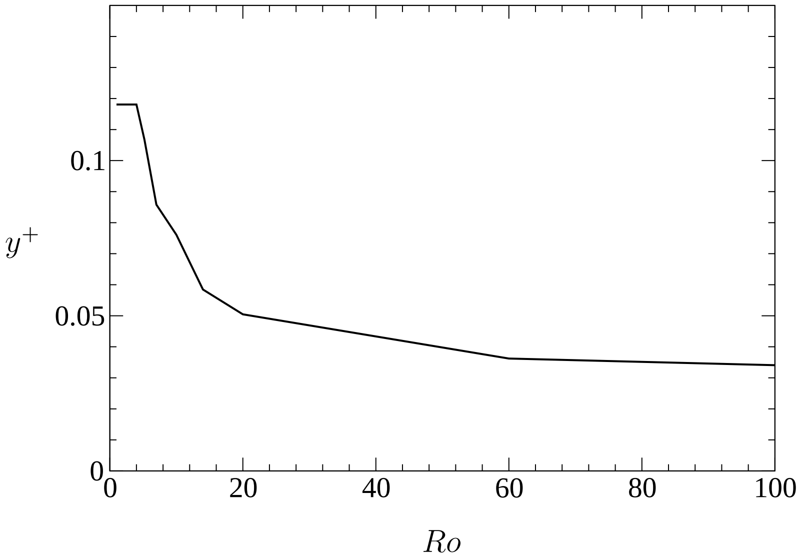

Figure 4.16: Distance from the wall y^+ of $\bar{u}_{3_{max}}$ as a function of the rotation rate.

Further, it is important to notice, that with increasing Ro the maximum value of the cross flow reaches a maximum at about $Ro = 10$ and then decreases for higher Ro. In figure 4.15 the development of $\bar{u}_{3_{max}}$ as a function of the rotation rate is shown.

Additionally, with an increasing rotation rate, the maxima get closer to the wall and at the same time the $\bar{u}_3$ boundary layer decreases. A more detailed perspective is given in figure 4.16, where the distance from the wall $y+$ of $\bar{u}_{3_{max}}$ is plotted as function of the rotation rate. The curve decreases rapidly up to $Ro = 20$ and goes on with a smaller gradient for higher rotation rates. That means that the boundary layer thickness approaches a minimum for $Ro \to \infty$.

Since both profiles exhibit a significant change at about the same rotation number $Ro = 10$, a significant change in the flow dynamics at this value is conjectured. The above observations will be given the name *rotation drag effect* (RDE), due to increased drag leading to a reduced mass flux in x_1-direction.

4.3.4.3 Reynolds Stress Tensor

From the statistical one-point quantities, the Reynolds stress tensor is displayed. In figures 4.17 - 4.22 the six components are shown. As predicted from the Lie group analysis by Oberlack et al. (Oberlack et al. 2006) the DNS shows in contrast to the non-rotating case, that all six components of the Reynolds stress tensor are non-zero.

In general, all statistical curves are symmetric or skew-symmetric about the centerline. The stress $\overline{u_1'u_1'}$ decreases at higher rotation, whereas $\overline{u_2'u_2'}$ and $\overline{u_3'u_3'}$ increase. The shear stress $\overline{u_1'u_2'}$ is nearly similar for all rotation rates.

The rotation about the streamwise axis leaves the momentum equation in the streamwise direction unaffected by the Coriolis force since $\bar{u}_1$ and the rotation axis are parallel. So for two-dimensional flow such as channel flow it reads

$$\frac{\partial \bar{u}_1}{\partial t} + \bar{u}_1 \frac{\partial \bar{u}_1}{\partial x_1} + \bar{u}_2 \frac{\partial \bar{u}_1}{\partial x_2} = -\frac{1}{\rho}\frac{\partial \bar{p}}{\partial x_1} + \frac{\partial}{\partial x_2}\left[\nu \frac{\partial \bar{u}_1}{\partial x_2} - \overline{u_1'u_2'}\right]. \tag{4.5}$$

In stationary, turbulent channel flow the derivative $\partial\bar{u}_1/\partial x_1$ and the averaged wall-normal velocity component $\bar{u}_2$ must vanish. Additionally, the viscous terms, which are significant only near the wall, can be neglected (Oberlack et al. 2006).

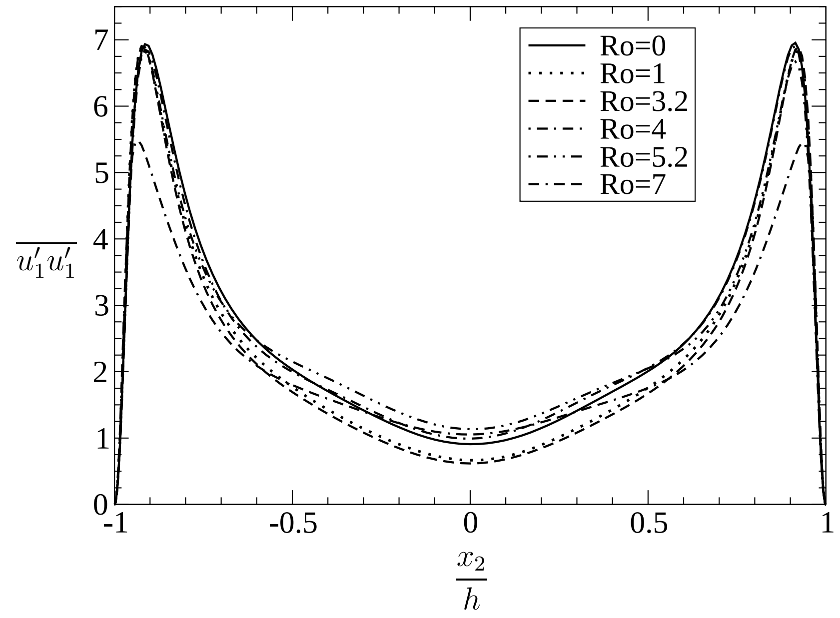

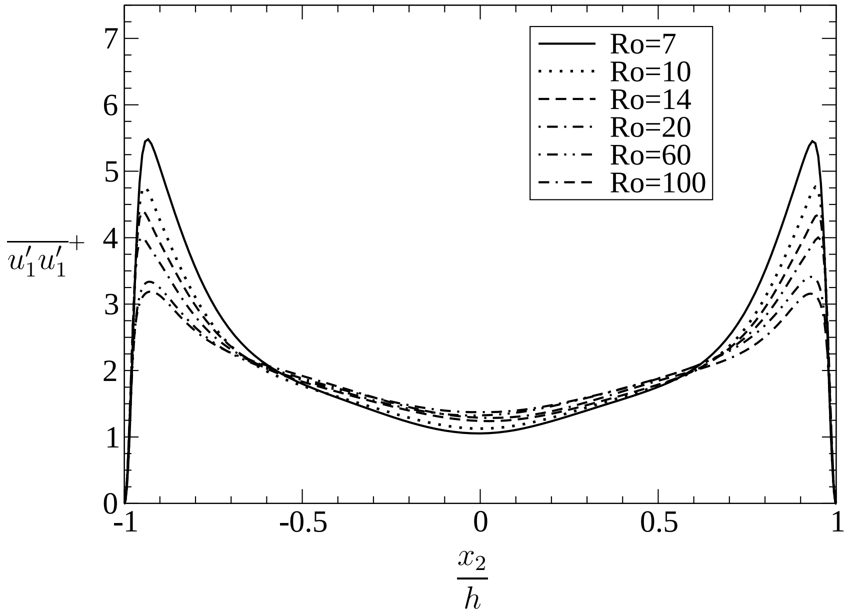

Figure 4.17: Reynolds normal stresses $\overline{u'_1u'_1}$ at different rotation rates.

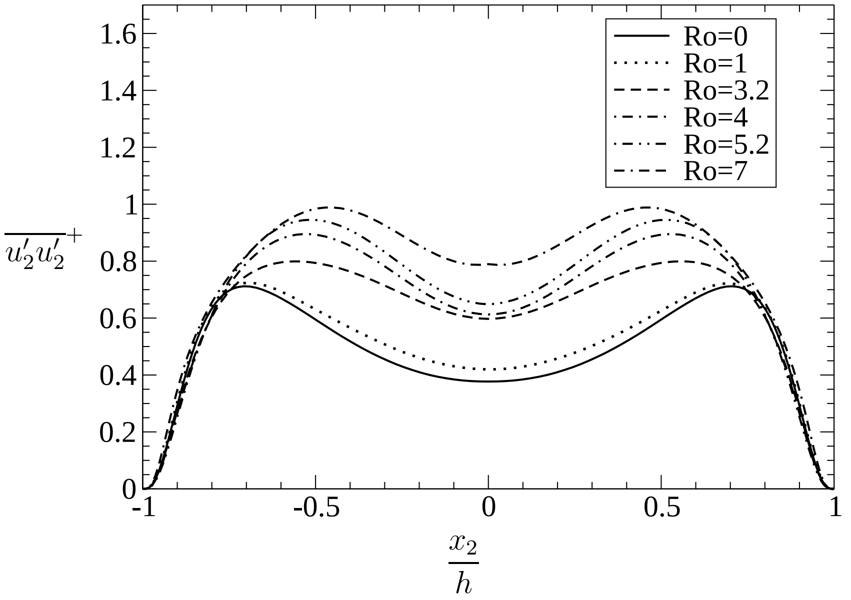

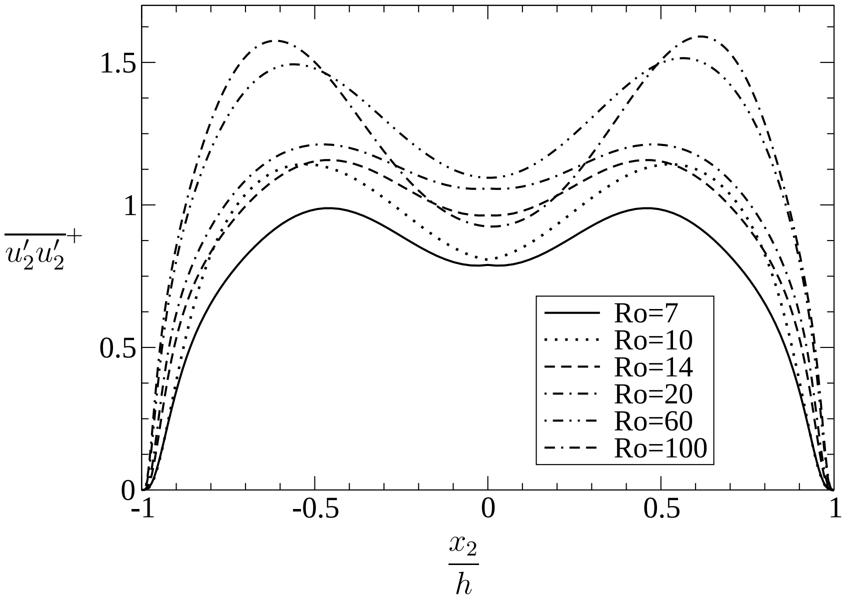

Figure 4.18: Reynolds normal stresses $\overline{u_2'u_2'}$ at different rotation rates.

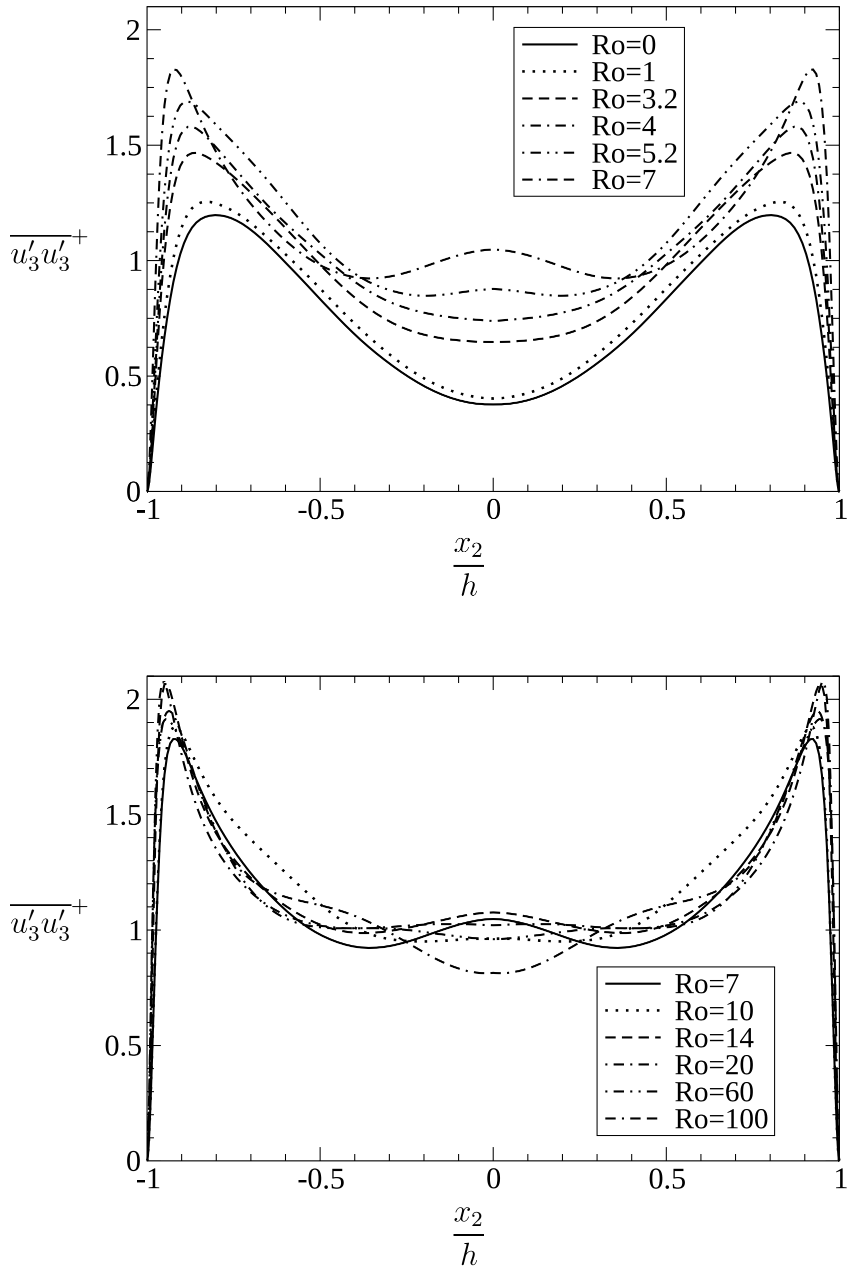

Figure 4.19: Reynolds normal stresses $\overline{u_3'u_3'}$ at different rotation rates.

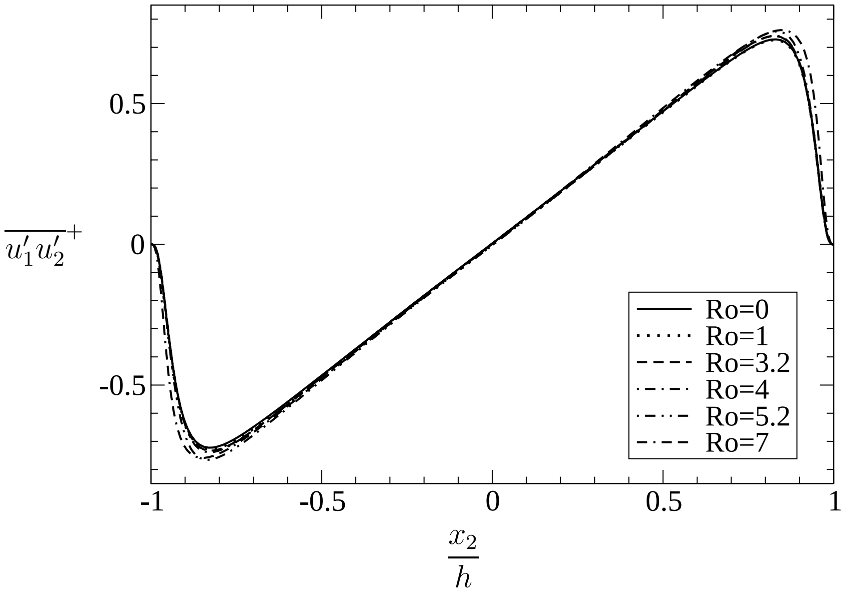

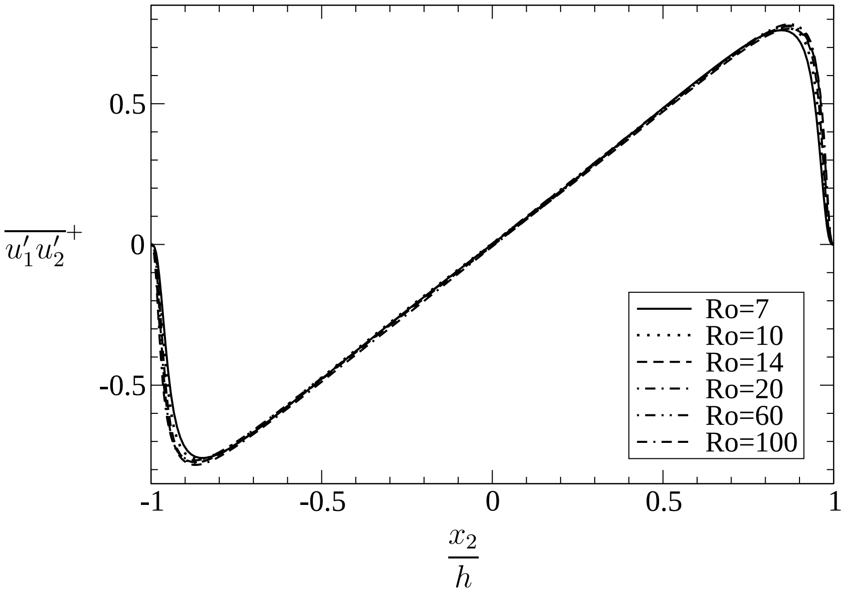

Figure 4.20: Reynolds shear stresses $\overline{u_1'u_2'}$ at different rotation rates.

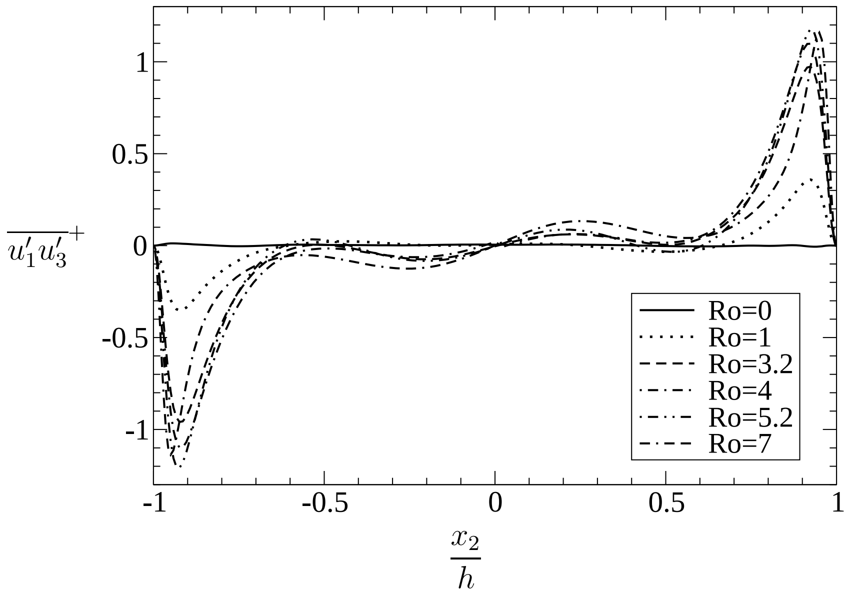

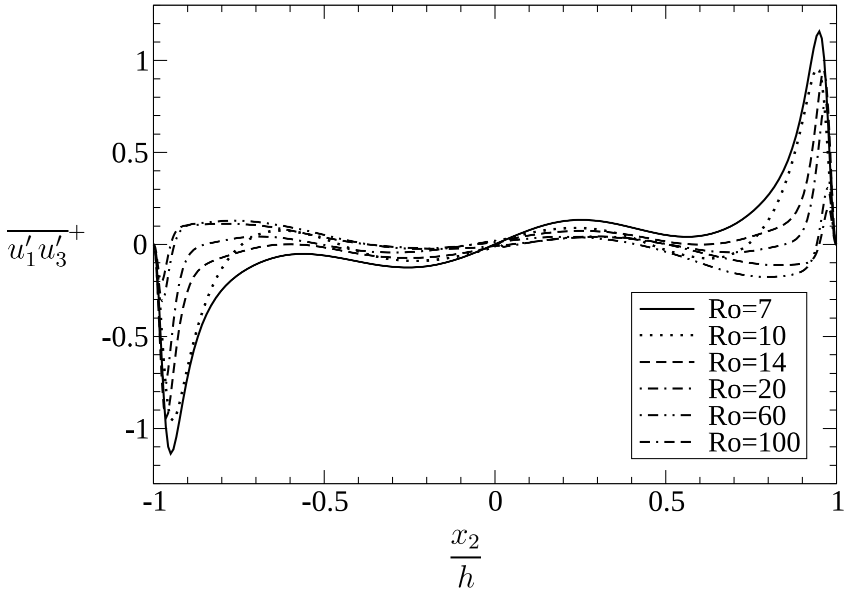

Figure 4.21: Reynolds shear stresses $\overline{u_1'u_3'}$ at different rotation rates.

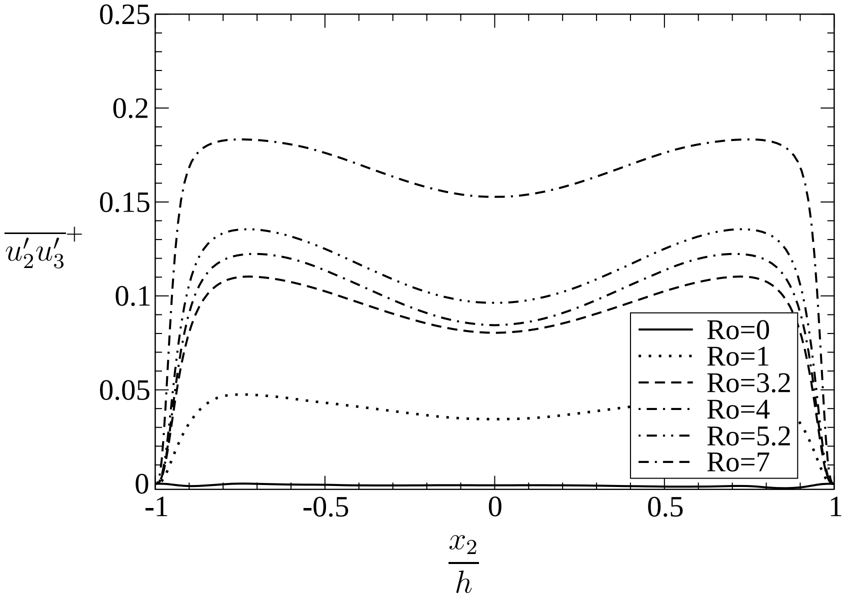

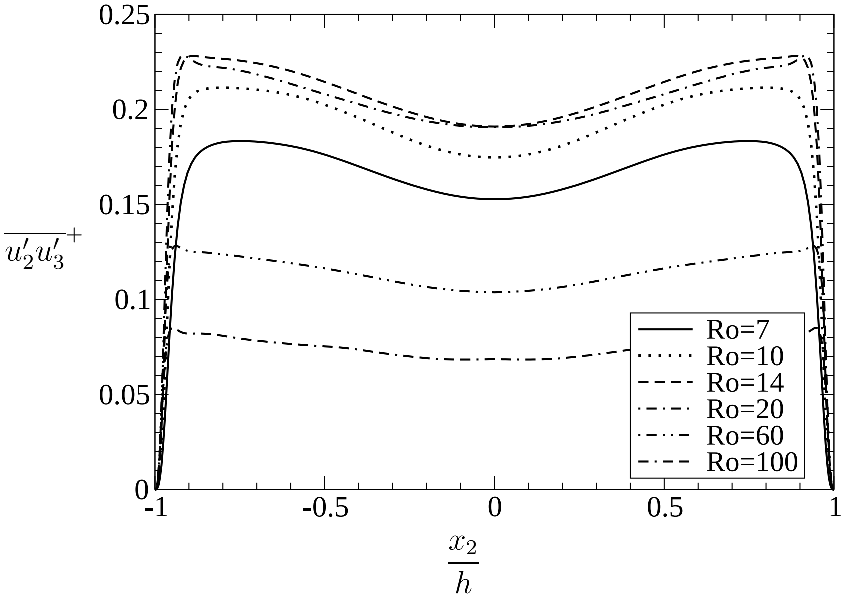

Figure 4.22: Reynolds shear stresses $\overline{u_2'u_3'}$ at different rotation rates.

This leaves

$$\frac{1}{\rho}\frac{\partial \bar{p}}{\partial x_1} = -\frac{\partial}{\partial x_2}\,\overline{u_1' u_2'}, \tag{4.6}$$

which means, that the shear stress primarily depends on the pressure gradient and hence is entirely independent of the rotation rate. Since Re_τ and therefore $\partial \bar{p}/\partial x_1$ is kept constant at different rotation rates, $\overline{u_1' u_2'}$ would be expected to have the same gradient for the linear line section over the channel height at all rotation speeds.

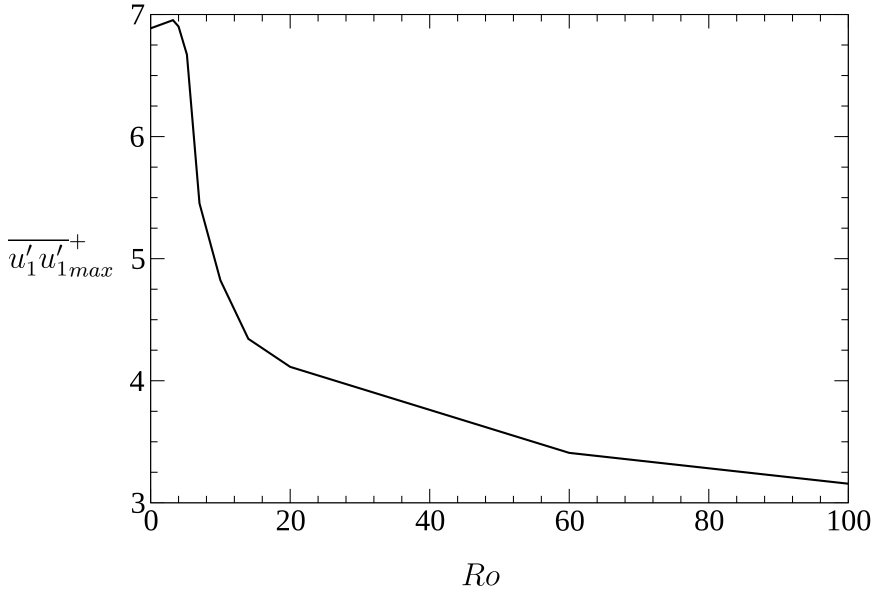

Figure 4.23: Development of $\overline{u_1' u_1'}_{1max}$ as a function of the rotation rate.

For the shear stresses $\overline{u_1' u_3'}$ and $\overline{u_2' u_3'}$ the same RDE such as for the spanwise mean velocity profiles is noticeable. Both shear stresses increase for small rotation rates and reverse respectively at $Ro = 10$.

In particular significant decays of the maximum velocity are visible beetween $Ro = 5.2$ and 10 at $\overline{u_1' u_1'}$. A more detailed view of this effect can be taken from figures 4.23, where the development of $\overline{u_1' u_1'}_{1max}$ is plotted over the rotation rate. This indicates also a change in the fluid dynamics.

4.3.4.4 Comparison to Experimental Data

In addition to the numerical findings, an experiment was conducted by I. Recktenwald and W. Schröder at the RWTH Aachen to confirm the results of theory and to compare to the the DNS data.

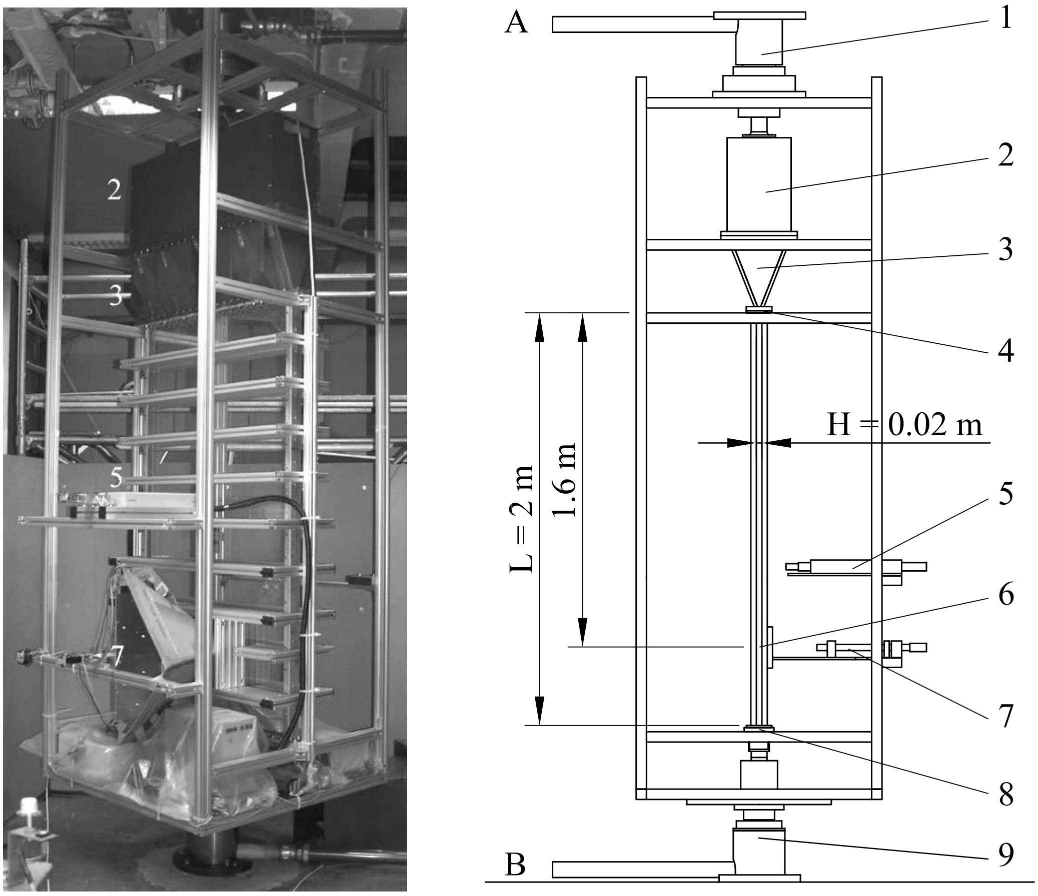

Figure 4.24: Setup of the rotating channel section: A: Inlet; B: Outlet; 1: Rotating union; 2: Flow straightener; 3: Inlet hopper; 4: Tripping edge at channel inlet; 5: Laser mount; 6: Location of the measuring section; 7: Camera mount; 8: Channel outlet; 9: Rotating union.

The measurements were done in a rotating channel with a length of $l = 2\ m$, a width of $w = 1\ m$, and a height of $h = 0.02\ m$. A sketch of the channel and the details of the complete setup are shown in figure 4.24.

The Reynolds number $Re_m = U_1\ (h/2)/\nu = 2850$ is determined by the mean bulk velocity

$$U_1 = \frac{1}{T}\frac{1}{A}\int_T \int_A u_1(x_2, x_3, t)\ dA\ dt \tag{4.7}$$

and the channel half-height $h/2$. During the experiments the flow rate is held constant leading to a constant Re_m.

To perform the measurements the Particle-Image Velocimetry technique (PIV) was used. PIV is a non-intrusive imaging measuring technique to determine the instantaneous velocity field. The fluid is seeded with tracer particles. The flow is illuminated by a suitable light source, usually a laser light sheet, and two pictures of the flow field are taken at a given time difference, such that the velocity can be calculated from the spatial deviation of the particles.

The basic system consisted of two PCO SensiCam CCD double-shutter cameras with a resolution of $1280 \times 1024\ px$ in conjunction with double-sided telecentric lenses. The cameras and lenses satisfied the Scheimpflug condition such that the pictures remained orthogonal. Details of the camera setup are shown in figure 4.25.

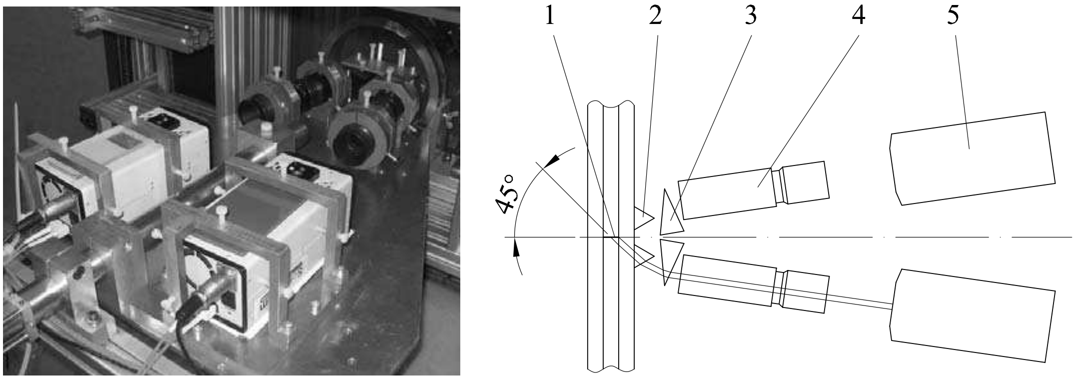

Figure 4.25: Setup of the stereoscopic camera system: 1: Measuring section; 2: Decoupling prism; 3: Correction prism; 4: Double-sided telecentric lenses; 5: CCD double-shutter camera. Two exemplary rays with an observation angle of 45° onto the measuring plane are displayed to illustrate the path of the laser light through the optical setup.

The measurements were made in the non-rotating and in the rotating channel at three rotational speeds $f = 0.46\ Hz, 0.75\ Hz$, and $1.0\ Hz$ leading to Rossby numbers $Ro_m = U_1/f\ h$ of $Ro_m = \infty$ for the non-rotating case and $Ro_m = 65.2$, 40, and 30 for the rotating cases, respectively. Using the relation between the angular velocity Ω and f, i.e., $\Omega = \pi f$, these values correspond to rotation numbers $Ro_\tau = 0, 3.2, 5.2$ and 7. More details on the experimental setup can be obtained from Recktenwald et. al. (Recktenwald, Weller, Schröder & Oberlack 2006)

Compared to the DNS the flow field coincides with the case $Re_\tau = u_\tau\ (h/2)/\nu = 180$, where u_τ is the friction velocity. Note, that the friction velocity was not measured in the experiments. Therefore, to make a comparison of the data possible, in all subsequent figures the velocities are normalized by the mean bulk velocity U_1. The numerical results are shown on the left-hand side of the figures, while the experimental results appear on the right-hand side.

Fig. 4.26 shows the streamwise mean velocity profiles $\bar{u}_1$ scaled with the mean bulk velocity U_1. On one hand, the profiles decrease along the channel axis with increasing rotation rate and on the other hand, they grow closer to the wall.

Note, in the experiments the wall-shear stress varies since the flow rate is held constant for the different flow conditions. In the DNS, however, the friction velocity based Reynolds number Re_τ or equivalently the pressure gradient is kept constant, which leads to a slightly changing mass flow in the different computations. Nonetheless, using the bulk velocity to normalize the data the numerical and experimental results of the mean velocity distributions possess a good agreement.

Fig. 4.27 displays the spanwise mean velocity profiles $\bar{u}_1$, which are also scaled with the mean bulk velocity U_1. The cross flow could also be verified in the experiment. Near the wall the cross flow becomes increasingly pronounced at a higher rotational speed. Close to the channel axis this flow is much less distinct and possesses a tendency to reverse the flow direction at higher rotation rates. A distinct reverse flow region, however, is only observed in the DNS velocity profiles.

The DNS results are different in the region near the rotation axis. A pronounced reverse flow develops compared to the experiment and the maximum $\bar{u}_3$-velocity near the wall is slightly higher than in the experiment. Since the values are normalized by U_1, the increased velocity might be explained by the reduced mean bulk velocity. The distributions, however, should develop similarly even at reduced mean flow rates, since they depend mostly on the fluctuations and the rotational speed.

Taking into account that the mean bulk velocity in the numerical analyses is decreasing and thus it is successively too low with increasing rotation number when

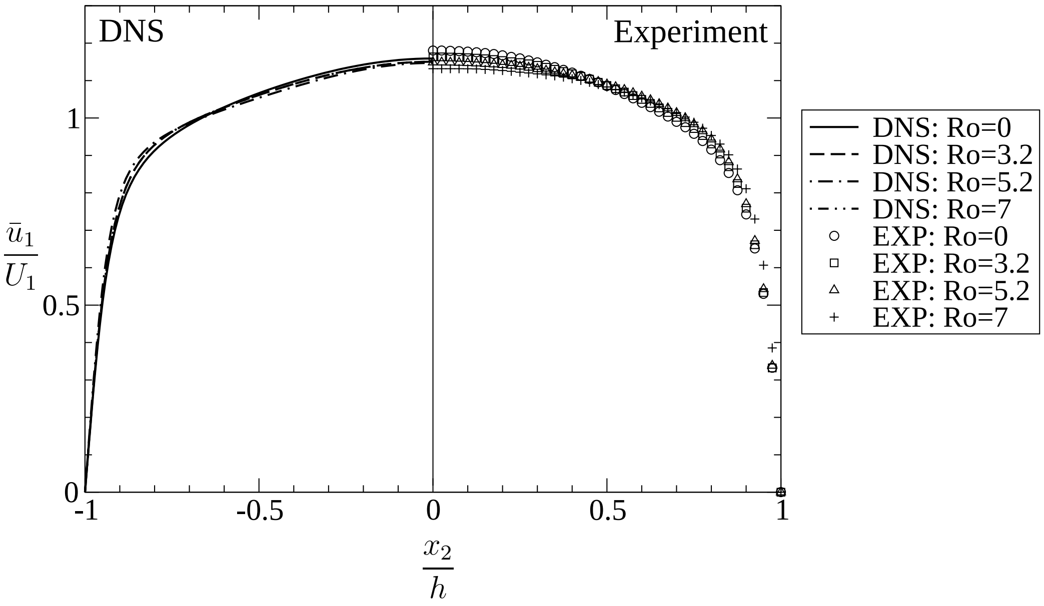

Figure 4.26: Comparison of streamwise mean velocity profiles u_3.

compared to the experimental investigations, the development of the secondary profiles with the rotation rate agrees fairly well near the wall region.

Note that both experiment and DNS are not geometrically congruent in a strict sense since the DNS employs periodicity in the spanwise direction while this is impossible in the experiment.

The comparison of the experimental results of the non-rotating channel with the numerical data evidences one of the problems with the turbulence statistics retrieved from PIV. Due to the averaging and the interpolation both necessary in the correlation process and the stereoscopic reconstruction the RMS-values of the flow are determined somewhat too low (fig. 4.28-4.30).

The reason for the RMS-distribution of the u_2-component in the experiment in fig. 4.29 to be too large lies in the stereoscopic reconstruction process. While both other directions can be measured directly with one of the two different light sheet orientations, the wall normal component has to be calculated in either case. Therefore, this component possesses the highest error sensitivity. Even slight defects in the light sheet angles cause the u_2-component and thus the according fluctuation to become marginally contaminated by fractions of the streamwise velocity u_1.

Nonetheless, the DNS and PIV data yield likewise tendencies and similar qualitative distributions for the Reynolds normal stresses, i.e., the values increase at growing rotation rates. The more pronounced growth in the DNS data, especially

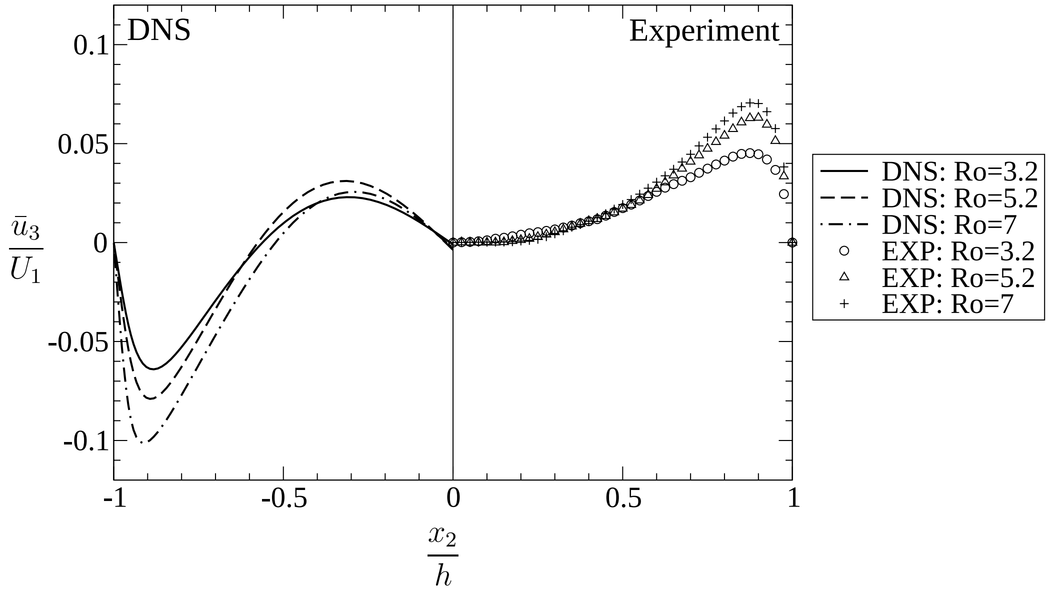

Figure 4.27: Comparison of spanwise mean velocity profiles u_3.

at the highest rotation rate, is partially caused by the normalization, which does overestimate the fluctuations compared to the decreased mean bulk velocity.

The analysis of the shear stress data in fig. 4.31-4.33 evidences the dependence on the reference velocity since the $\overline{u_i'u_j'}$-terms are normalized by the square of U_1. While the experimental results show only a small increase of the shear stress, the pronounced growth in the DNS distributions can only be attributed to the smaller reference velocity. The necessity of the friction velocity to prescribe the boundary conditions for the DNS computations reduces the resulting mean bulk velocity at the highest rotation by about 18%.

The shear stresses containing the spanwise fluctuation u_3' experience the most pronounced change, i.e., they become non-zero under rotation. Both distributions increase significantly in a rotating system, i.e., they possess a similar behavior of the RMS values. Even though the scatter of the experimental data for the $\overline{u_2'u_3'}$-distributions is higher than in the figures of the other shear stresses, the tendency is evident. Using the argument about the mean mass flow discussed above clearly reduces the DNS data such that the experimental and numerical results will have similar distributions especially near the axis of rotation.

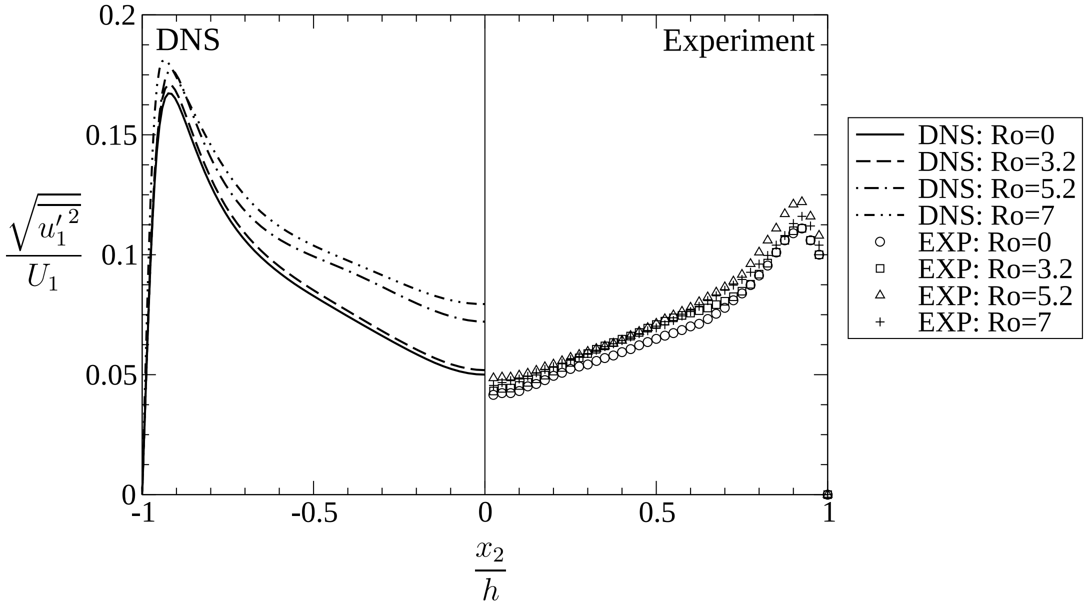

Figure 4.28: Comparing of Reynolds normal stress $\overline{u_1'u_1'}$.

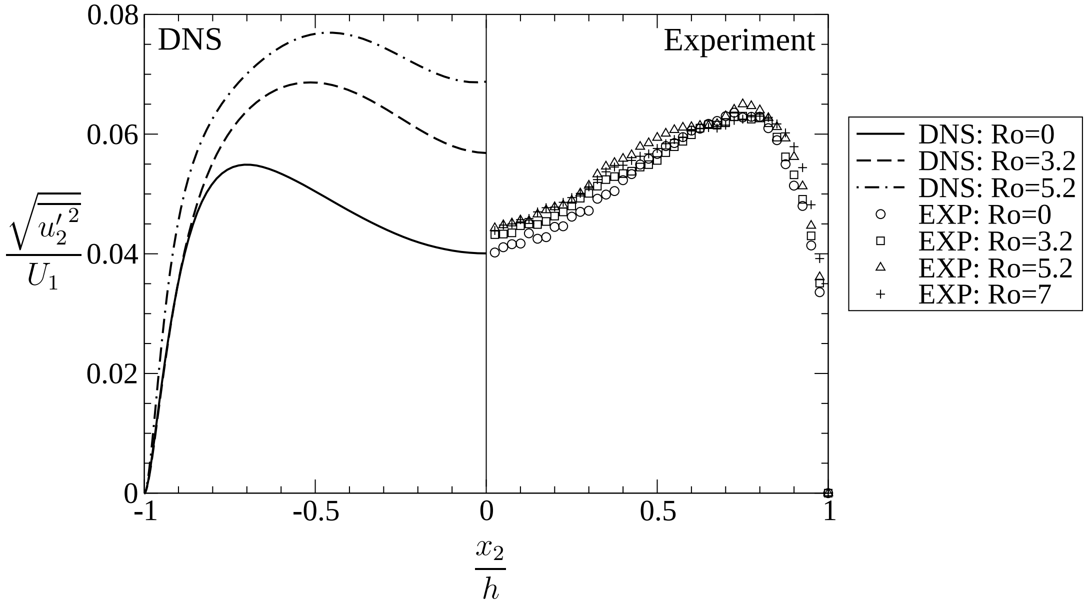

Figure 4.29: Comparing of Reynolds normal stress $\overline{u_2'u_2'}$.

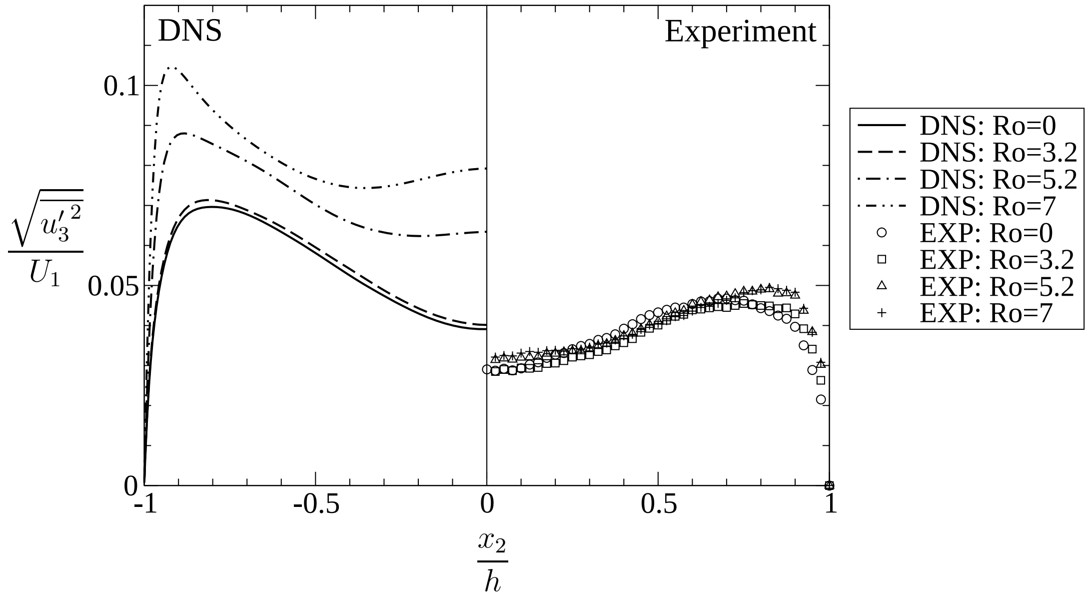

Figure 4.30: Comparing of Reynolds normal stress $\overline{u_3' u_3'}$.

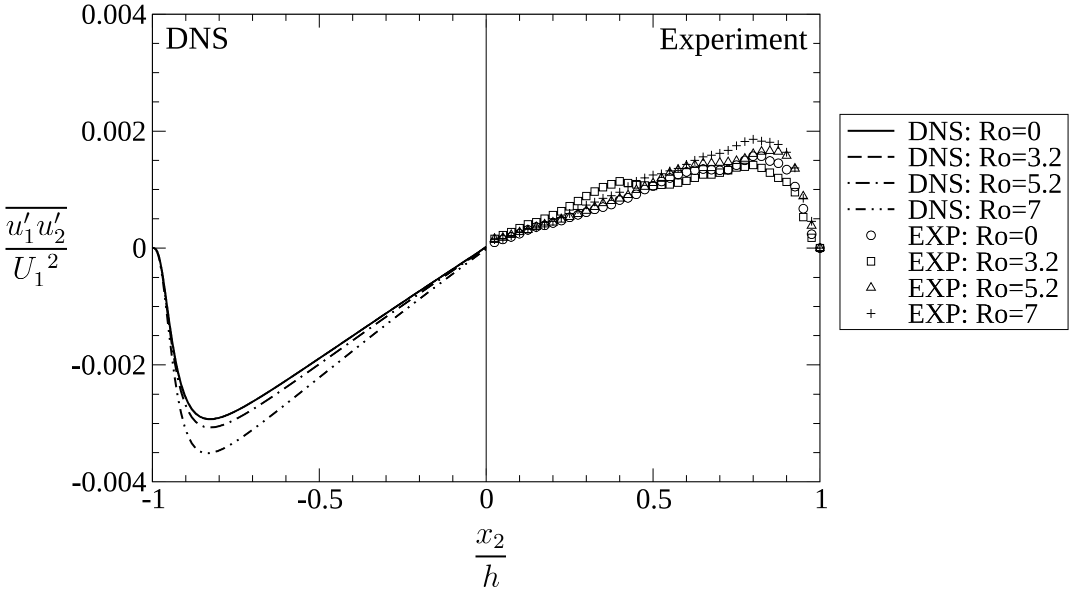

Figure 4.31: Comparing of Reynolds shear stress $\overline{u_1' u_2'}$.

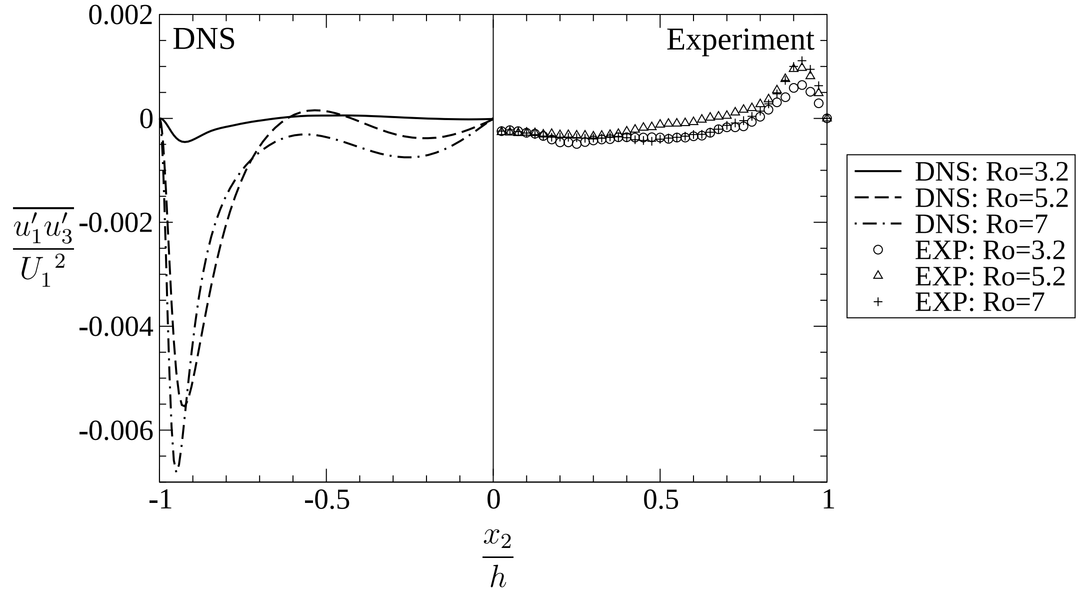

Figure 4.32: Comparing of Reynolds shear stress $\overline{u_1'u_3'}$.

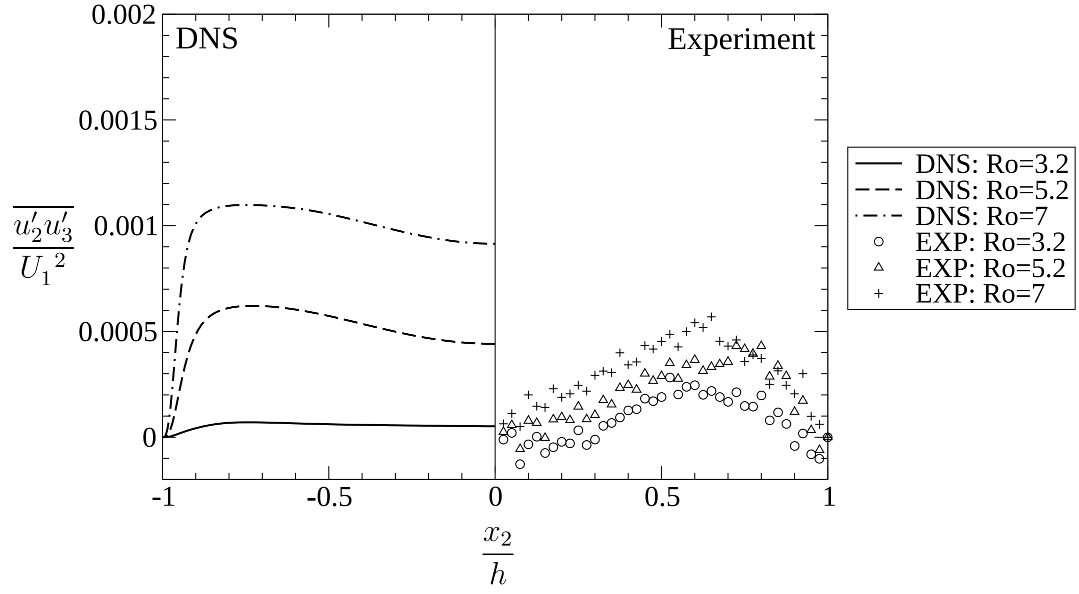

Figure 4.33: Comparing of Reynolds shear stress $\overline{u_2'u_3'}$.

4.3.4.5 Isosurfaces of the Velocity Fields

In figures 4.34 - 4.42 the isosurfaces of the fluctuations of the wall-normal velocity field are presented at the instantaneous time unit $t \simeq 10000\frac{h/2}{u_{cl}}$ for the non-rotating case and eight different rotation rates up to $Ro = 100$. To compare the figures, the same value $u_2' = 0.018$ for the visualizations of the isosurfaces is used, which is normalized on the centerline velocity u_{cl}.

At this point it was renounced to normalize u_2' on the friction velocity u_τ, because u_τ is depending directly on the Reynolds number and in the following section 4.5 these results are compared to these at higher Reynolds numbers. This simplification makes it only possible to use the same value $u_2' = 0.018$ for all visualizations of the isosurfaces at different Reynolds numbers.

At $Re_\tau = 180$ u_2' is approximately located in the interval from -0.0466 to 0.0786. Table 4.3 gives a more precise overview about the minimum and maximum values of u_2' at different rotation rates. In general a value of $u_2' = 0.018$ represents rather a smaller scale of the spectrum.

Table 4.3: Minimum and maximum values of u_2' at $Re_\tau = 180$.

Ro	$u'_{2_{min}}$	$u'_{2_{max}}$
0	-0.0466	0.0505
1	-0.0532	0.0577
3.2	-0.0580	0.0585
4	-0.0548	0.0664
5.2	-0.0529	0.0568
7	-0.0610	0.0683
10	-0.0606	0.0696
14	-0.0659	0.0649
20	-0.0653	0.0689
60	-0.0780	0.0829
100	-0.0857	0.0786

For the non-rotating case and at $Ro = 1$ the velocity fields appear disordered, at $Ro = 3.2, 4$ and 5.2 only small structures are visible. From $Ro = 7$ up to $Ro = 20$ many large turbulent structures are formed, which are growing with an increasing rotation rate. At least at $Ro = 100$ the turbulent structures extend through the whole channel of a length of 32π. Apparently with increasing rotation number increasingly elongated turbulent structures are formed. This means that the growing of the structures strongly depends on the rotation rate.

Furthermore, in figure 4.43 subdomains of the same size are presented for all simulations (1-11). Each subzone has a size of $4\pi \times 2 \times 1\pi$. Primarily the subdomains give the possibility to compare the size and number of the structures directly, which is not given in figures 4.34 - 4.42 because of the different box lenghts. The other advantage is to have a better zoom of the velocity structures.

The illustration emphasizes that elongated structures in the streamwise direction are established due to the rotation. The structures are allocated in the whole channel. In the non-rotating case only small and disordered structures are visible, while coherent structures drastically increase with growing rotation number. In this subdomains, also an increase of the radial extent of the vortices is observed up to $Ro = 20$, for higher rotation rates the turbulent structures become thinner again.

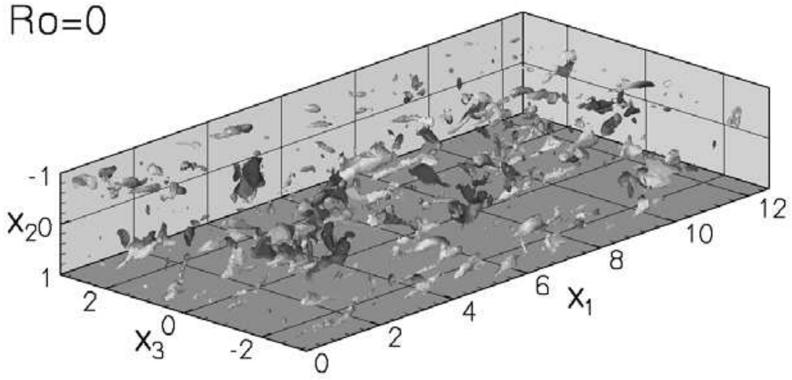

Figure 4.34: Isosurfaces of the wall-normal velocity field at $u_2' = 0.018$ at $Ro = 0$.

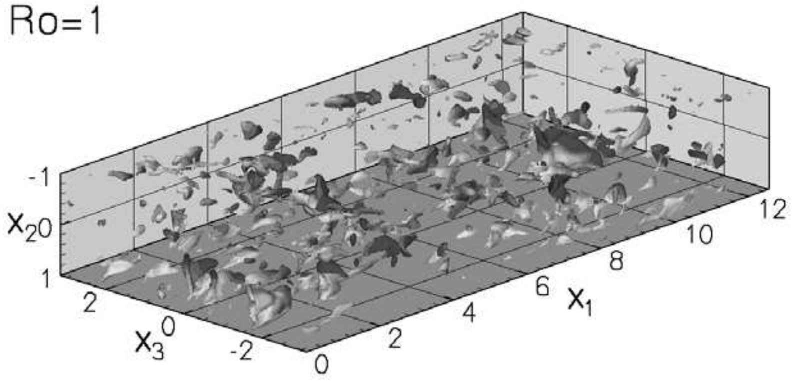

Figure 4.35: Isosurfaces of the wall-normal velocity field at $u_2' = 0.018$ at $Ro = 1$.

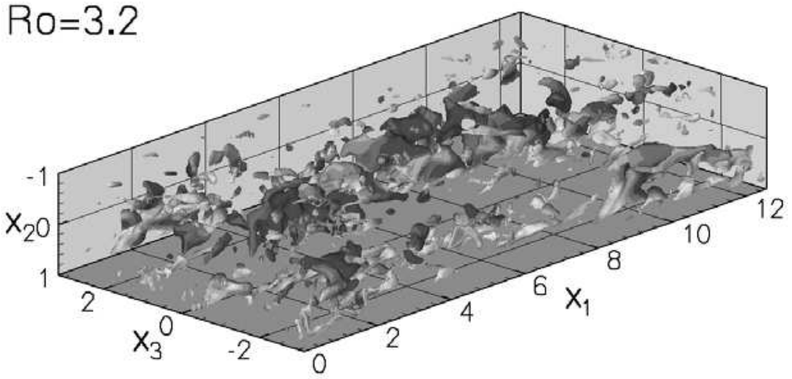

Figure 4.36: Isosurfaces of the wall-normal velocity field at $u_2' = 0.018$ at $Ro = 3.2$.

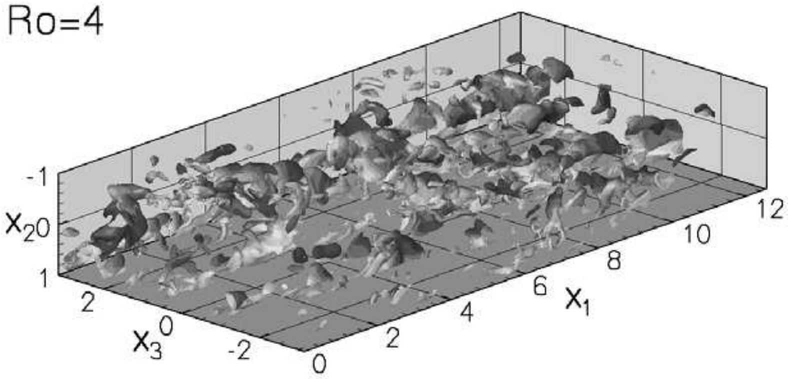

Figure 4.37: Isosurfaces of the wall-normal velocity field at $u_2' = 0.018$ at $Ro = 4$.

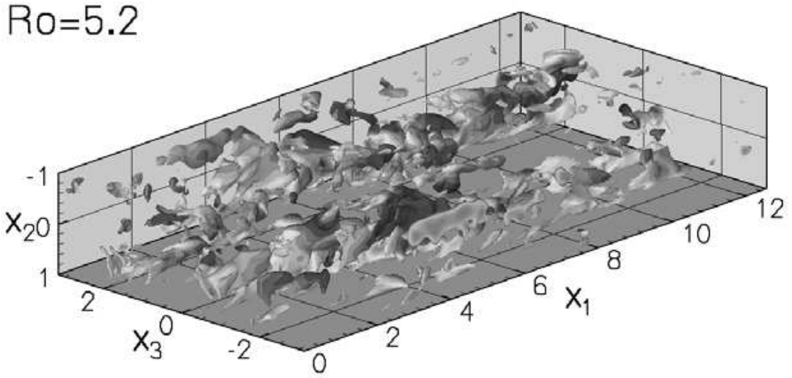

Figure 4.38: Isosurfaces of the wall-normal velocity field at $u_2' = 0.018$ at $Ro = 5.2$.

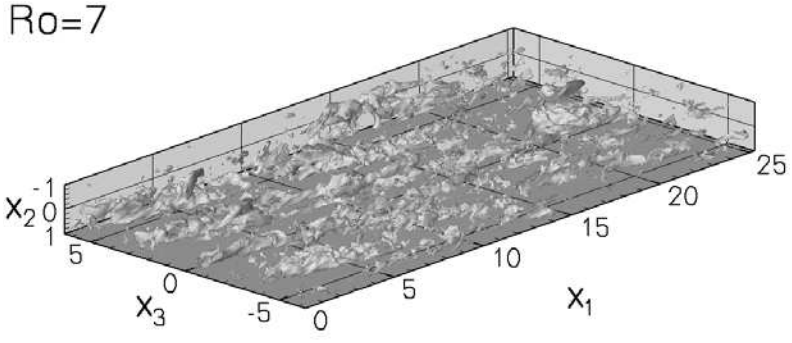

Figure 4.39: Isosurfaces of the wall-normal velocity field at $u_2' = 0.018$ at $Ro = 7$.

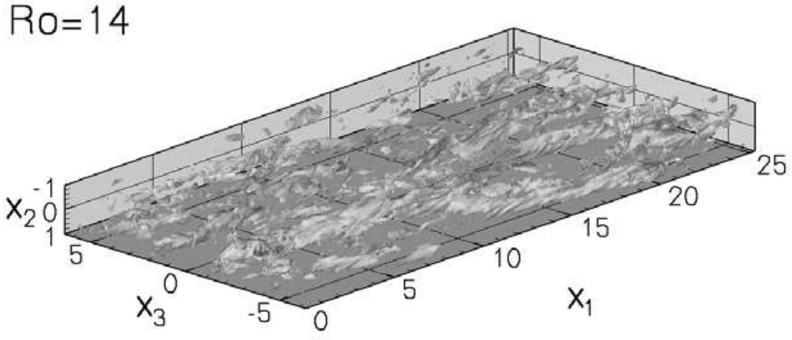

Figure 4.40: Isosurfaces of the wall-normal velocity field at $u_2' = 0.018$ at $Ro = 14$.

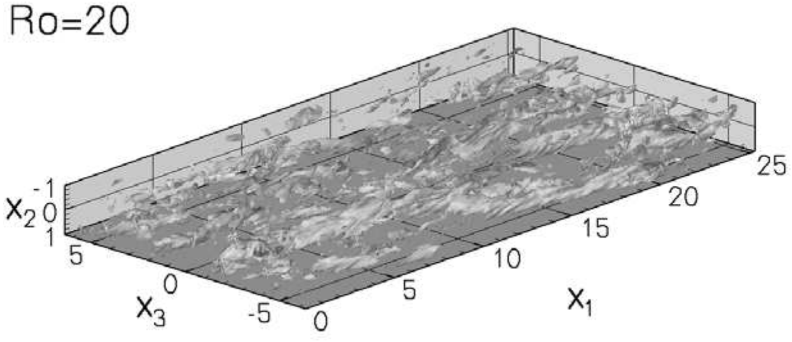

Figure 4.41: Isosurfaces of the wall-normal velocity field at $u_2' = 0.018$ at $Ro = 20$.

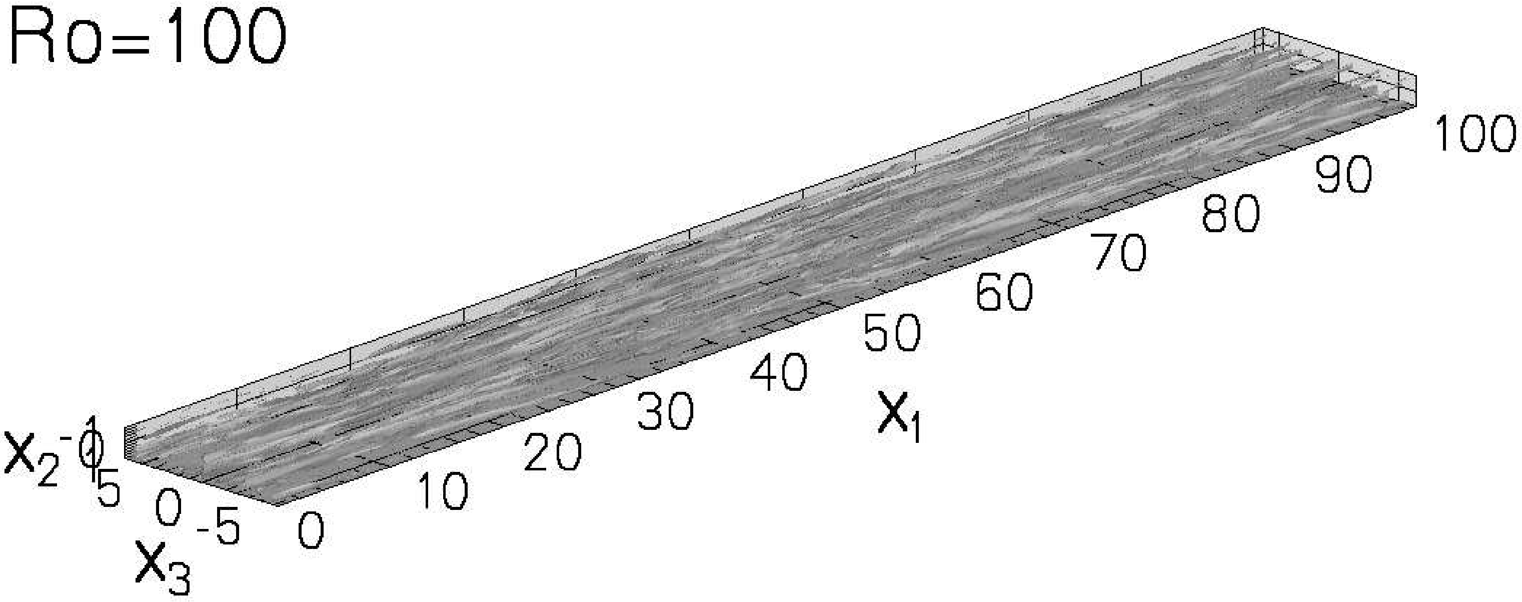

Figure 4.42: Isosurfaces of the wall-normal velocity field at $u_2' = 0.018$ at $Ro = 100$.

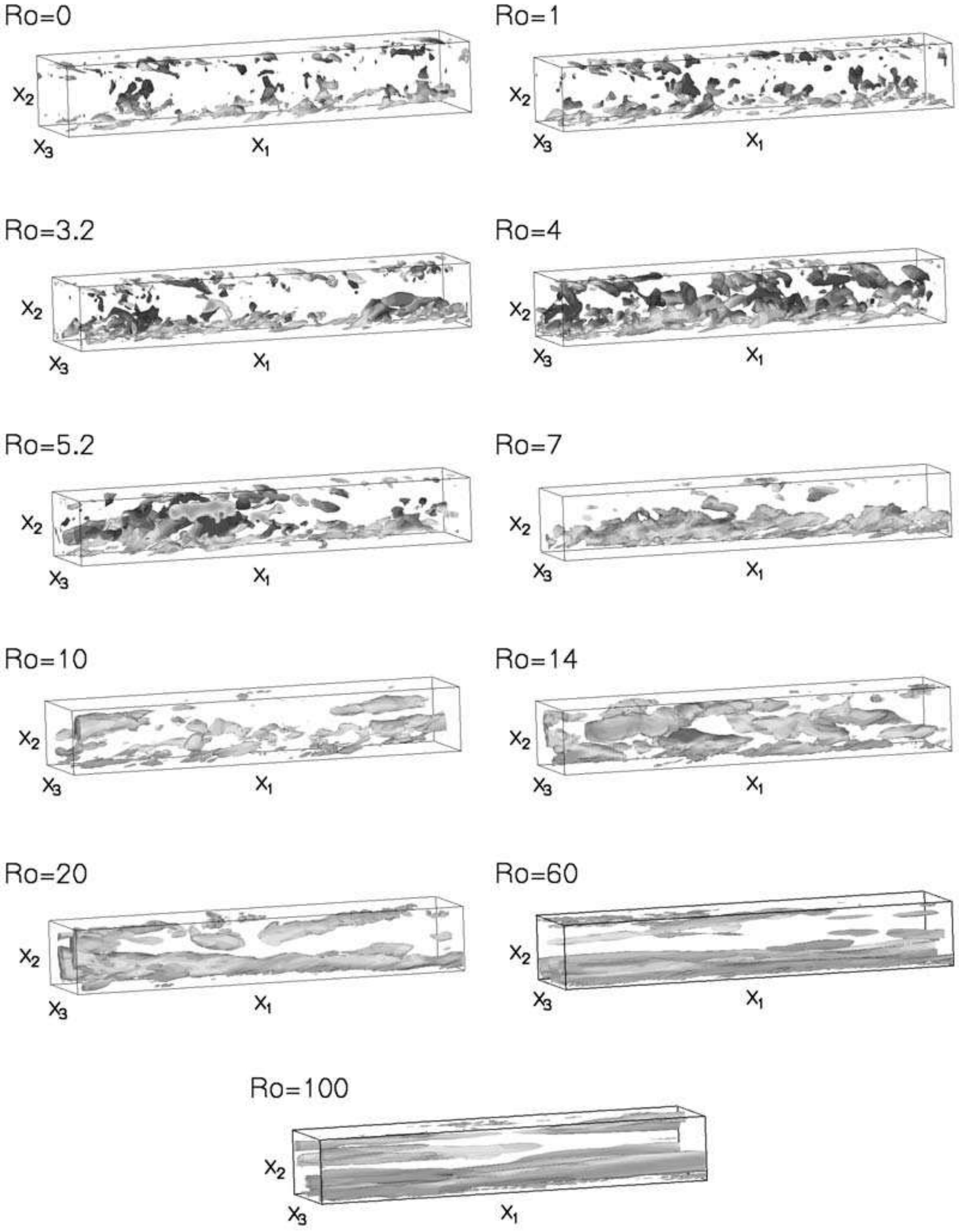

Figure 4.43: Subzones of equivalent size of isosurfaces of the wall-normal velocity fields at $u_2' = 0.018$ at different rotation rates.

4.3.4.6 Isosurfaces of the Vorticity Fields

In figures 4.44 - 4.48 the isosurfaces of the fluctuations of the streamwise vorticity field are presented at the instantaneous time unit $t \simeq 10000\frac{h/2}{u_{cl}}$ for the non-rotating case and four different rotation rates up to $Ro = 100$. For all figures the same value $\omega_1' = \pm 2$ for the visualizations of the isosurfaces is used, which is normalized on the centerline velocity u_{cl}.

Analogously to sec. 4.3.4.5 it was also renounced to normalize ω_1' on the friction velocity u_τ. At $Re_\tau = 180\,\omega_1'$ is approximately located in the interval from -6.2073 to 11.4418. Table 4.4 gives a more precise overview about the minimum and maximum values of ω_1' at different rotation rates. In general a value of $\omega_1' = \pm 2$ represents rather a smaller scale of the spectrum.

Table 4.4: Minimum and maximum values of ω_1' at $Re_\tau = 180$.

Ro	$\omega'_{1_{min}}$	$\omega'_{1_{max}}$
0	-6.7440	7.0287
1	-6.8737	5.5292
3	-6.7603	5.7444
4	-6.2073	7.8810
5	-7.3359	6.2114
7	-6.2673	6.7907
10	-6.8193	6.6555
14	-7.4159	6.7947
20	-7.8332	7.3783
60	-7.0484	11.4418
100	-9.3228	8.5718

The illustrations for the non-rotating case and at $Ro = 4$ show very similar vorticity structures. The structures at $Ro = 10$ and $Ro = 20$ seems to be thinner. Only at $Ro = 100$ much longer structures are clearly visbile. More details can be obtained by analysing subdomains of the same size. Therefore, subzones of the size, respectively $4\pi \times 2 \times 1\pi$, were extracted for all simulations (1-11).

The illustrations for the non-rotating case and at $Ro = 4$ show very similar vorticity structures. The structures at $Ro = 10$ and $Ro = 20$ seems to be thinner. Only at $Ro = 100$ much longer structures are clearly visbile. More details can be obtained by analysing subdomains of the same size. Therefore, subzones of the same size, respectively $4\pi \times 2 \times 1\pi$, were extracted for all simulations (1-11).

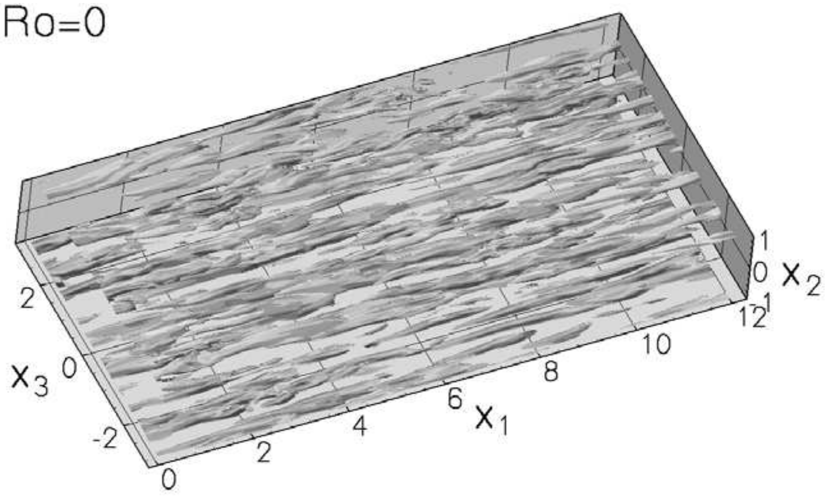

Figure 4.44: Isosurfaces of the streamwise vorticity field at $\omega_1' = \pm2$ at $Ro = 0$.

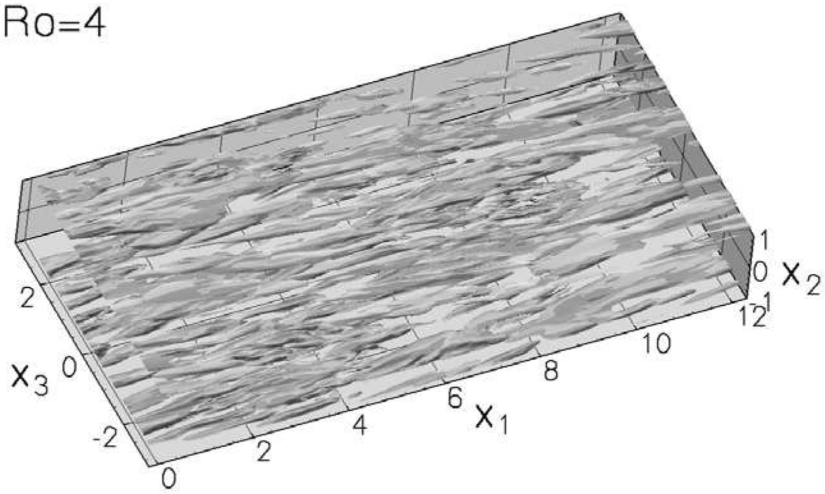

Figure 4.45: Isosurfaces of the streamwise vorticity field at $\omega_1' = \pm2$ at $Ro = 4$.

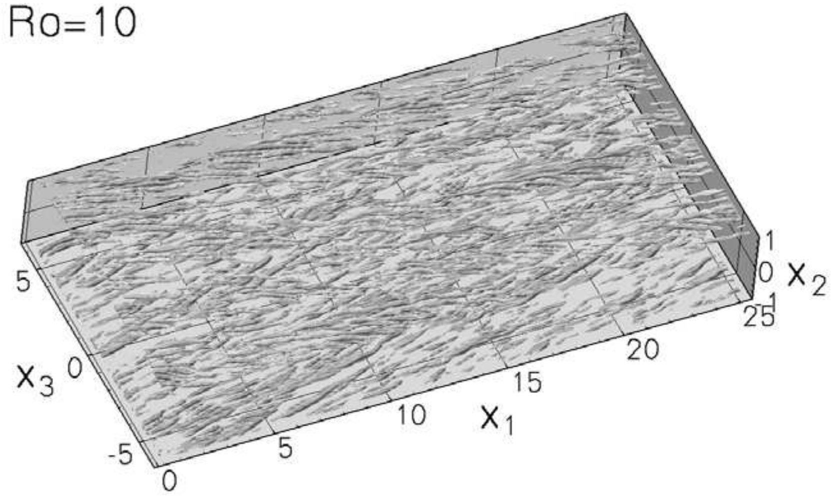

Figure 4.46: Isosurfaces of the streamwise vorticity field at $\omega_1' = \pm 2$ at $Ro = 10$.

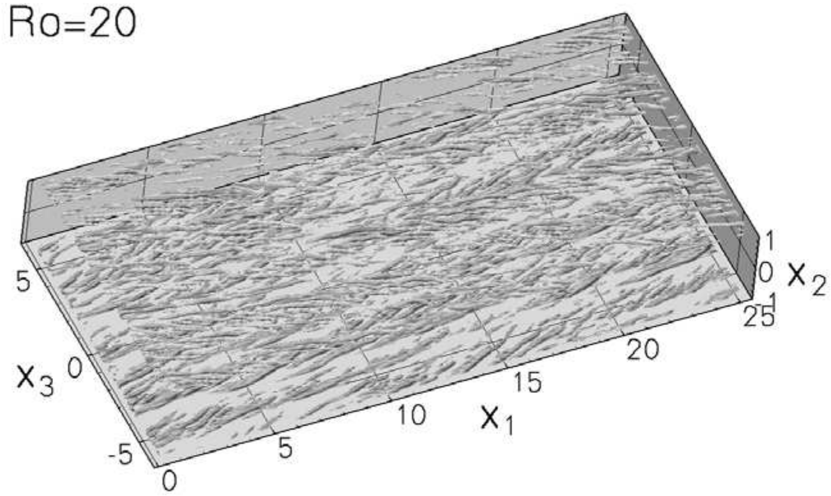

Figure 4.47: Isosurfaces of the streamwise vorticity field at $\omega_1' = \pm 2$ at $Ro = 20$.

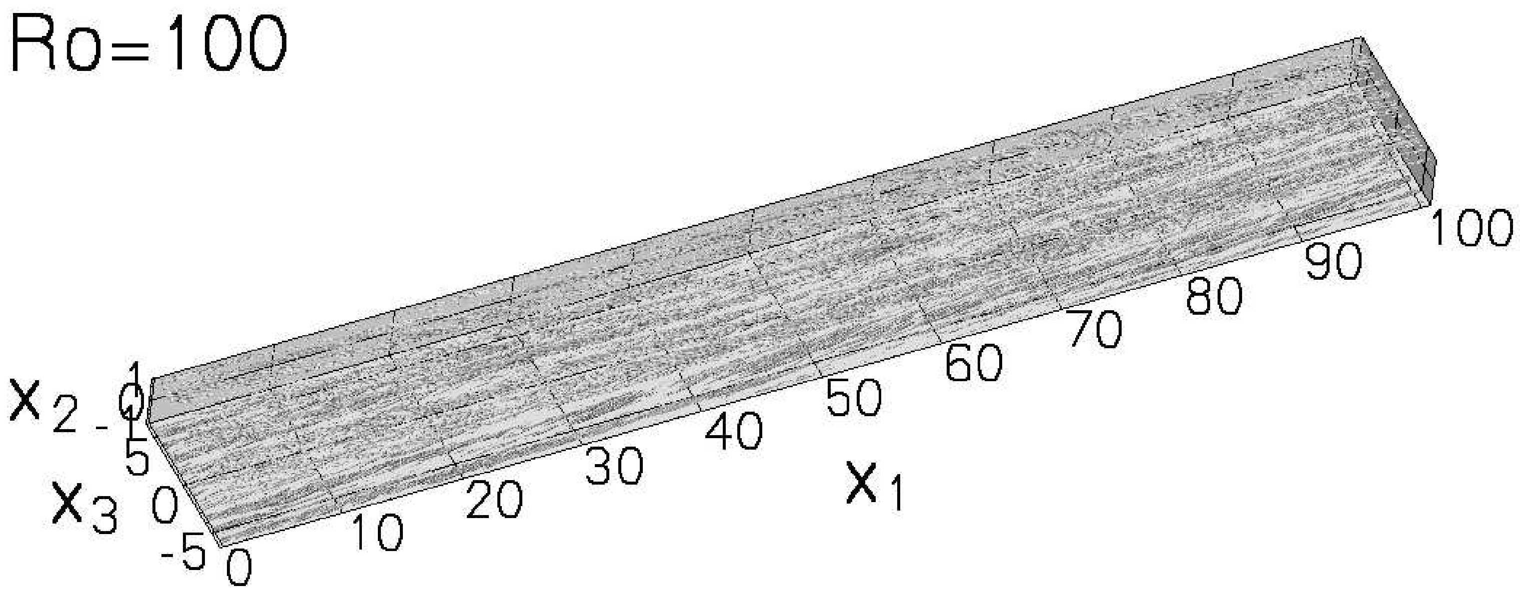

Figure 4.48: Isosurfaces of the streamwise vorticity field at $\omega_1' = \pm 2$ at $Ro = 100$.

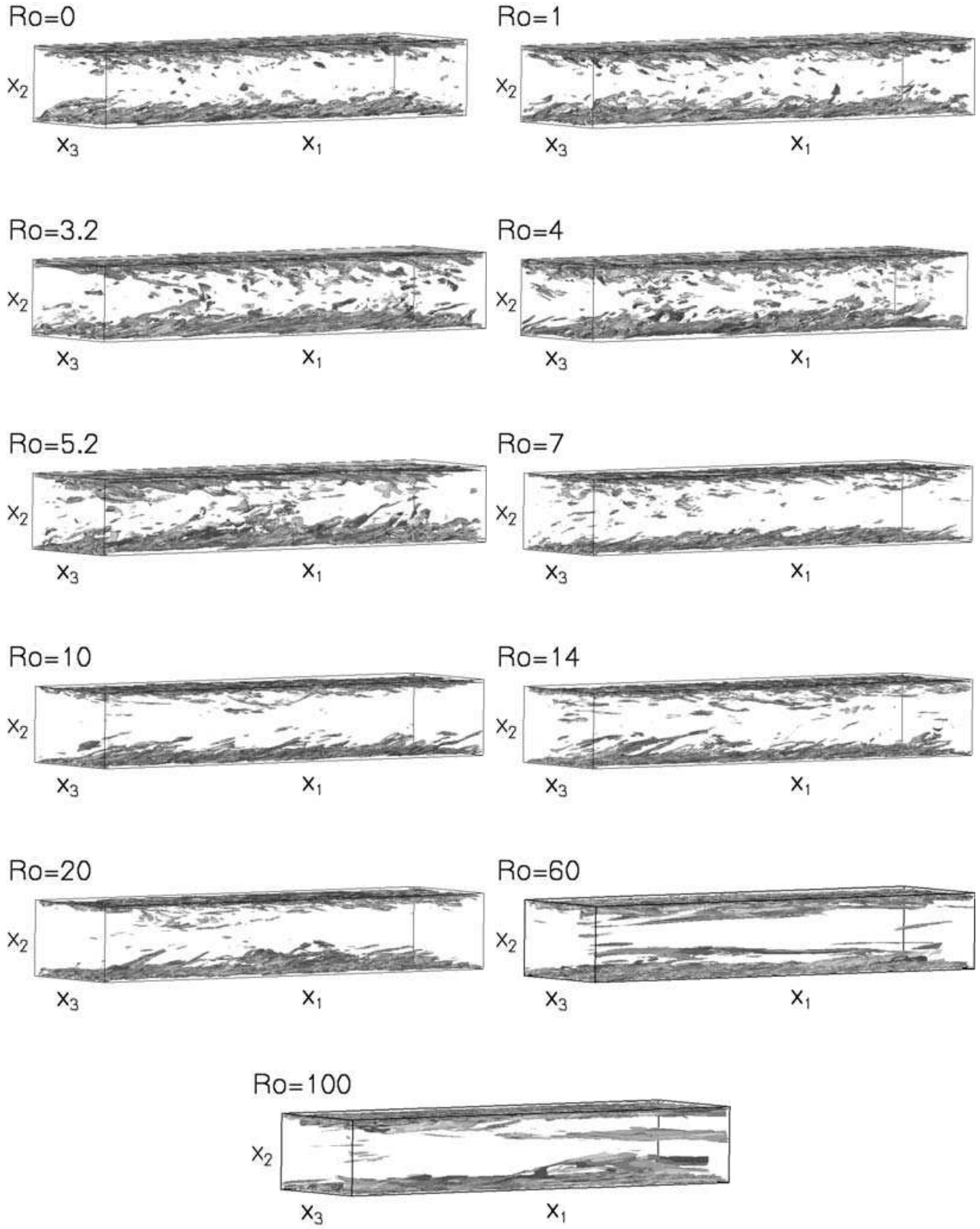

Figure 4.49: Subzones of equivalent size of isosurfaces of the streamwise vorticity fields at $\omega_1' = \pm 2$ at different rotation rates.

Moreover, in figure 4.49 the subdomains are presented. The illustration emphasizes that for small rotation rates smaller and more disordered structures are observed, while from $Ro = 10$ the structures are thinner and growing in the streamwise direction due to the rotation. In all figures the vorticies are more dense in the wall region and with increasing rotation rate less vortices appear in the middle of the channel. It seems that the vorticies are pressed against the wall due to the rotation.

4.4 Computations at $Re_\tau = 270$ and $Re_\tau = 560$

4.4.1 Computations

In the present subsection, it will be investigated if the RDE is only an effect of a rather low Reynolds number ($Re_\tau = 180$) or if it exits also at higher Reynolds numbers. Therefore, simulations were performed at two higher Reynolds numbers $Re_\tau = 270$ and $Re_\tau = 560$. Especially DNS at rotations rates of $Ro = 10$ and $Ro = 14$ were conducted, at which the RDE was found at $Re_\tau = 180$. Two additional calculations at $Ro = 4$ and $Ro = 20$ were performed to confirm the tendendies.
Table 4.5 gives an overview of the different flow cases, the computational domain, and the corresponding grid points.

Table 4.5: Computations at $Re_\tau = 270$ and $Re_\tau = 560$.

Sim.	Re_τ	Ro	Box($L_1 \times L_2 \times L_3$)	Grid($N_1 \times N_2 \times N_3$)	Grid points
12	270	4	$8\pi \times 2 \times 4\pi$	$256 \times 217 \times 256$	14.2 Mio
13		10	$8\pi \times 2 \times 4\pi$	$256 \times 217 \times 256$	14.2 Mio
14		14	$8\pi \times 2 \times 4\pi$	$256 \times 217 \times 256$	14.2 Mio
15		20	$8\pi \times 2 \times 4\pi$	$256 \times 217 \times 256$	14.2 Mio
16	560	4	$16\pi \times 2 \times 4\pi$	$640 \times 385 \times 256$	63.1 Mio
17		10	$16\pi \times 2 \times 4\pi$	$640 \times 385 \times 256$	63.1 Mio
18		14	$16\pi \times 2 \times 4\pi$	$640 \times 385 \times 256$	63.1 Mio
19		20	$16\pi \times 2 \times 4\pi$	$640 \times 385 \times 256$	63.1 Mio

To obtain smooth statistics all computations were run for $12000 \frac{h/2}{u_{CL}}$ time units and the statistics was performed using the last 7000 time units.

4.4.2 Verification of the Computational Domain

In the rotating channel flows it is necessary to use large computational boxes to capture large-scale structures. Analogously to section 4.3.2 it was prooved that the computional domains were large enough to ensure a sufficient decay to zero for the TPC functions.

Figures 4.50 and 4.52 demonstrate that at both Reynolds numbers ($Re_\tau = 270, 560$) TPC functions tend to zero. This means that in each case the computational domains were sufficient.

The comparison of the correlation functions for different Reynolds numbers shows, that the correlation areas increase not only significantly in the streamwise direction with the rotation. At the same time the correlation areas increase too with increasing Reynolds numbers. For example at $Ro = 10$ the zero-crossing is at about $x_1/h = 8$ for $Re_\tau = 180$ and increases up to $x_1/h = 10$ for $Re_\tau = 270$ and at least up to $x_1/h = 18.5$ for $Re_\tau = 560$.

As a result, it is demonstrated that larger coherent turbulent structures appear at the same rotation rate with an increasing Reynolds number.

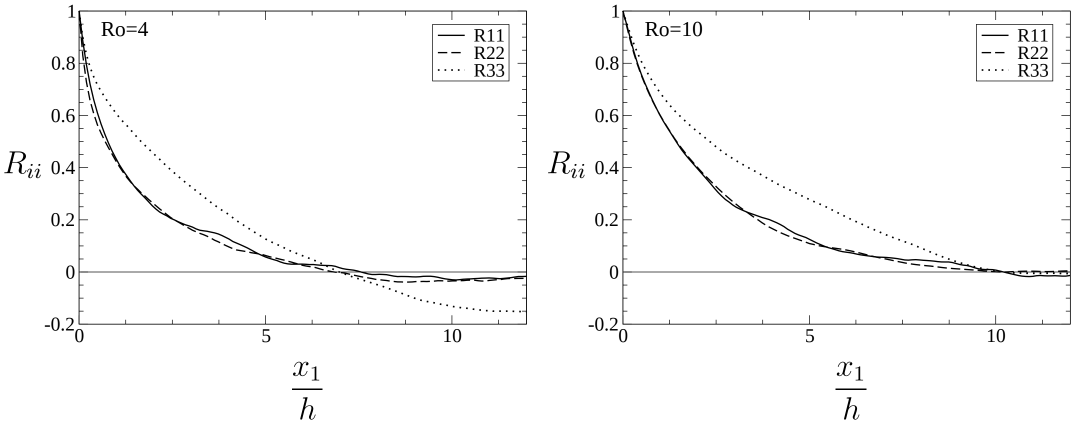

Figure 4.50: TPC R_{ii} in the streamwise direction at the centerline at $Re_\tau = 270$ and $Ro = 4$ and 10.

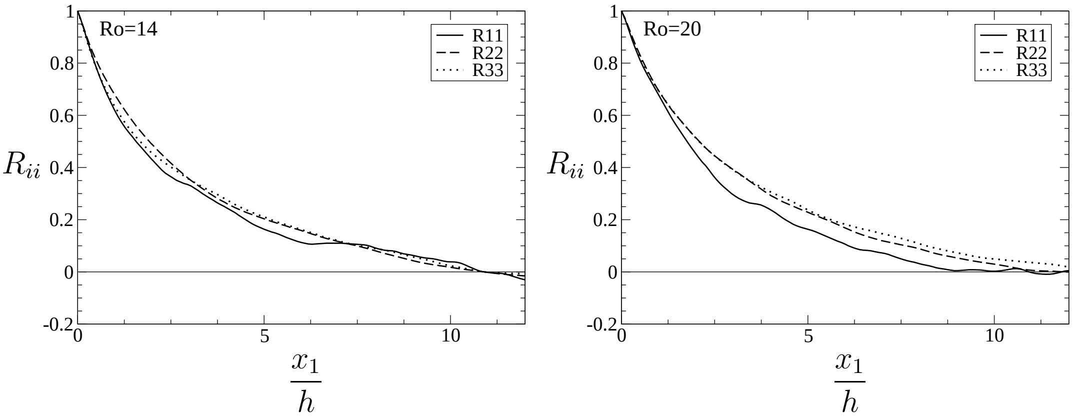

Figure 4.51: TPC R_{ii} in the streamwise direction at the centerline at $Re_\tau = 270$ and $Ro = 14$ and 20.

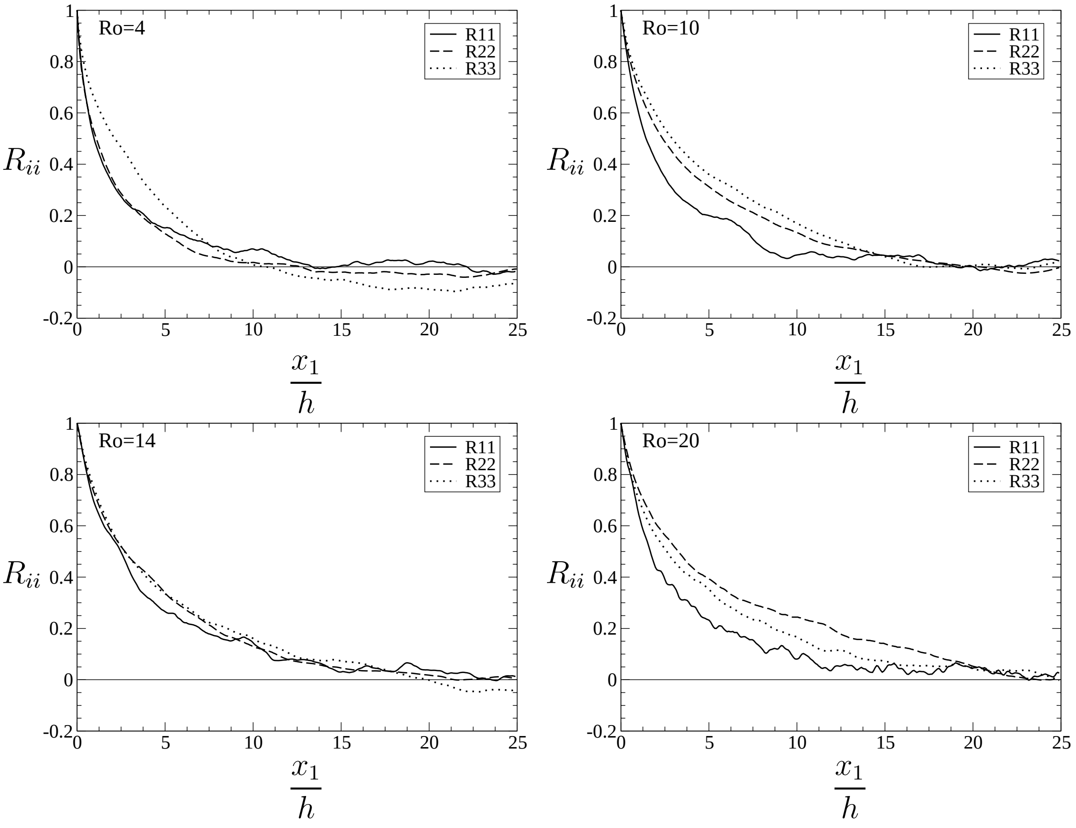

Figure 4.52: TPC R_{ii} in the streamwise direction at the centerline at $Re_\tau = 560$ and $Ro = 4, 10, 14$ and 20.

4.4.3 Verification of the Grid Resolution

The grid resolution in the streamwise and spanwise directions were at $Re_\tau = 270$, $\Delta x_1^+ \approx 26.51$ and $\Delta x_3^+ \approx 13.25$ (sim. 12-15) and at $Re_\tau = 560$ $\Delta x_1^+ \approx 43.98$ and $\Delta x_3^+ \approx 27.49$ (sim. 16-19).
Concerning the wall-normal direction the resolution at $Re_\tau = 270$ was $\Delta x_2^+ \approx 0.029$ near the wall and $\Delta x_2^+ \approx 3.927$ in the centerline and at $Re_\tau = 560$ $\Delta x_2^+ \approx 0.019$ near the wall and $\Delta x_2^+ \approx 4.581$ in the centerline respectively. The exact values are also summarized in table 4.6.

Table 4.6: Grid resolution at $Re_\tau = 270$ and $Re_\tau = 560$.

Sim.	Re	Ro	Δx_1^+	$\Delta x_2^+(WR) - \Delta x_2^+(CL)$	Δx_3^+
12-15	270	4, 10, 14, 20	26.51	0.029 - 3.927	13.25
16-19	560	4, 10, 14, 20	43.98	0.019 - 4.581	27.49

Analogously to the section 4.3.3 the grid resolution was verified by comparing the Reynolds normal stress $\overline{u_1'u_1'}^+$ at two different resolutions. The curves of the utilized resolutions of the simulations are plotted in solid lines.

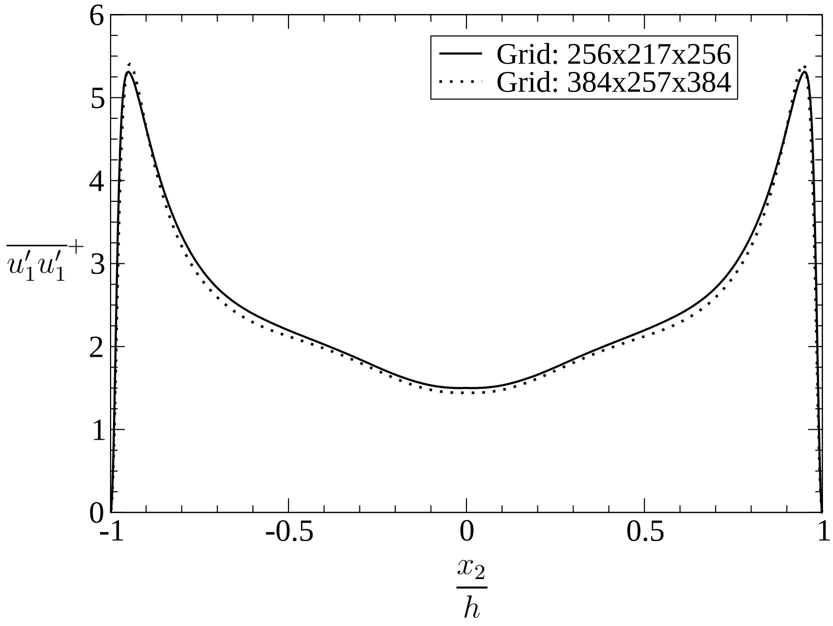

Figure 4.53: Comparison of resolutions at $Re_\tau = 270$ and $Ro = 10$ (Sim. 13).

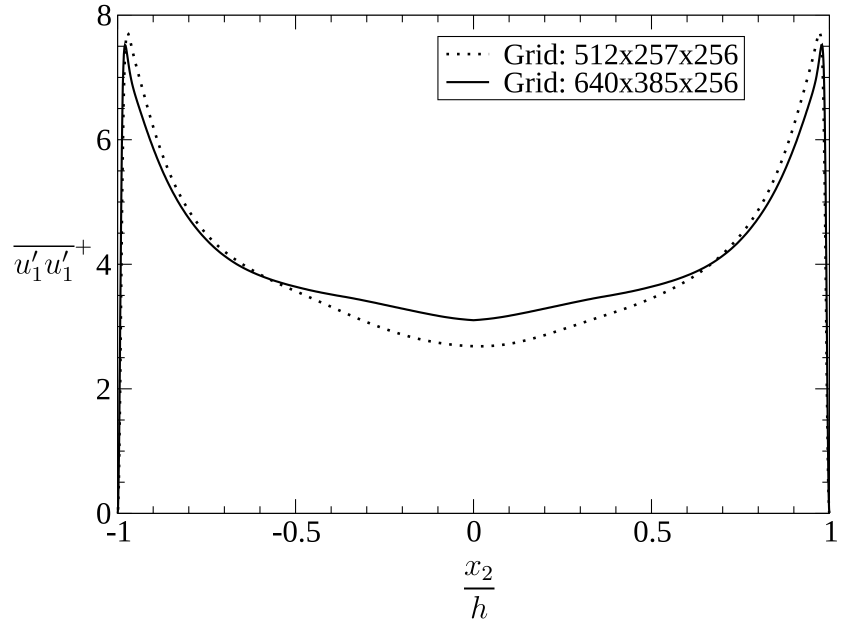

Figure 4.54: Comparison of resolutions at $Re_\tau = 560$ and $Ro = 10$ (Sim. 17).

In figures 4.53 and 4.54 the normal stress $\overline{u_1'u_1'}^+$ is plotted in each case at two different resolutions. In the first case at $Re_\tau = 270$ the curves are close to each other. For the higher Reynolds number case at $Re_\tau = 560$ some small differences are visible especially at the centerline of the profiles. In general the utilized resolutions in table 4.6 are sufficient enough for the simulations.

4.4.4 Results

4.4.4.1 Mean Velocity Profiles

Figure 4.55 compares the streamwise mean velocity profiles both at different rotation rates and three different Reynolds numbers. In general, the profiles show the same tendency as for $Re_\tau = 180$, only the maxima of the profiles are higher with increasing Reynolds numbers.

The drastic decay of the maximum velocity between $Ro = 4$ and 10 exists at $Re_\tau = 270$ and $Re_\tau = 560$ too, but is less pronounced. A more detailed view is given in fig. 4.57, where the development of the mass flux is plotted over the rotation rate. The curves for $Re_\tau = 270$ and 560 are approximately parallel, while the curve at $Re_\tau = 180$ has a sharp bend at $Ro = 10$.

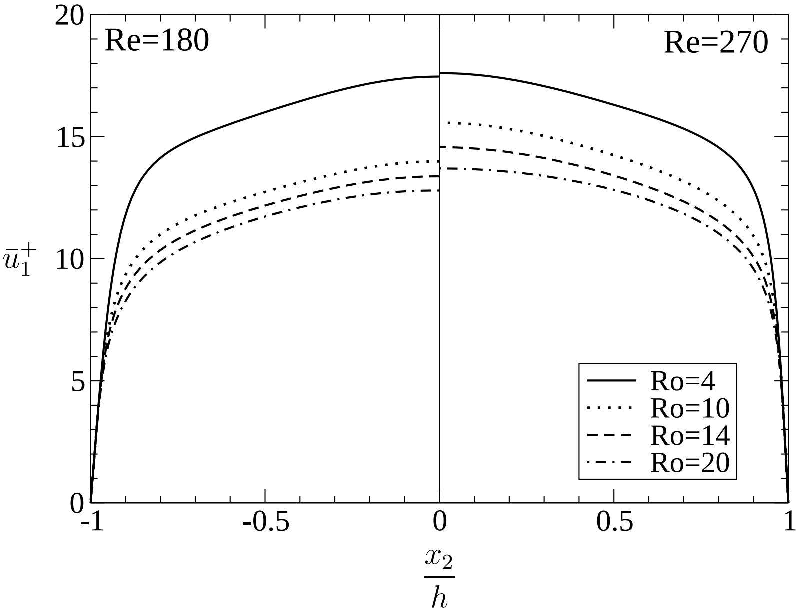

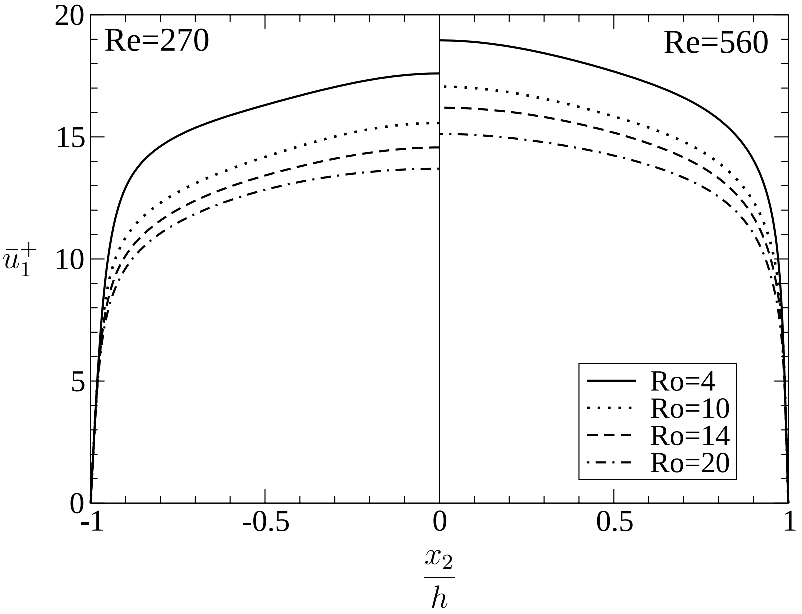

Figure 4.55: Streamwise mean velocity profiles $\bar{u}_1$ at different Reynolds numbers.

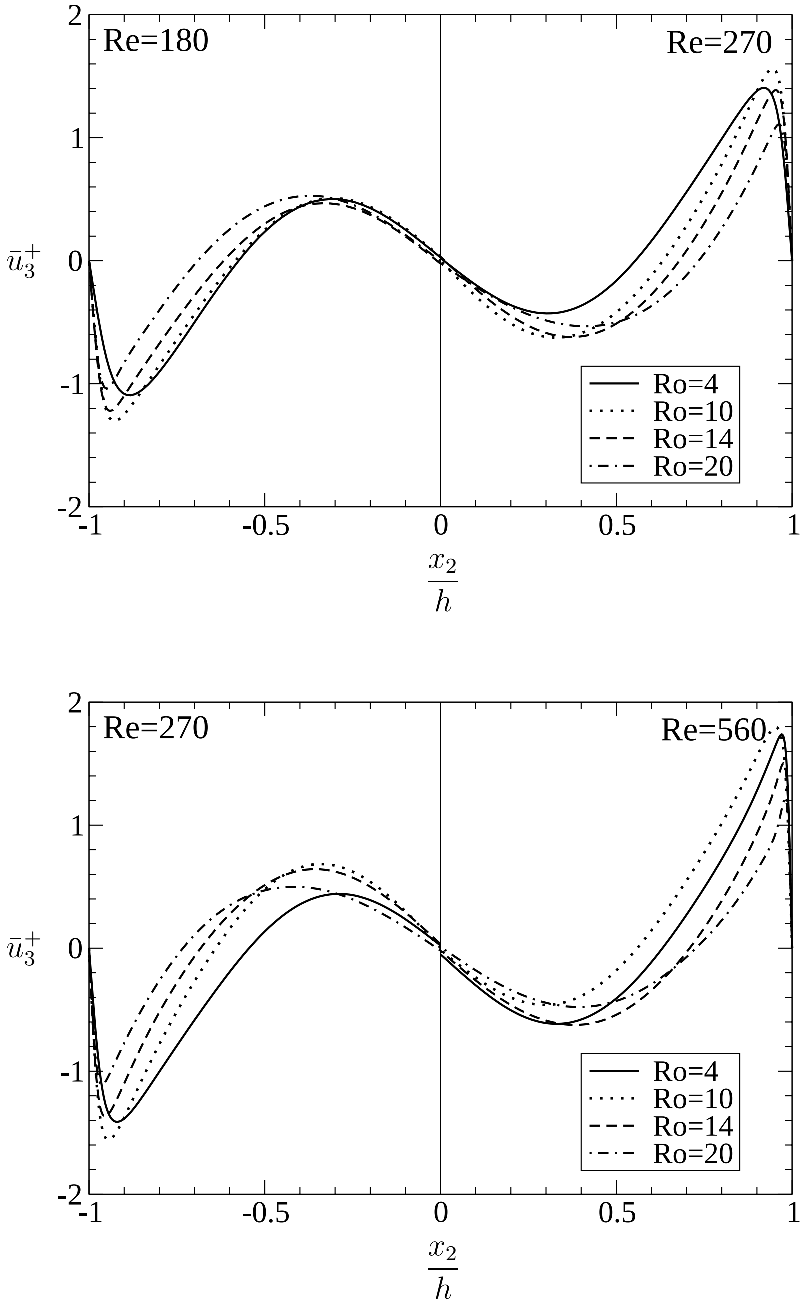

Figure 4.56: Spanwise mean velocity profiles $\bar{u}_3$ at different Reynolds numbers.

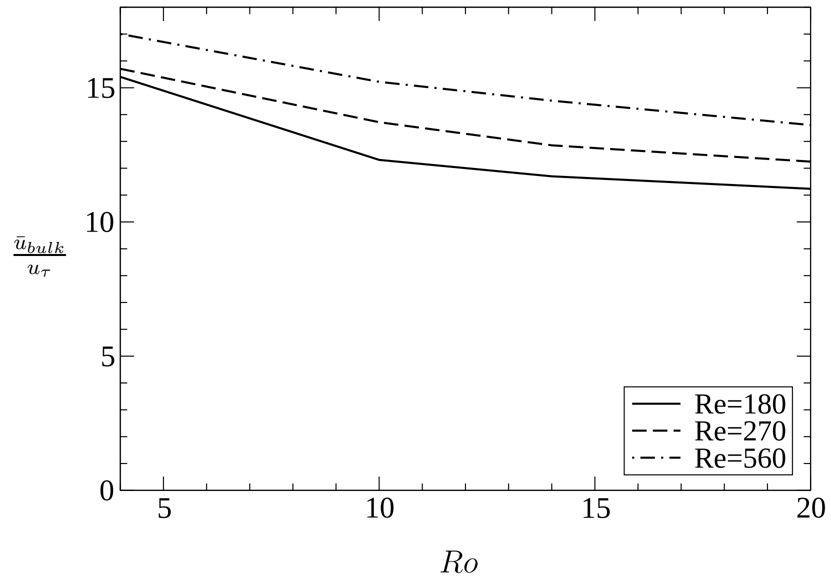

Figure 4.57: Development of $\bar{u}_{bulk}$ for increasing rotation rates at different Re_τ.

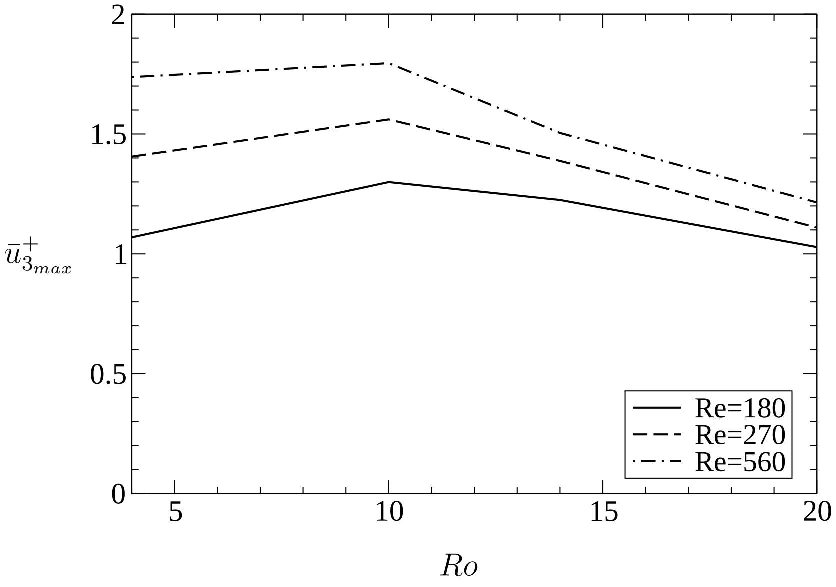

Figure 4.58: Development of $\bar{u}_{3_{max}}$ as a function of the rotation rate at different Re_τ.

The cross flow could be also verified in the DNS at higher Reynolds numbers (see Weller & Oberlack (2005b) and Weller & Oberlack (2006)). Figure 4.56 compares the spanwise mean velocity profiles at different Reynolds numbers.

The profiles show also an S-shaped skew-symmetric cross flow with a flow reversal in the core region of the channel with three zero-crossings. At higher Reynolds numbers the cross flow reaches a maximum value exactly at the same rotation rate $Ro = 10$ and then decreases for higher Ro.

Fig. 4.58 emphasises this effect, where the development of $\bar{u}_{3_{max}}$ as a function of the rotation rate is depicted. If you split the curves in two regions: first part from $Ro = 4$ to the maximum at $Ro = 10$ and second part from the maximum $Ro = 10$ to $Ro = 20$, it is important to notice, that the biggest gradient is in the first part at $Re_\tau = 180$ and in the second part for the highest Reynolds number $Re_\tau = 560$ visible.

As a results it is verified that the RDE is not only an effect at a rather low Reynolds number $Re_\tau = 180$. It is also visible for higher Reynolds numbers.

4.4.4.2 Reynolds Stress Tensor

In figures 4.59 - 4.64 the six components of the Reynolds stress tensor are compared at three different Reynolds numbers.

Generally the profiles have the same tendency as at $Re_\tau = 180$, only the maxima of the profiles are higher with increasing Reynolds numbers.

For higher Reynolds numbers the normal stress $\overline{u_1'u_1'}$ decreases at higher rotation rates. At $Re_\tau = 270$ $\overline{u_1'u_1'}$ exhibits a strong decay between $Ro = 4$ and 10, while at $Re_\tau = 560$ the different profiles are monotonically decreasing. The normal stresses $\overline{u_2'u_2'}$ and $\overline{u_3'u_3'}$ increase for higher rotation rates, whereas the shear stress $\overline{u_1'u_2'}$ stays nearly constant for all rotation rates.

The RDE is also noticeable at higher higher Reynolds numbers for the shear stresses $\overline{u_1'u_3'}$ and $\overline{u_2'u_3'}$.

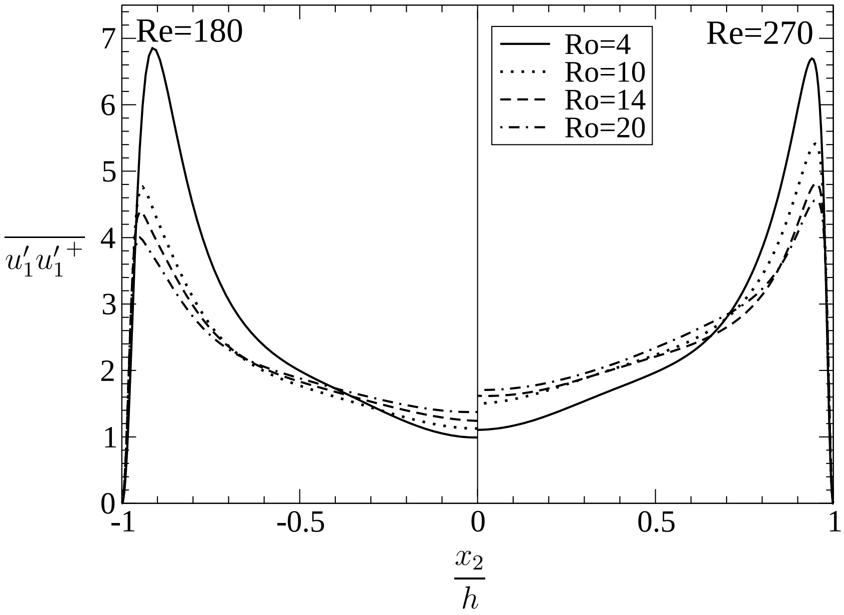

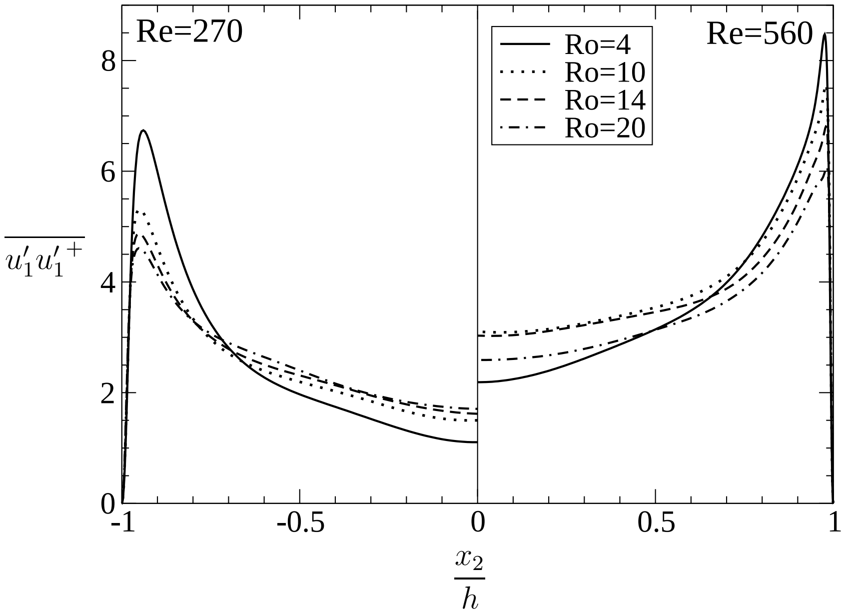

Figure 4.59: Comparison of Reynolds normal stresses $\overline{u_1' u_1'}$ at different Reynolds numbers.

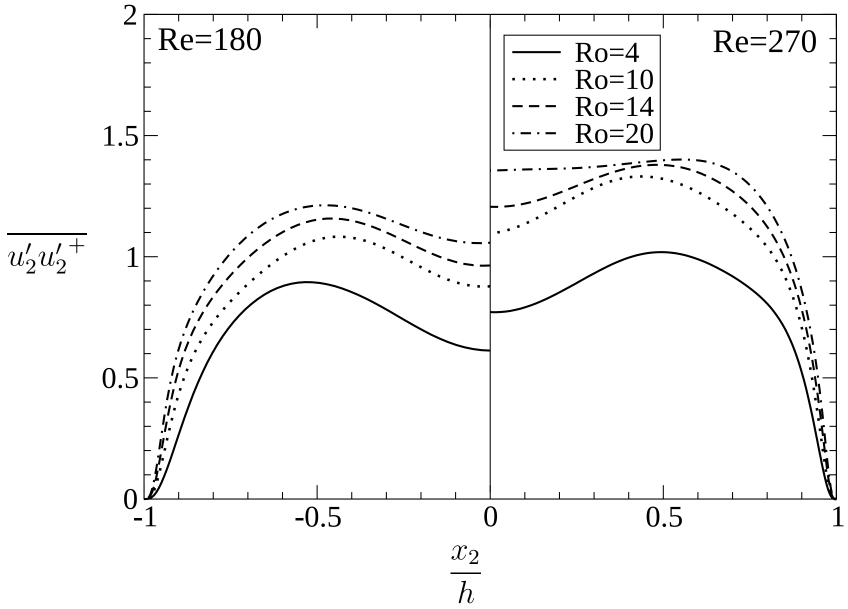

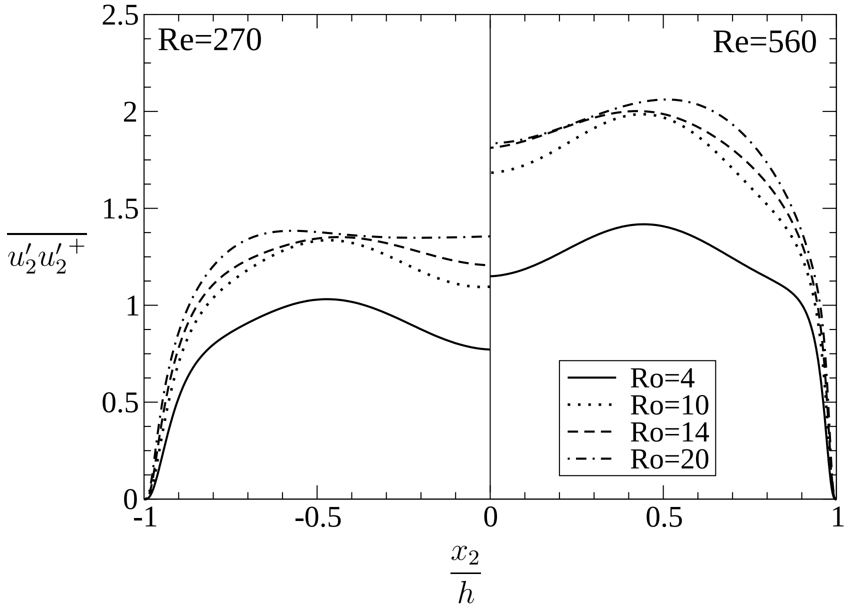

Figure 4.60: Comparison of Reynolds normal stresses $\overline{u_2'u_2'}$ at different Reynolds numbers.

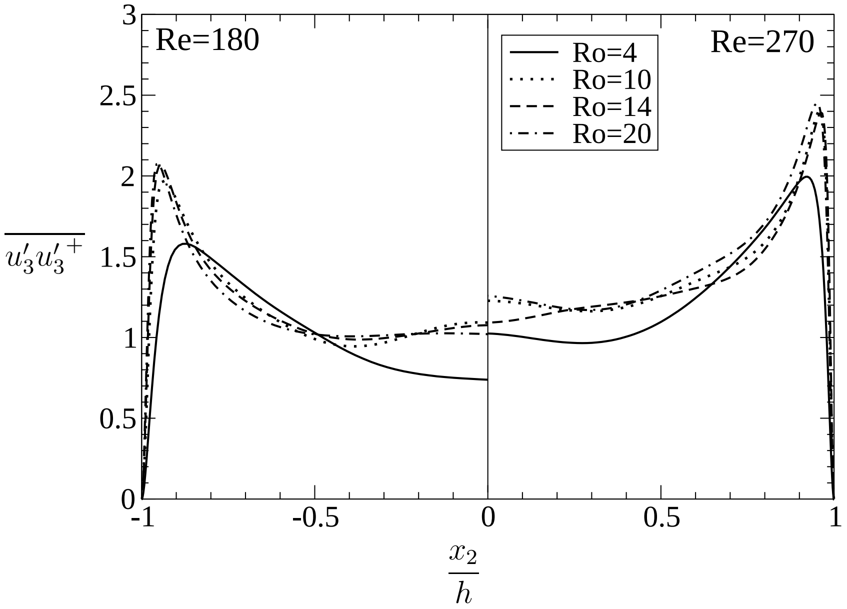

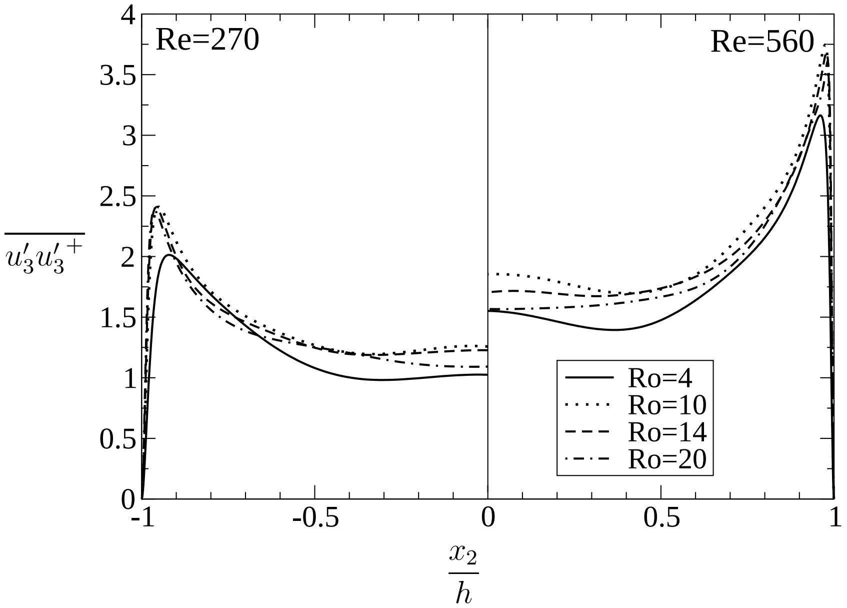

Figure 4.61: Reynolds normal stresses $\overline{u_3'u_3'}$ at different Reynolds numbers.

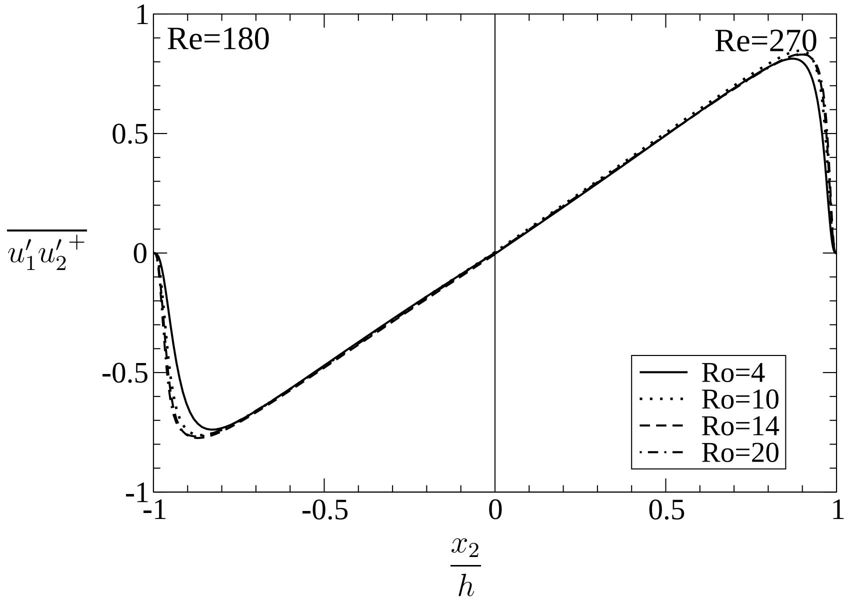

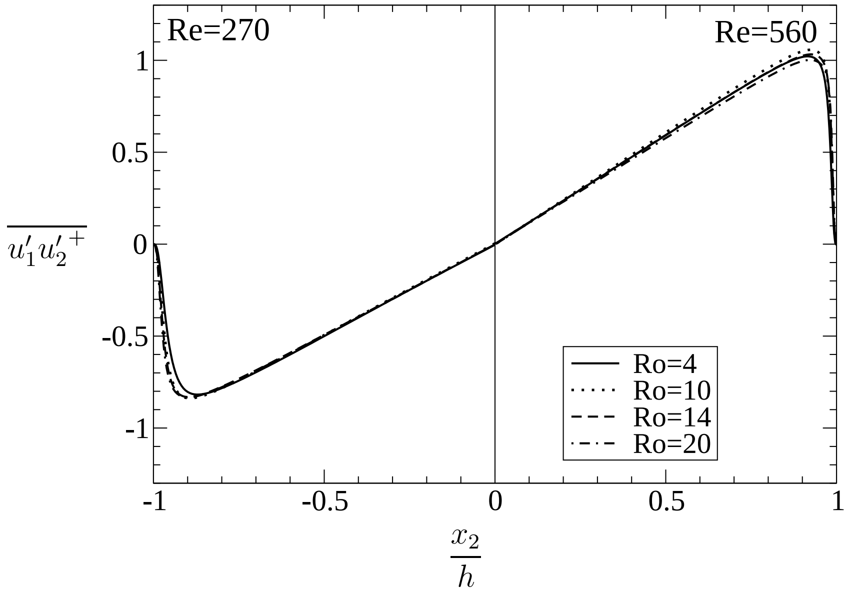

Figure 4.62: Reynolds shear stresses $\overline{u_1'u_2'}$ at different Reynolds numbers.

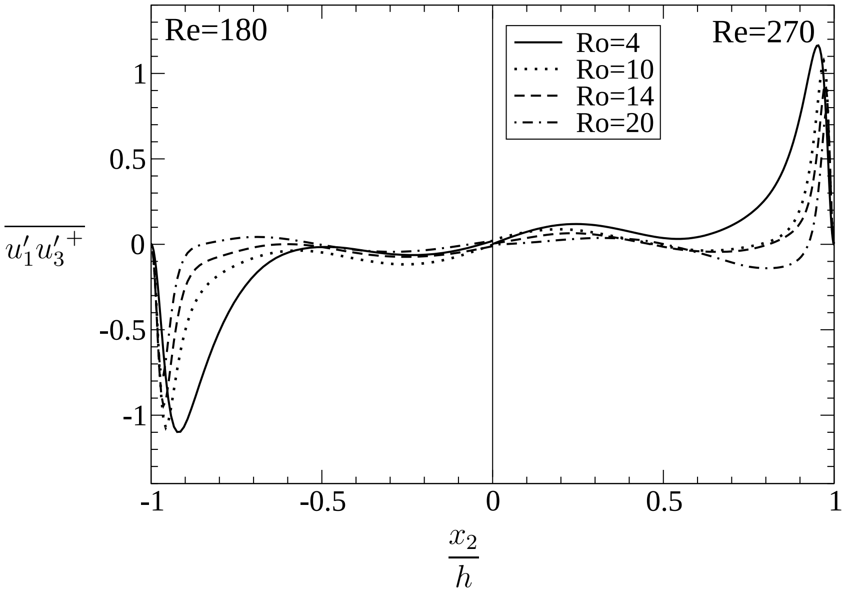

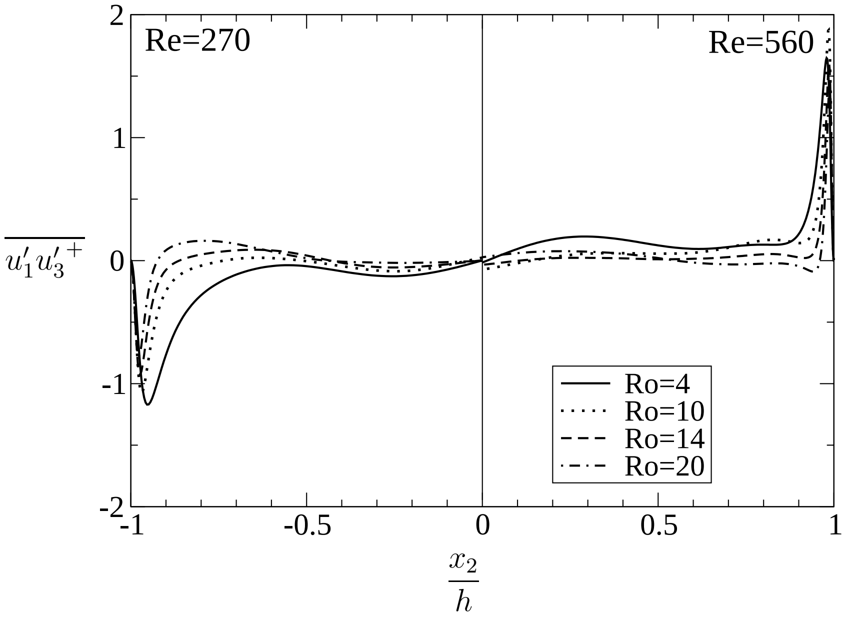

Figure 4.63: Reynolds shear stresses $\overline{u_1'u_3'}$ at different Reynolds numbers.

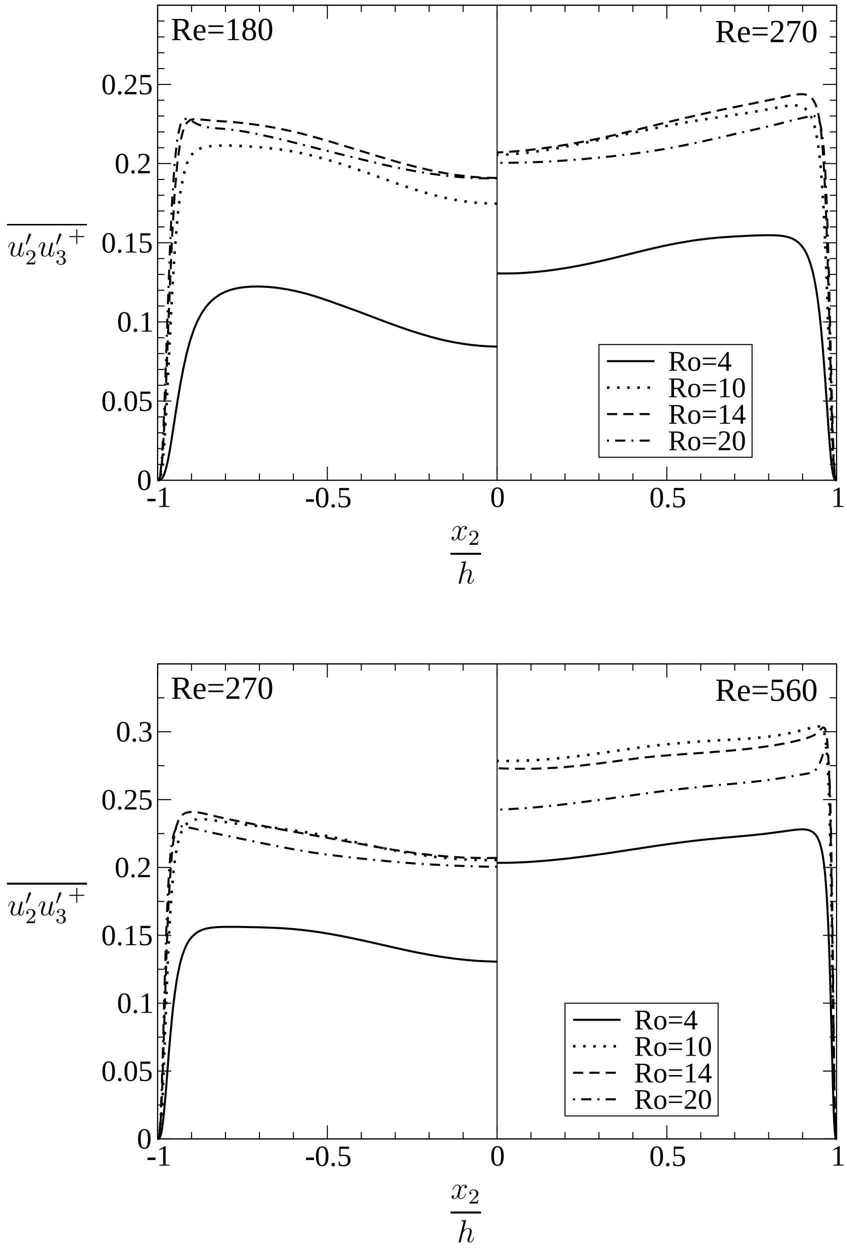

Figure 4.64: Reynolds shear stresses $\overline{u_2'u_3'}$ at different Reynolds numbers.

4.4.4.3 Isosurfaces of the Velocity Fields

In figures 4.65 - 4.66 the isosurfaces of the fluctuations of the wall-normal velocity field are presented at the instantaneous time unit $t \simeq 12000\frac{h/2}{u_{cl}}$ for two different Reynolds numbers $Re_\tau = 270$ and $Re_\tau = 560$ and four rotation rates up to $Ro = 20$. To compare the figures, the same value $u_2' = 0.018$ for the visualizations of the isosurfaces was selected, which is normalized on the centerline velocity u_{cl}.

In this subsection it was also renounced to normalize u_2' on the friction velocity u_τ, because u_τ depends directly on the Reynolds number and at this point the intension is to compare the results at different Reynolds numbers. For more details see sec. 4.3.4.5.

At $Re_\tau = 270$ and 560 u_2' is approximately located in the interval from -0.0362 to 0.0557. Table 4.7 gives a more precise overview about the minimum and maximum values of u_2' at different rotation rates. In general a value of $u_2' = 0.018$ represents rather a smaller scale of the spectrum.

Table 4.7: Minimum and maximum values of u_2' at $Re_\tau = 270$ and 560.

	$Re_\tau = 270$		$Re_\tau = 560$	
Ro	$u'_{2_{min}}$	$u'_{2_{max}}$	$u'_{2_{min}}$	$u'_{2_{max}}$
4	-0.0461	0.0479	-0.0372	0.0324
10	-0.0586	0.0545	-0.0366	0.0374
14	-0.0551	0.0540	-0.0380	0.0383
20	-0.0578	0.0557	-0.0362	0.0355

At higher Reynolds numbers it seems that the structures follow the same scheme as it was discussed in sec. 4.3.4.5 at $Re_\tau = 180$. For both Reynolds numbers the structures of the velocity fields at $Ro = 4$ are very disordered and distributed in the whole channel. From $Ro = 10$ up to $Ro = 20$ many large turbulent structures are formed, which are growing with an increasing rotation rate. It is remarkable that the structures at $Re_\tau = 560$ grow more slowly with increasing rotation rate than at $Re_\tau = 270$.

Furthermore, in figure 4.67 subdomains of the same size are presented at three Reynolds numbers and respectively different rotation rates. Primarily the subdomains give the possibility to compare the size and number of the structures directly, which is not given in figures 4.65 - 4.66 because of the different box lenghts. The other advantage is to have a better zoom of the velocity structures. Each subzone has a size of $4\pi \times 2 \times 1\pi$.

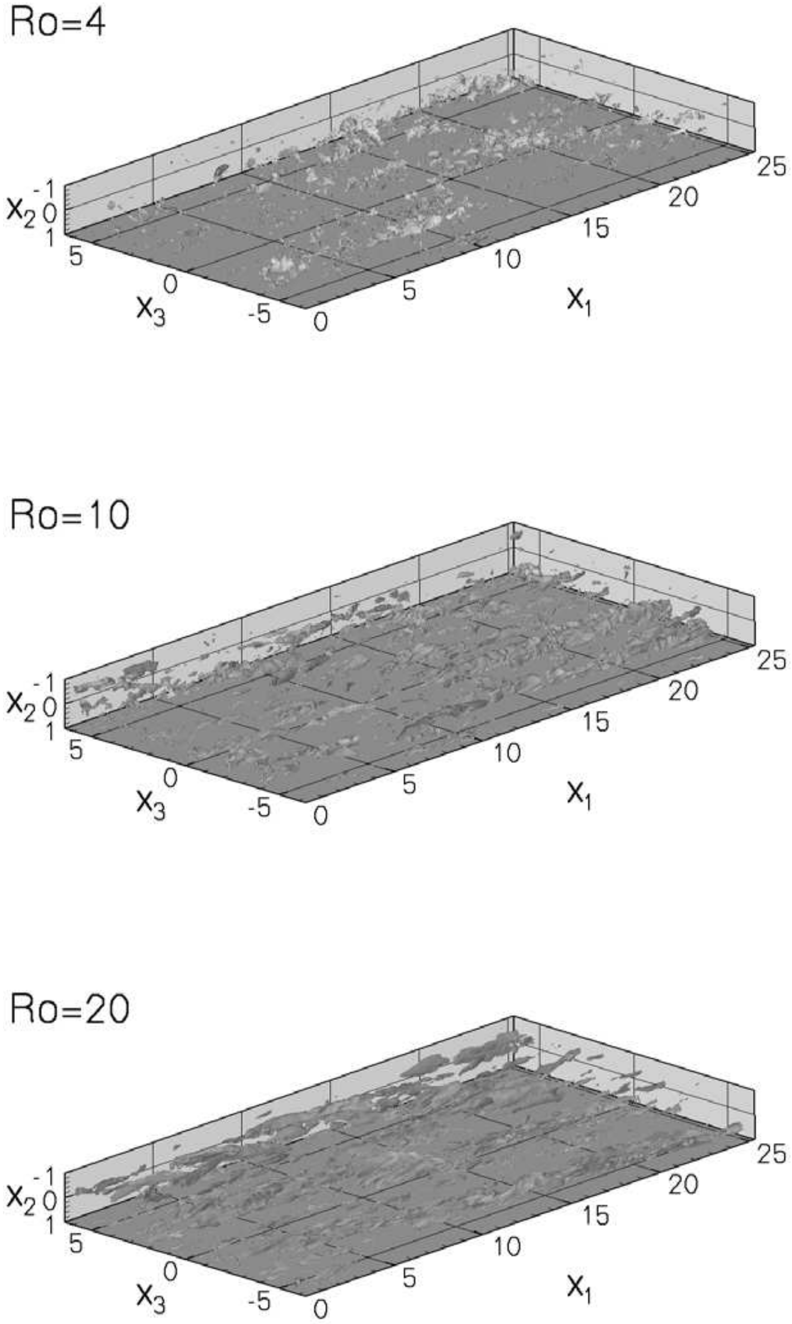

Figure 4.65: Isosurfaces of the wall-normal velocity field at $u_2' = 0.018$, $Re_\tau = 270$ and different rotation rates.

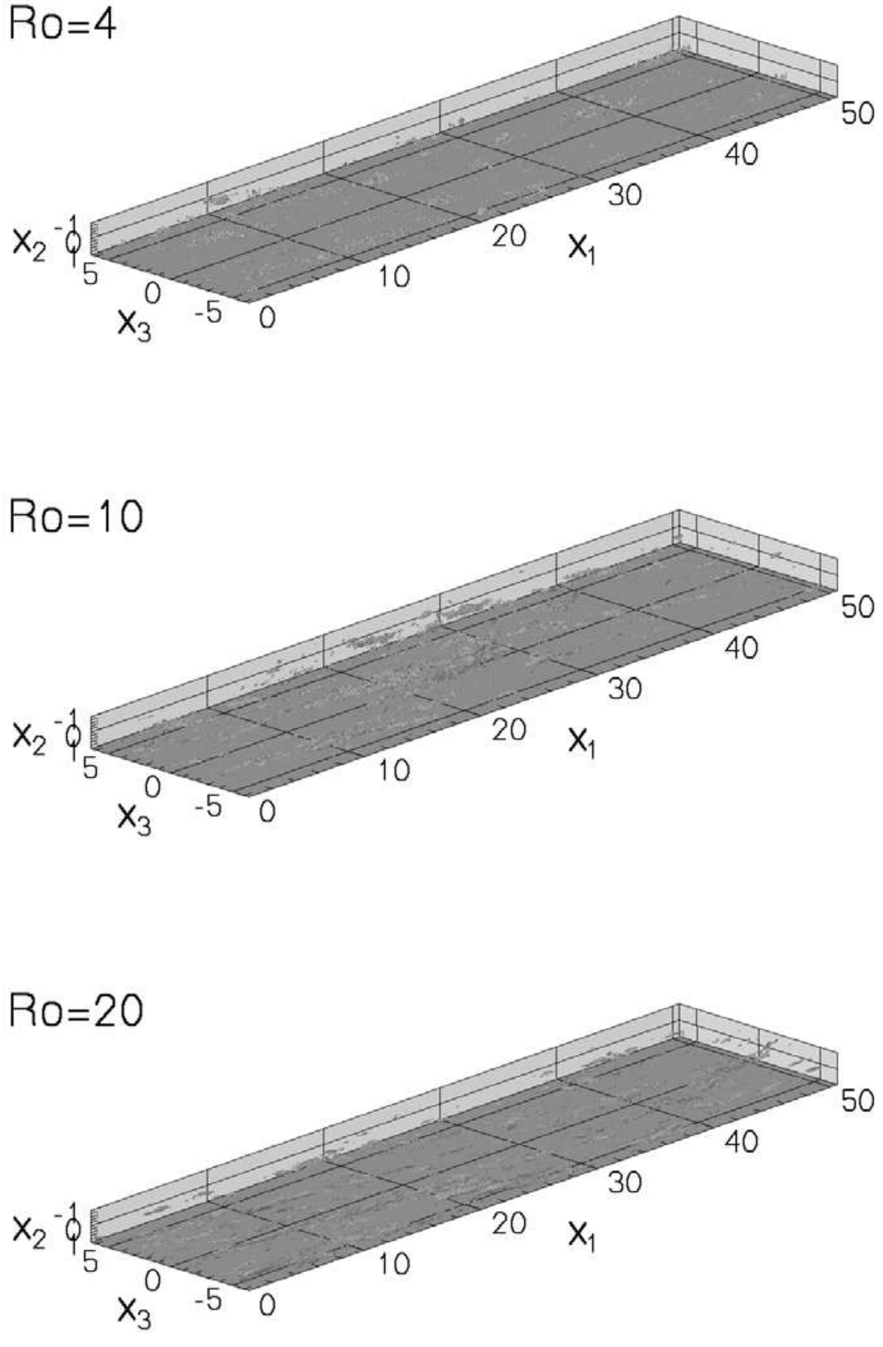

Figure 4.66: Isosurfaces of the wall-normal velocity field at $u_2' = 0.018$, $Re_\tau = 560$ and different rotation rates.

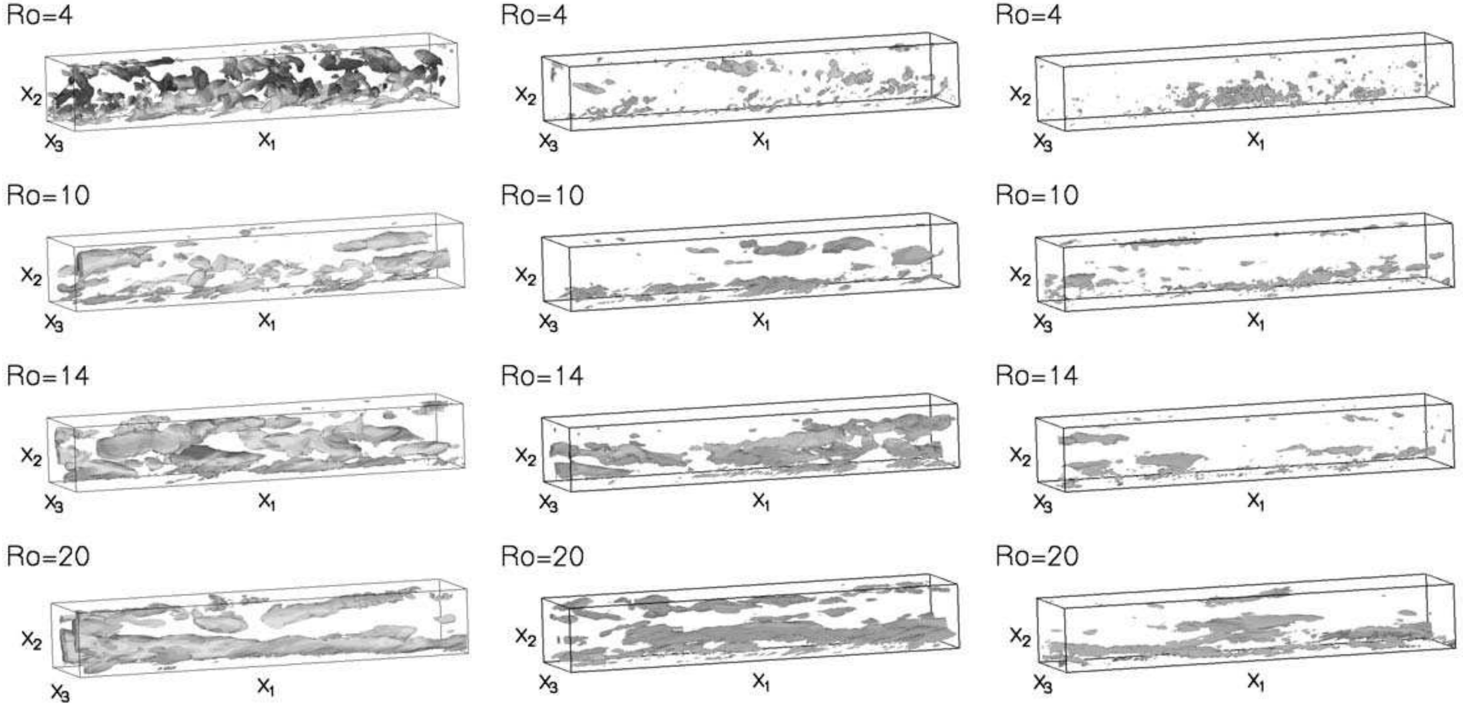

Figure 4.67: Subzones of isosurfaces of the wall-normal velocity fields at $u_2' = 0.018$ for different Ro: on the left hand side at $Re_\tau = 180$, in the middle at $Re_\tau = 270$ and at the right hand side at $Re_\tau = 560$.

The illustration emphasizes that the establishment of elongated structures starts for higher Reynolds numbers at higher rotation speeds.

While the structures at $Re_\tau = 560$ are disordered up to $Ro = 10$, the structures at $Re_\tau = 270$ start to grow from $Ro = 10$ on. The first larger structures at $Re_\tau = 560$ are observed at $Ro = 14$. At $Ro = 20$ in all cases elongated structures are visible. In general the radius of the structures are in all subdomains at higher Reynolds numbers smaller compared to the illustrations at $Re_\tau = 180$.

Summarized it is to say, that the growing of the structures strongly depends on both the rotation rate and the Reynolds number.

4.4.4.4 Isosurfaces of the Vorticity Fields

In figures 4.68 - 4.69 the isosurfaces of the fluctuations of the streamwise vorticity field are displayed at the instantaneous time unit $t \simeq 12000\frac{h/2}{u_{cl}}$ for both Reynolds numbers $Re_\tau = 270$ and $Re_\tau = 560$ and four different rotation rates up to $Ro = 20$. For all figures the same value $\omega_1' = \pm 2$ for the visualizations of the isosurfaces is used, which is normalized on the centerline velocity u_{cl}.

Analogously to sec. 4.3.4.5 it was also renounced to normalize ω_1' on the friction velocity u_τ. At $Re_\tau = 270$ and 560 ω_1' is approximately located in the interval from -7.0287 to 10.5057. Table 4.8 gives a more precise overview about the minimum and maximum values of ω_1' at different rotation rates. In general a value of $\omega_1' = \pm 2$ represents rather a smaller scale of the spectrum.

Table 4.8: Minimum and maximum values of ω_1' at $Re_\tau = 270$ and 560.

Ro	$Re_\tau = 270$		$Re_\tau = 560$	
	$\omega'_{1_{min}}$	$\omega'_{1_{max}}$	$\omega'_{1_{min}}$	$\omega'_{1_{max}}$
4	-8.2892	8.8572	-8.4569	9.1470
10	-7.0287	8.2853	-9.4491	10.5057
14	-9.1697	7.6311	-10.0345	9.6013
20	-9.8064	9.0623	-12.2102	10.4886

The illustrations, at $Re_\tau = 270$ and $Re_\tau = 560$ show respectively very similar vorticity structures for each rotation rate. The vorticies look very dense and are located in the wall region. More details can be obtained by analysing subdomains of the same size. Therefore, subzones of the same size, respectively $4\pi \times 2 \times 1\pi$, were extracted for all simulations.

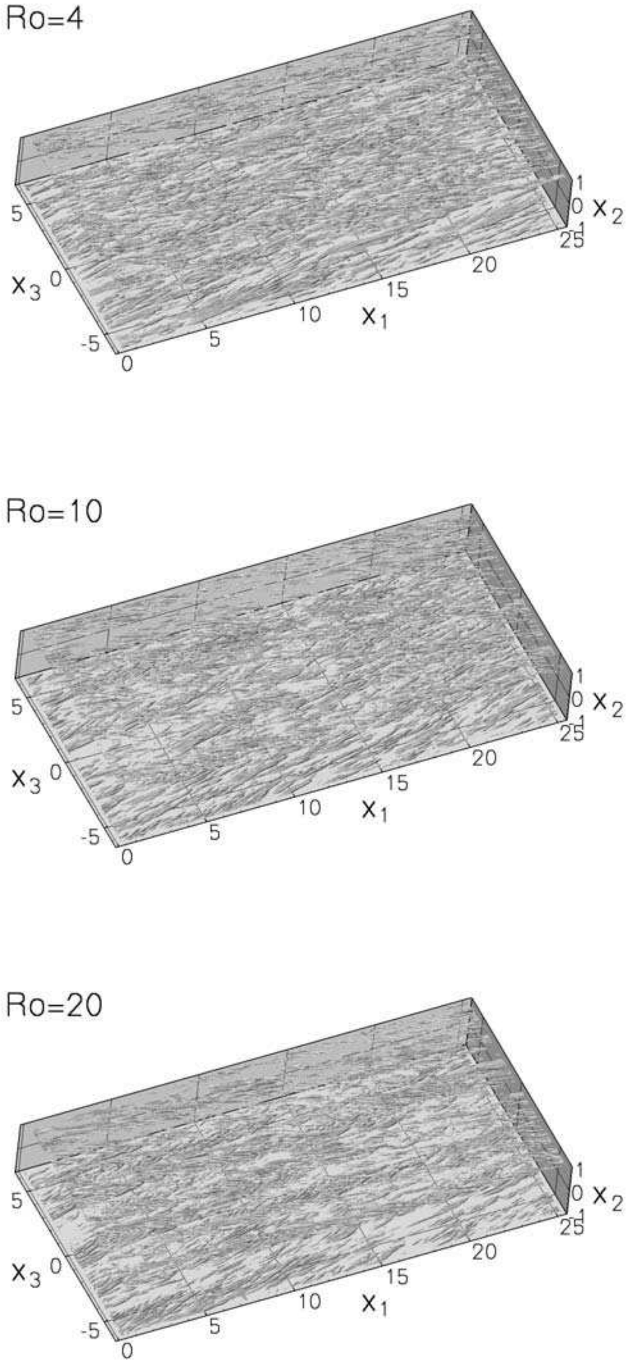

Figure 4.68: Isosurfaces of the streamwise vorticity field at $\omega_1' = \pm 2$, $Re_\tau = 270$ and different rotation rates.

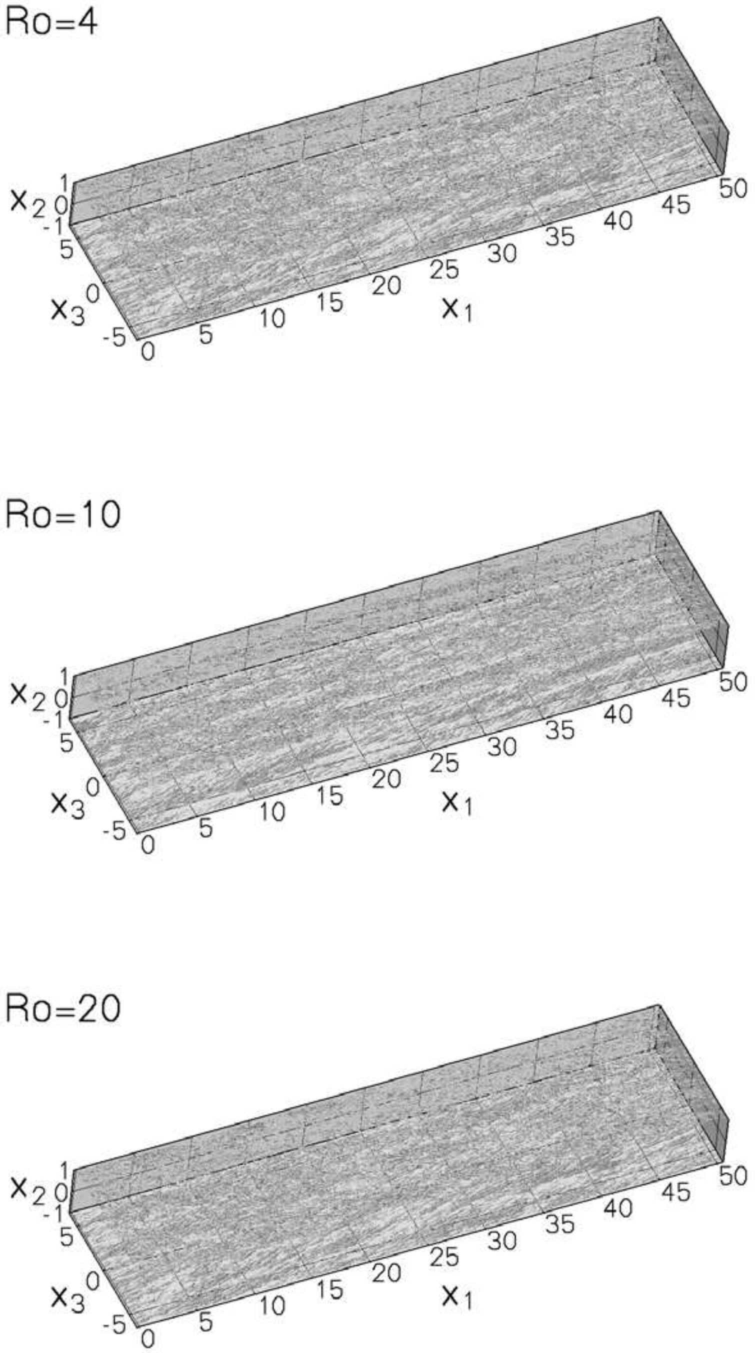

Figure 4.69: Isosurfaces of the streamwise vorticity field at $\omega_1' = \pm 2$, $Re_\tau = 560$ and different rotation rates.

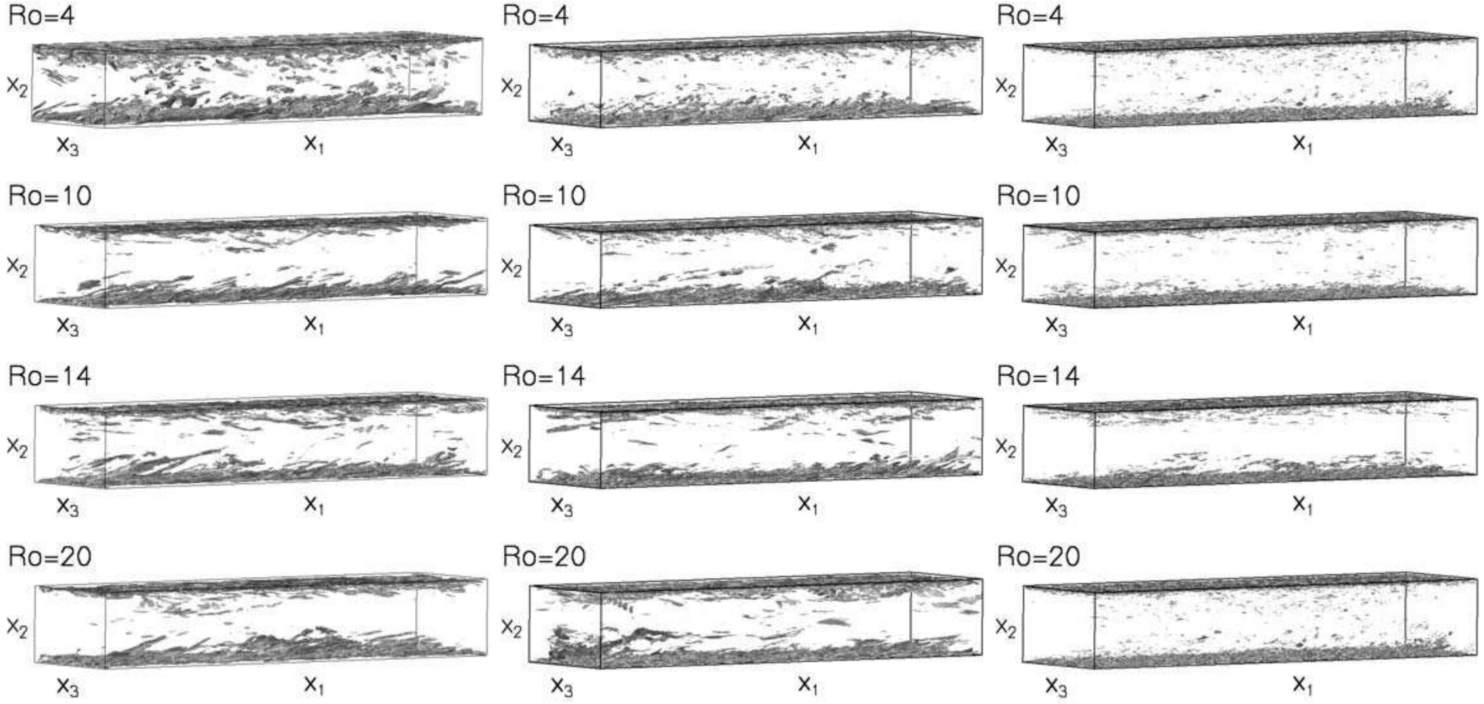

Figure 4.70: Subzones of isosurfaces of the wall-normal velocity fields at $\omega_1' = \pm 2$ for different Ro: on the left hand side at $Re_\tau = 180$, in the middle at $Re_\tau = 270$ and at the right hand side at $Re_\tau = 560$.

In fig. 4.70 the subdomains are compared at three Reynolds numbers. The different subzones at $Re_\tau = 270$ look very similar to the ones at $Re_\tau = 180$, which means they are growing with an increasing rotation rate. The structures at $Re_\tau = 560$ are for all rotation rates smaller and thinner, no larger structures can be recognized due to the rotation. In all figures the vorticies are more dense in the wall region.

5 Wavelet Analysis

5.1 Historical Background

Wavelets are mathematical functions, which divide data into different frequency components to study each component with a resolution matched to its scale. They have advantages over traditional Fourier methods in analyzing physical situations, where the signal contains discontinuities and sharp spikes. Wavelets were developed independently in the fields of mathematics, quantum physics, electrical engineering and seismic geology.
In the last twenty years wavelets become more and more popular for many new wavelet applications such as image compression, speech discrimination, music, turbulence, human vision, radar and earthquake prediction. (see Graps (1995)).

From an historical point of view, the roots of wavelets go back to the work of Joseph Fourier, a French mathematician. Fourier claimed in 1807 that any 2π-periodic function $f(x)$ is the sum:

$$f(x) \;=\; a_0 + \sum_{k=1}^{\infty} \left(a_k \cos\left(kx\right) + b_k \sin\left(kx\right)\right) \tag{5.1}$$

of its Fourier series. The coefficients a_0, a_k, and b_k are calculated by

$$a_0 = \frac{1}{2\pi}\int_0^{2\pi} f(x)dx \qquad a_k = \frac{1}{\pi}\int_0^{2\pi} f(x)\cos(kx)dx \qquad b_k = \frac{1}{\pi}\int_0^{2\pi} f(x)\sin(kx)dx$$

Fourier's assertion played an essential role in the evolution of the ideas mathematicians had about functions. Mathematicians extended the theory to non-periodic functions that change over time, rather than repeating in the same shape, the so-called Fourier-Transform.

Hence, a useful tool known as Fourier analysis was born that allows complex periodic and non-periodic functions to be summed as a series of simpler functions. At this time scientists solved with this theory many problems in physics and engineering.

At the same time tey observed some short coming e.g. they had trouble reproducing transient signals or signals with abrupt changes, such as the spoken word. Although the scientists started to solve the problems particular to their fields, they began to arrive at essentially the same solution - namely, that Fourier transforms themselves are to blame.
Over the course of the twentieth century, scientists worked to get around these limitations and arrived at the same solution. It is necessary to split a signal up into components that could be localized in time and analyzed at different scales of resolution. This is the idea of wavelet theory.

The first mention of wavelets appeared in an appendix to the thesis of Alfred Haar, a Hungarian mathematician, in 1909. He introduced the *Haar* wavelets (fig. 5.1a). These functions consist simply of a short positive pulse followed by a short negative pulse:

$$\begin{aligned} \psi(x) &= 1 \qquad \text{if} \qquad x \in [0, 0.5[\\ \psi(x) &= -1 \qquad \text{if} \qquad x \in [0.5, 1[\\ \psi(x) &= 0 \qquad \text{if} \qquad x \notin [0, 1[. \end{aligned} \tag{5.2}$$

They are less useful for most applications because they yield jagged lines instead of smooth curves.
In 1930, John Littlewood and R. Paley, both English mathematicians, showed that local information about a signal can be retrieved by grouping the terms of its Fourier series into octaves. Sixteen years later, Dennis Gábor, a British-Hungarian physicist who invented holography, introduced the *Gábor* transform which splits a signal into time-frequency packets which have localization in both time and frequency. In 1976, IBM physicists Claude Galand and Daniel Esteban discovered subband coding, a way of encoding digital transmissions for the telephone. In 1981, Jean Morlet, a Petroleum engineer for Elf-Aquitaine, developed his own way of analyzing the seismic signals to create components that were localized in space. His wavelets are now known as *Morlet* wavelets (fig. 5.1b):

$$\psi = ce^{-x^2/2} cos(5x), \tag{5.3}$$

where the constant c is used for normalization in view of recontruction.
Morlet turns Alex Grossmann, a quantum physicist at the Centre de Physique Théorique in Marseilles, for help in proving that the method works. Grossmann worked with Morlet for a year to confirm that waves could be reconstructed from their wavelet decompositions (Grossmann & Morlet 1984). In 1984, Morlet and

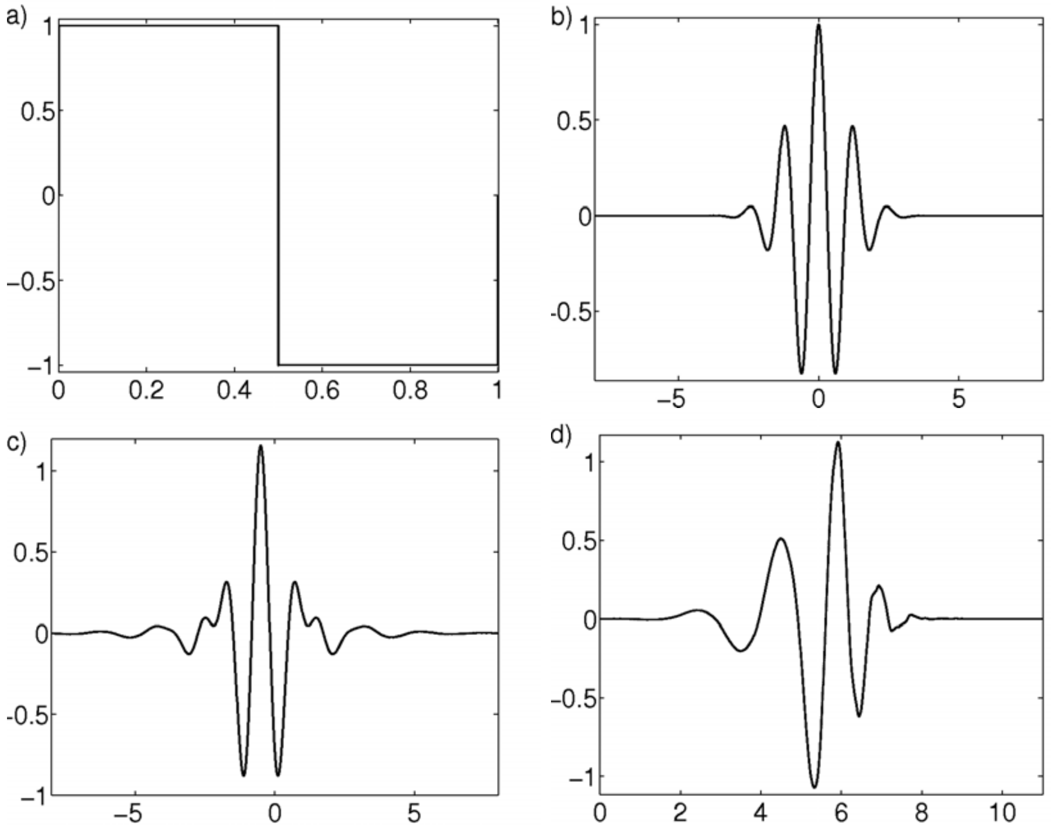

Figure 5.1: Different wavelets ψ in physical space: a) Haar, b) Morlet, c) Meyer and d) Daubeschies.

Grossmann brought the word *wavelet* into the mathematical lexicon for the first time.
Only one year later, Yves Meyer of the University of Paris discovered the first smooth orthogonal wavelets (fig. 5.1c). The Meyer wavelet function is defined in the frequency domain:

$$\begin{aligned}
\hat{\psi}(\omega) &= (2\pi)^{-1/2} e^{i\omega/2} sin\Big(\frac{\pi}{2}\nu\big(\frac{3}{2\pi}|\omega| - 1\big)\Big) \qquad \text{if} \qquad \frac{2\pi}{3} \le |\omega| \le \frac{4\pi}{3} \\
\hat{\psi}(\omega) &= (2\pi)^{-1/2} e^{i\omega/2} cos\Big(\frac{\pi}{2}\nu\big(\frac{3}{4\pi}|\omega| - 1\big)\Big) \qquad \text{if} \qquad \frac{4\pi}{3} \le |\omega| \le \frac{8\pi}{3} \\
\hat{\psi}(\omega) &= 0 \qquad \text{if} \qquad |\omega| \notin \Big[\frac{2\pi}{3}, \frac{8\pi}{3}\Big],
\end{aligned} \tag{5.4}$$

with $\nu(a) = a^4(35 - 84a + 70a^2 - 20a^3)$ and $a \in [0, 1]$. Orthogonality means that the information captured by one wavelet is completely independent of the information captured by another.

In 1986, Stéphane Mallat, at the University of Pennsylvania, a former student of Meyer, showed that the Haar basis, the Littlewood-Paley octaves, the Gábor time-frequency packets, and the subband filters of Galand and Esteban are all related to wavelet-based algorithms.

In 1987, Ingrid Daubechies, a physicist and presently director of the department of mathematics at Princeton University, constructed the first smooth orthogonal wavelets(Daubechies 1992). The square modulus of the transfer function of h is explicit and fairly simple. Let

$$P(y) = \sum_{k=0}^{N-1} C_k^{N-1+k} y^k, \tag{5.5}$$

where C_k^{N-1+k} denotes the binomial coefficients. Then

$$|m_0(\omega)|^2 = \Big(cos^2(\frac{\omega}{2})\Big)^N P\Big(sin^2(\frac{\omega}{2})\Big) \quad \text{with} \quad m_0(\omega) = \frac{1}{\sqrt{2}} \sum_{k=0}^{2N-1} h_k e^{-ik\omega}. \tag{5.6}$$

The support length of ψ is 2N-1. Her wavelets (fig. 5.1d) turned the theory into a practical tool that can be easily programmed and used by any scientist with a minimum of mathematical training.

With the foundations of wavelet, the field has grown rapidly over the last years. Many researchers are interested in expanding the application of wavelets beyond image compression to other areas.

5.2 Basics in Wavelets

The main idea of wavelets is to decompose a signal f into a basis of functions ψ_i (Daubechies 1992):

$$f = \sum_i a_i \psi_i \tag{5.7}$$

to have an efficient representation of a signal f using only a few coefficients a_i. For this reason it is very important to use a suitable family of functions ψ_i, which reproduce the signal very well.

Usually signals are limited both in time (or space i.e. in the case of images) and in frequency. Time-limited signals can be presented efficiently by a basis of block functions and frequency-limited signals by a Fourier basis (sines and cosines functions). The main problem is that block functions are not frequency-limited and a Fourier basis are not limited in time. A combination of both time-limited and frequency-limited functions is necessary, which is provided by wavelets

5.2.1 Properties of Wavelets

One of the main feature of wavelets is their good decorrelation. Wavelets can be characterized as (Mallat 1998):

- localized in both space/time and scale/frequency domains. Hence, they are able to detect easily local features of a signal.
- based on multi-resolution analysis, which means that a wavelet decomposition allows to analyze a signal at different resolution levels (scales).
- smooth, which can be characterized by their number of vanishing moments. A function defined on the interval $[a, b]$ has n vanishing moments if

  $$\int_a^b f(x)x^i dx = 0 \quad \text{for} \quad i_0, 1, .., n-1. \tag{5.8}$$

  The higher the number of vanishing moments, the better smooth signals can be approximated in a wavelet basis.

5.2.2 Multi-Resolution Analysis (MRA)

We consider the space $\boldsymbol{L}^2$, the vector space of square integrable functions in $\boldsymbol{R}$:

$$\boldsymbol{L}^2 = \left\{ f : \int_{-\infty}^{+\infty} f^2(x)dx < \infty \right\}. \tag{5.9}$$

In a multi-resolution analysis (Mallat 1989) we decompose $\boldsymbol{L}^2$ in nested subspaces V_j

$$\cdots \subset V_{-2} \subset V_{-1} \subset V_0 \subset V_1 \subset V_2 \subset \cdots \tag{5.10}$$

in a way that the closure of their union is $\boldsymbol{L}^2$

$$\overline{\bigcup_{j=-\infty}^{+\infty} V_j} = \boldsymbol{L}^2, \tag{5.11}$$

and their intersection contains only the zero-function

$$\bigcup_{j=-\infty}^{+\infty} V_j = \{0\}. \tag{5.12}$$

In the dyadic case, i.e. when each subspace V_j is twice as large as V_{j-1}, a function $f(x)$ that belongs to one of these subspaces V_j has the following properties:

$$\begin{aligned} f(x) \in V_j \quad &\Leftrightarrow \quad \text{dilation} \quad f(2x) \in V_{j+1} \\ f(x) \in V_0 \quad &\Leftrightarrow \quad \text{translation} \quad f(x+1) \in V_0 \end{aligned} \tag{5.13}$$

if we can find a function $\varphi(x) \in V_0$ such that the set of functions consisting of $\varphi(x)$ and its integer translates

$$\{\varphi(x-k)\}_{k\in\boldsymbol{Z}} \tag{5.14}$$

form a basis for the space V_0 , we call it a *scalling function* or *father function.* For the other subspaces $V_j($ with $j \neq 0)$ we define:

$$\varphi_{j,k}(x) \equiv 2^{j/2}\varphi\left(2^j x - k\right). \tag{5.15}$$

5.2.3 Wavelet Functions

Because the subspaces V_j are nested:

$$V_j \subset V_{j+1}, \tag{5.16}$$

we can decompose V_{j+1} in V_j and W_j, the orthogonal complement of V_j in V_{j+1} :

$$V_j \oplus W_j = V_{j+1}, \tag{5.17}$$

$$W_j \perp V_j. \tag{5.18}$$

The direct sum of the subspaces W_j is equal to $\boldsymbol{L}^2$:

$$\overline{\bigcup_{j=-\infty}^{+\infty} V_j} = \overline{\bigoplus_{j=-\infty}^{+\infty} W_j} = \boldsymbol{L}^2 \tag{5.19}$$

This means that V_j is a *coarse-resolution* representation of V_{j+1} , while W_j carries the *hight-resolution* difference information between V_{j+1} and V_j. If we can find a function $\psi(x) \in W_0$ that obeys the translation property (see sec. 5.2.1) i.e.

$$\psi(x) \in W_0 \Leftrightarrow translation \quad \psi(x+1) \in W_0, \tag{5.20}$$

and such that a set of function consisting of $\psi(x)$ and its integer translates

$$\{\psi(x-k)\}_{k\in z} \tag{5.21}$$

from a basis for the space W_0, we call it a *wavelet function* or *mother function.* For the other subspaces V_j(with $j \neq 0$) we define:

$$\psi_{j,k}(x) \equiv 2^{j/2}\psi\left(2^j x - k\right). \tag{5.22}$$

5.2.4 The Fast Wavelet Transform (FWT)

Because both V_0 and W_0 are subspaces of V_1:

$$V_0 \subset V_1 \text{and} W_0 \subset V_1, \tag{5.23}$$

we can express $\varphi(x)$ and $\psi(X)$ in term of basis functions of V_1:

$$\varphi(x) = 2\sum_k h_k \varphi(2x-k), \tag{5.24}$$

$$\psi(x) = 2\sum_k g_k \varphi(2x-k). \tag{5.25}$$

Due to the multi-resolution analysis, these relation are also valid between V_{j+1}, V_j and W_j for arbitrary j. We call the h_k and g_k the filter coefficients that uniquely define the scaling function $\varphi(x)$ and the wavelet $\psi(x)$.

Since $V_{j+1} = V_j \oplus W_j$, we can express a function $f(x)$ that is written in terms of the basis functions of V_{j+1} in terms of the basis functions of V_j and W_j also:

$$\begin{aligned} f(x) &= \sum_k \lambda_{j+1,k}\varphi_{j+1,k}(x), && (5.26)\\ &= \sum_l \lambda_{j,l}\varphi_{j,l}(x) + \sum_l \gamma_{j,l}\psi_{j,l}(x). && (5.27)\end{aligned}$$

with the transform coefficients $\lambda_{j,l}$ and $\gamma_{j,l}$ defined by:

$$\begin{aligned} \lambda_{j,l} &= \sqrt{2}\sum_k h_{k-2l}\lambda_{j+1,k}, && (5.28)\\ \gamma_{j,l} &= \sqrt{2}\sum_k g_{k-2l}\lambda_{j+1,k}. && (5.29)\end{aligned}$$

This operation is known as the *Fast Wavelet Transform* (FWT). It is called *fast* because its complexity is $O(n)$, i.e. the amount of work is proportional to the signal length. The filter h_k is a low-pass filter, while g_k is a high-pass filter.

5.2.5 Orthogonal Wavelets

If the $\varphi_{j,k}(x)$ and $\psi_{j,k}(x)$ are orthonormal:

$$\begin{aligned} V_j &\perp W_j, && (5.30)\\ \langle \varphi_{j,l}, \varphi_{j,l'}\rangle &= \delta_{l-l'}, && (5.31)\\ \langle \psi_{j,l}, \psi_{j',l'}\rangle &= \delta_{j-j'}\delta_{l-l'}, && (5.32)\end{aligned}$$

then we can calculate the coefficients of the decomposition

$$f(x) = \sum_l \lambda_{j,l}\varphi_{j,l}(x) + \sum_l \gamma_{j,l}\psi_{j,l}(x) \qquad (5.33)$$

by taking inner products with the scaling and wavelet functions:

$$\lambda_{j,l} = \langle f, \varphi_{j,l} \rangle , \tag{5.34}$$

$$\gamma_{j,l} = \langle f, \psi_{j,l} \rangle . \tag{5.35}$$

The decomposition in the wavelet basis is guaranteed to be stable: if the function $f(x)$ is slightly changed, this will cause only a slight change in the coefficients $\lambda_{j,l}$ and $\gamma_{j,l}$. Parseval's identity holds:

$$\|f\|^2 = \sum_k \lambda^2_{j+1,k}, \tag{5.36}$$

$$= \sum_l \lambda^2_{j,l} + \sum_l \gamma^2_{j,l} \tag{5.37}$$

Examples of orthogonal wavelets are the family of orthogonal wavelets constructed by Daubechies (1988). The wavelet function $\psi(x)$ for the member with 4 vanishing moments (also known as *D8* because the corresponding wavelet filter has 4 taps or filter coefficients) is shown in fig. 5.1d.

5.3 Some prominent Applications

In 1993, the FBI chooses a wavelet method developed by Tom Hopper of the FBI's Criminal Justice Information Services Division and Jonathan Bradley and Chris Brislawn from Los Alamos National Laboratory to compress its enormous database of fingerprints (Bradley, Brislawn & Hopper 1993). The method allows to zoom in on an image without losing resolution.

In 1998, Walt Disney Pictures and Pixar Animation Studios released a full-length computer-animated feature film called *A Bug's Life* (Mackenzie 2001). A challenge was to develop all of these numerous characters of the animated ants, their many textures, their myriad expressions, and the way they jumped, flitted, and buzzed around. Only the use of wavelets made these enormous calculations of all the computer animations possible.

In 1999, the International Standards Organization approves a new standard for digital picture compression, called JPEG-2000 (Mackenzie 2001). The new standard uses wavelets to compress image files by 1:200 ratios with no visible loss in image quality. Since 2001, web browsers support the new standard.

5.4 Application to Turbulence

The first application to turbulence was manufactured in 1999 by Farge (1992), a French physicist. During the following years Marie Farge and Kai Schneider developed in France a new method, known as *Coherent Vortex Extraction* (CVE) method, to extract coherent vortices from two- and three-dimensional homogeneous turbulent flows (Farge, Schneider & Kevlahan 1999, Farge, Pellegrino & Schneider 2000, Farge, Pellegrino & Schneider 2001a). A short introduction into the CVE method is presented in sec. 5.5.
Until today the method was applied to many areas in turbulence. For example in 2001 to study turbulent transport in confined hot plasmas (Farge, Schneider & Devynck 2001b), in 2002 to 3D homogeneous isotropic turbulence (Farge, Schneider, Pellegrino, Wray & Rogallo 2002), in 2003 to mixing layer (Schneider & Farge 2003, Schneider, Pellegrino, Farge & Rogers 2003, Schneider, Farge, Pellegrino & Rogers 2005) as well as to study the mixing of passive and reactive scalars in 2D turbulent flows (Beta, Schneider, Farge & Bockhorn 2003).
The applications have shown, that the method is well suited to extract coherent structures, not only for their 3D visualization. It represents also the basis for their further investigations.

M. Farge and K. Schneider were so kind to make her wavelet package, based on the CVE method, avaiable for us. In colloboration we started to study vortices and their statitics of our rotating channel flow. A short introduction into the CVE method is given in the next section and the results are presented in sec. 5.7.

5.5 Coherent Vortex Extraction (CVE) Method

An orthogonal wavelet-based method to extract coherent vortices from 3D turbulent flow was proposed by M. Farge and K. Schneider. More details on the method can be obtained from Farge et al. (2001a). Further a short introduction into the method will be given.

Considered is the vorticity field $\boldsymbol{\omega} = \nabla \times \boldsymbol{u}$ at resolution $N = 2^{3J}$, where N is the number of grid points and J the corresponding number of octaves. Each component is developed into an orthogonal wavelet series, from the largest scale $l_{max} = 2^0$ to the smallest scale $l_{min} = 2^{1-J}$, using as 3D multi-resolution analysis (MRA) (Daubechies 1992, Farge 1992):

$$\boldsymbol{\omega}\left(\boldsymbol{x}\right) \; = \; \tilde{\boldsymbol{\omega}}_{0,0,0,0}\phi_{0,0,0,0}\left(\boldsymbol{x}\right) \; + \; \sum_{j=0}^{J-1}\sum_{i_{x_1}=0}^{2^j-1}\sum_{i_{x_2}=0}^{2^j-1}\sum_{i_{x_3}=0}^{2^j-1}\sum_{\mu=1}^{7}\tilde{\boldsymbol{\omega}}^{\mu}_{j,i_{x_1},i_{x_2},i_{x_3}}\psi^{\mu}_{j,i_{x_1},i_{x_2},i_{x_3}}\left(\boldsymbol{x}\right), \tag{5.38}$$

with

$$\psi^{\mu}_{j,i_{x_1},i_{x_2},i_{x_3}}\left(\boldsymbol{x}\right) \; = \; \begin{cases} \psi_{j,i_{x_1}}\left(x_1\right)\phi_{j,i_{x_2}}\left(x_2\right)\phi_{j,i_{x_3}}\left(x_3\right), & \mu = 1, \\ \phi_{j,i_{x_1}}\left(x_1\right)\psi_{j,i_{x_2}}\left(x_2\right)\phi_{j,i_{x_3}}\left(x_3\right), & \mu = 2, \\ \phi_{j,i_{x_1}}\left(x_1\right)\phi_{j,i_{x_2}}\left(x_2\right)\psi_{j,i_{x_3}}\left(x_3\right), & \mu = 3, \\ \psi_{j,i_{x_1}}\left(x_1\right)\phi_{j,i_{x_2}}\left(x_2\right)\psi_{j,i_{x_3}}\left(x_3\right), & \mu = 4, \\ \psi_{j,i_{x_1}}\left(x_1\right)\psi_{j,i_{x_2}}\left(x_2\right)\phi_{j,i_{x_3}}\left(x_3\right), & \mu = 5, \\ \phi_{j,i_{x_1}}\left(x_1\right)\psi_{j,i_{x_2}}\left(x_2\right)\psi_{j,i_{x_3}}\left(x_3\right), & \mu = 6, \\ \psi_{j,i_{x_1}}\left(x_1\right)\psi_{j,i_{x_2}}\left(x_2\right)\psi_{j,i_{x_3}}\left(x_3\right), & \mu = 7. \end{cases} \tag{5.39}$$

and

$$\phi_{j,i_{x_1},i_{x_2},i_{x_3}}\left(\boldsymbol{x}\right) \; = \; \phi_{j,i_{x_1}}\left(x_1\right)\phi_{j,i_{x_2}}\left(x_2\right)\phi_{j,i_{x_3}}\left(x_3\right), \tag{5.40}$$

where $\phi_{j,i}$ and $\psi_{j,i}$ are the 1D scaling function and the corresponding wavelet, respectively. Due to orthogonality, the scaling coefficients are given by $\bar{\boldsymbol{\omega}}_{0,0,0,0} = \langle\boldsymbol{\omega}, \phi_{0,0,0,0}\rangle$ and the wavelet coefficients by $\tilde{\boldsymbol{\omega}}^{\mu}_{j,i_{x_1},i_{x_2},i_{x_3}} = \left\langle\boldsymbol{\omega}, \psi^{\mu}_{j,i_{x_1},i_{x_2},i_{x_3}}\right\rangle$, where $\langle\cdot,\cdot\rangle$ denotes the L^2-inner product and μ corresponds to seven discrete directions in three dimensions.

The extraction algorithm can be summarized as follows:

1. Given $\boldsymbol{\omega}$, sampled on a grid $(x_{1_i}, x_{2_i}, x_{3_i})$ for $i, j, k = 0, N-1$ and the total enstrophy $Z = \frac{1}{2}\int|\boldsymbol{\omega}|^2 dx$.

2. Perform the 3D wavelet decomposition by applying the Fast Wavelet Transform (FWT) to each component of $\boldsymbol{\omega}$ to obtain the three components of $\tilde{\boldsymbol{\omega}}^{\mu}_{j,i_{x_1},i_{x_2},i_{x_3}}$ for $j = 0, J-1, i_{x_1}, i_{x_2}, i_{x_3} = 0, 2^{J-1}$, and $\mu = 1, ..., 7$.

3. Thresholding, where Z is the enstrophy and N the number of grid points,

$$T = \sqrt{\frac{4Z}{3}\ln N} \tag{5.41}$$

and split the coefficients $\tilde{\boldsymbol{\omega}}$ into

$$\tilde{\boldsymbol{\omega}}_{coh} = \begin{cases} \tilde{\boldsymbol{\omega}} & for \quad |\tilde{\boldsymbol{\omega}}| \geq T, \\ 0 & for \quad |\tilde{\boldsymbol{\omega}}| < T \end{cases} \quad \text{and} \quad \tilde{\boldsymbol{\omega}}_{inc} = \begin{cases} \tilde{\boldsymbol{\omega}} & for \quad |\tilde{\boldsymbol{\omega}}| < T, \\ 0 & for \quad |\tilde{\boldsymbol{\omega}}| \geq T \end{cases} \tag{5.42}$$

4. Perform the 3D wavelet reconstruction by applying the inverse FWT to compute $\boldsymbol{\omega}_{coh}$ and $\boldsymbol{\omega}_{inc}$ from $\tilde{\boldsymbol{\omega}}_{coh}$ and $\tilde{\boldsymbol{\omega}}_{inc}$, where *coh* and *inc* corresponds to coherent and incoherent. For the decomposition one FWT is performed for each component of the vorticity vector $\boldsymbol{\omega}$. To reconstruct the coherent vorticity $\boldsymbol{\omega}_{coh}$ in physical space one inverse FWT is required for each component. The incoherent vorticity vector is obtained by taking the difference between the total and the coherent vorticity in physical space. This yields in total six FWTs.

5.6 Application to the present Turbulent Rotating Channel Flow

To obtain more insight into the RDE and the corresponding structural effects the CVE method has been applied to six data sets (see Weller, Schneider, Oberlack & Farge (2006)) at a Reynolds number $Re_\tau = 180$ (table 5.1). At first for the non-rotating case and further for the rotating cases at five different rotation rates $Ro = 1, 3.2, 5.2, 10$ and 20. Table 5.1 gives an overview on the different computations, the flow domain and the corresponding interpolated grid points. In each case, the fluctuantions of a fully developed 3D instantaneous vorticity field were examined.

In the wavelet package, provided by our partners in France, orthogonal *Coiflet 12* wavelets are used, which have a filter length of twelve and four vanishing moments. The variable $c = 12$ denotes the length of the associated quadratic mirror filter (Daubechies 1992, Farge 1992). Coiflets are another variation on Daubechies wavelets. They are so named by I. Daubechies because R. Coifman suggested the construction of orthonormal wavelet basis with vanishing moment conditions both for φ as well as for ψ. The idea is to find the form of $m_0(\omega)$ that satisfies the orthogonality condition and both moment conditions for φ and ψ. These moment conditions are

$$\int_{-\infty}^{\infty} \oint \psi(t)dt = 0 \quad \text{for} \quad l = 0, 1, ..., N-1 \tag{5.43}$$

and

$$\int_{-\infty}^{\infty} \varphi(t) = 1, \quad \int_{-\infty}^{\infty} \oint \varphi(t)dt = 0 \quad \text{for} \quad l = 1, ..., N-1 \tag{5.44}$$

These two moment conditions translate into the following conditions on $m_0(\omega)$:

$$m_0^{(l)}(\pi) = 0 \quad \text{for} \quad l = 0, 1, ..., N-1 \tag{5.45}$$

and

$$m_0(0) = 1, \quad m_0^{(l)}(0) = 0 \quad \text{for} \quad l = 1, ..., N-1 \tag{5.46}$$

It can be shown that the following form of fulfills both the moment conditions given in eq. (5.45) and (5.46):

$$m_0(\omega) = \big(cos^2\frac{\omega}{2}\big)^K \Big[\sum_{k=0}^{K-1} \big(\frac{K-1+k}{k}\big)\big(sin^2\frac{\omega}{2}\big)^k + \big(sin^2\frac{\omega}{2}\big)^K f(\omega)\Big] \tag{5.47}$$

where $2K = N$ and $f(\omega)$ is chosen to be

$$f(\omega) = \sum_{n=0}^{2K-1} f_n e^{in\omega}. \tag{5.48}$$

The coefficients f_n are determined by requiring $m_0(\omega)$ given in eg. 5.47 to satisfy the orthogonality condition. For more details see Daubechies (1992). The scaling φ and wavelet ψ function is shown in fig. (5.2).

As a result, the operation count of the whole algorithm is $6Nc$ compared with $6Nlog_2N$ for the standard Fast Fourier Transform (FFT). This means that the FWT becomes faster than the FFT for $N > 2^c$. The choice of the threshold T (see eq. 5.41) is based on Donohos theorems (Daubechies 1992, Donoho & Johnstone 1994) and depends only on the total enstrophy Z and the number of grid points N, without any adjustable parameters.

Because the orthogonal wavelet decomposition requires that the number of grid points is a power of two in each direction, the vorticity fields have to be interpolated. The main problem is the Chebychev decomposition in the wall-normal direction used in the spectral code of the DNS, which makes a grid of a power of two impossible.

The utilized method for the interpolation is the *inverse distance* method, which is implemented in the visualization tool *tecplot* (Amtec Engineering 2003). In general

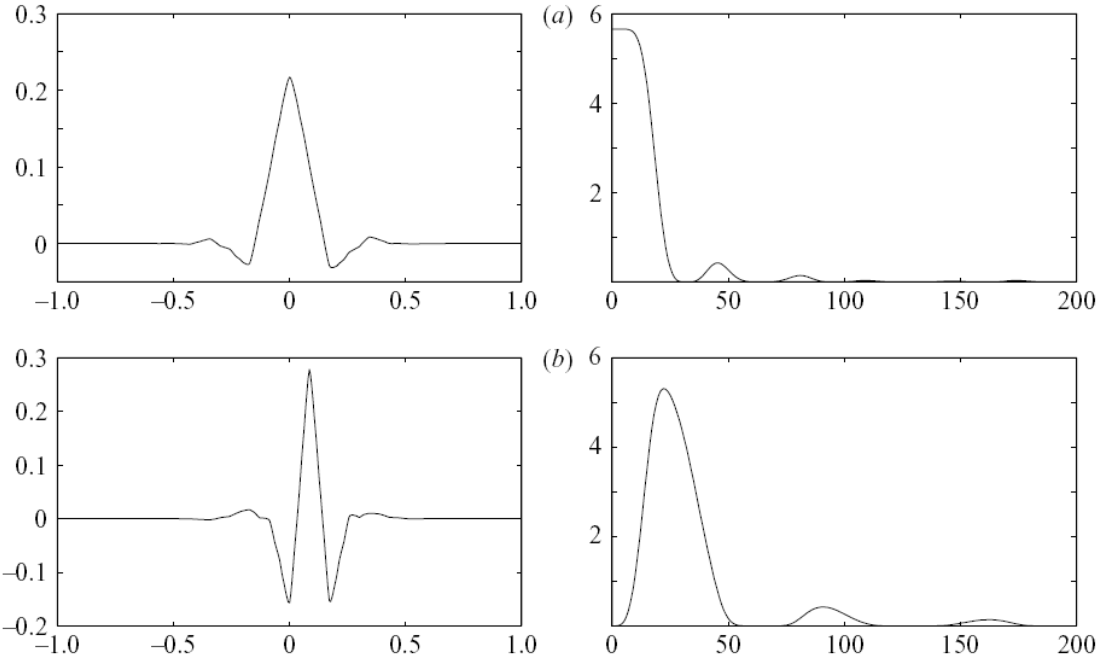

Figure 5.2: *Coiflet 12* wavelets: a) Scaling function ϕ in physical space (left) and spectral space (right) and b) Wavelet ψ in physical space (left) and spectral space (right).

it weights every grid point according to its distance from the sample point. The scheme can be written in the form:

$$F(P) = \frac{\sum_{i=1}^{n} \frac{F_i}{\|P-P_i\|^2}}{\sum_{i=1}^{n} \frac{1}{\|P-P_i\|^2}} \tag{5.49}$$

where P is the location of the sample point, $F(P)$ is the interpolated value at the sample point, P_i the location of the grid points, F_i are the grid point values, and $\|P - P_i\|^2$ represents the distance from P to P_i. For the non-rotating case and rotation rates 1, 3.2 and 5.2 the vorticity field was interpolated in physical space from a grid of $(128 \times 129 \times 128)$ to $(128 \times 128 \times 128)$ and for all other cases from $(256 \times 129 \times 128)$ to $(256 \times 128 \times 128)$.

Figures 5.3 - 5.5 show some results of the interpolation. For the comparison the data set at rotation rate $Ro = 20$ was selected because it exhibits most of the

Table 5.1: Computations at $Re_\tau = 180$ at interpolated grid.

Sim.	Ro	Box($L_1 \times L_2 \times L_3$)	Grid($N_1 \times N_2 \times N_3$)	Grid points
1	0	$4\pi \times 2 \times 2\pi$	$128 \times 128 \times 128$	2.1 Mio
2	1	$4\pi \times 2 \times 2\pi$	$128 \times 128 \times 128$	2.1 Mio
3	3.2	$4\pi \times 2 \times 2\pi$	$128 \times 128 \times 128$	2.1 Mio
4	5.2	$4\pi \times 2 \times 2\pi$	$128 \times 128 \times 128$	2.1 Mio
5	10	$8\pi \times 2 \times 4\pi$	$256 \times 128 \times 128$	4.2 Mio
6	14	$8\pi \times 2 \times 4\pi$	$256 \times 128 \times 128$	4.2 Mio
7	20	$8\pi \times 2 \times 4\pi$	$256 \times 128 \times 128$	4.2 Mio

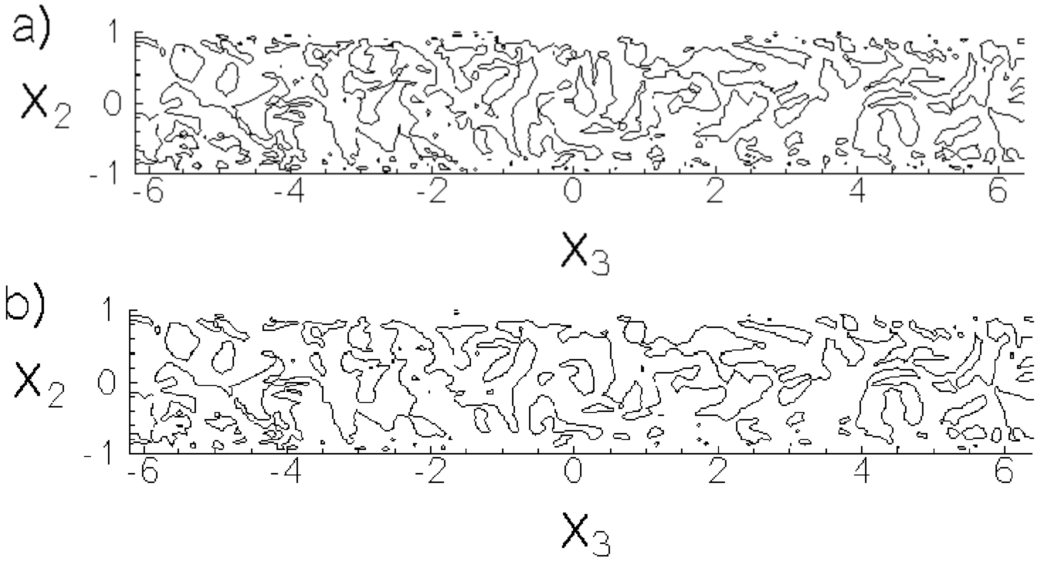

Figure 5.3: x_2x_3-slice: $x_1 = const.$ (middle of the channel) a) before and b) after interpolation .

coherent structures (see table 5.2). Besides for all plots the streamwise component is visualized since it represents the dominant part of the vorticity vector $|\boldsymbol{\omega}|$. Figures 5.3 and 5.4 show slices by the $x_2 - x_3$ and $x_1 - x_3$ levels, while figure 5.5 displays a top view of the isosurfaces of the 3D vorticity field. It is to be recognized that small structures are not completely dissolved and others are shown partly after the interpolation. However, the large coherent structures, which play the most important role in the further work, are fairly reconstructed.

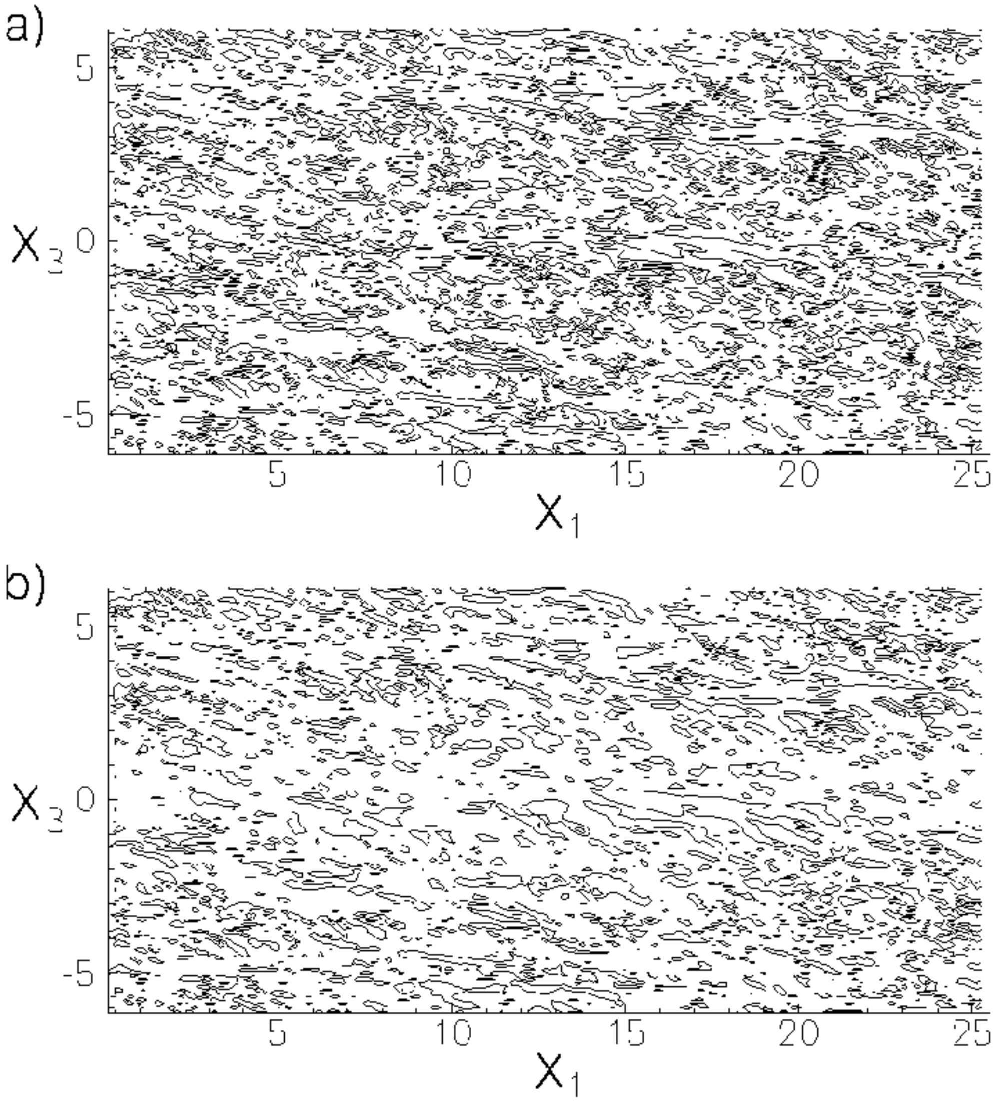

Figure 5.4: x_1x_3-slice: $x_2 = const.$ (wall-region) a) before and b) after interpolation .

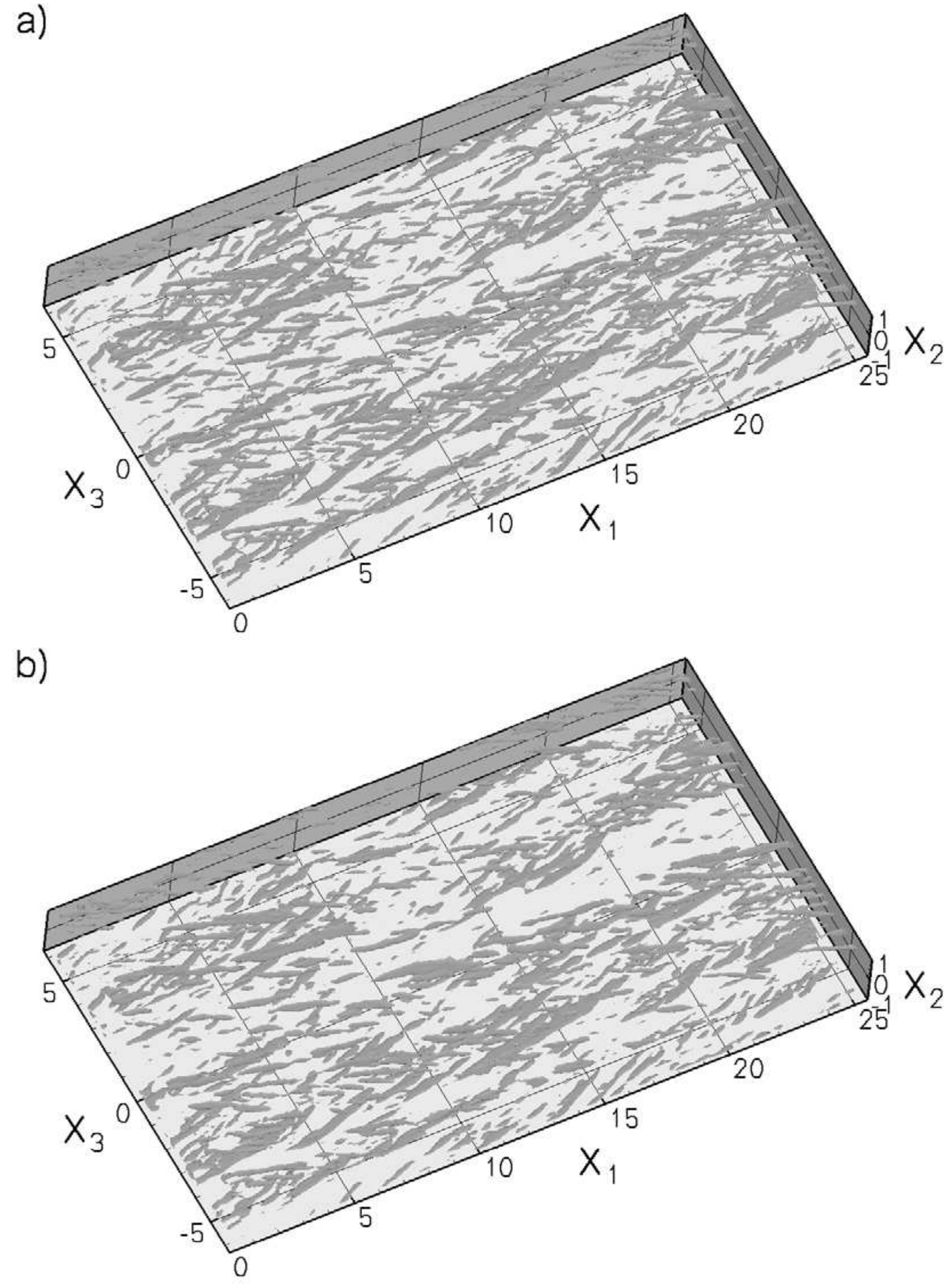

Figure 5.5: Isosurfaces of the streamwise vorticity field a) before and b) after interpolation at $\omega_x = \pm 2.4$.

5.7 Results of the CVE

5.7.1 Total, coherent and incoherent components of vorticity

The CVE software package, provided by our partners from France, was applied to the mentioned data sets (see table 5.1) to study coherent vortices and their statistics. In this frame the respective instantenous 3D vorticity fields were split in two parts namely the coherent and the incoherent component. The coherent part represents the coherent structures, while the incoherent part corresponds to incoherent structures, the so-called background flow.

In table 5.2 the rates of the coherent and incoherent components of the compression rate CR and the enstrophy Z are given for all rotation rates. The compression rate tells the number of coherent and respectively incoherent wavelet coefficients in percent of the particular component. Consequentially the compressin rate of the total field must be 100%. Compared to the non-rotating case the compression rate for the coherent structures is decreasing to a minimum at $Ro = 5.2$. At $Ro = 10$ the compression rate appears to revers it increases suddenly up to 3.46% and keeps on increasing monotonically for higher rotation rates. Figure 5.6 shows the percentage of wavelet coefficients corresponding to the coherent flow and the percentage of the coherent enstrophy which are plotted versus the rotation number.

Concerning enstrophy the values are inversely proportional to the compression rate (see fig. 5.7). For small rotation rates the coherent part increases compared to the non-rotating case and at $Ro = 10$ the enstrophy decreases down to 93.70%. This means that fewer coefficients retain more enstrophy, which might be interpreted as an increased coherency of the flow.

Table 5.2: Coherent and incoherent components of the compression rate CR and enstrophy Z at different rotation rates at $Re_\tau = 180$.

	Compression rate		Enstrophy	
Ro_τ	coherent[%]	incoherent[%]	coherent[%]	incoherent[%]
0	3.41	96.59	94.85	5.15
1	3.24	96.76	96.54	3.46
3.2	3.14	96.86	97.07	2.93
5.2	3.12	96.88	97.22	2.78
10	3.46	96.54	93.70	6.30
14	3.53	96.47	93.55	6.45
20	3.57	96.43	93.66	6.34

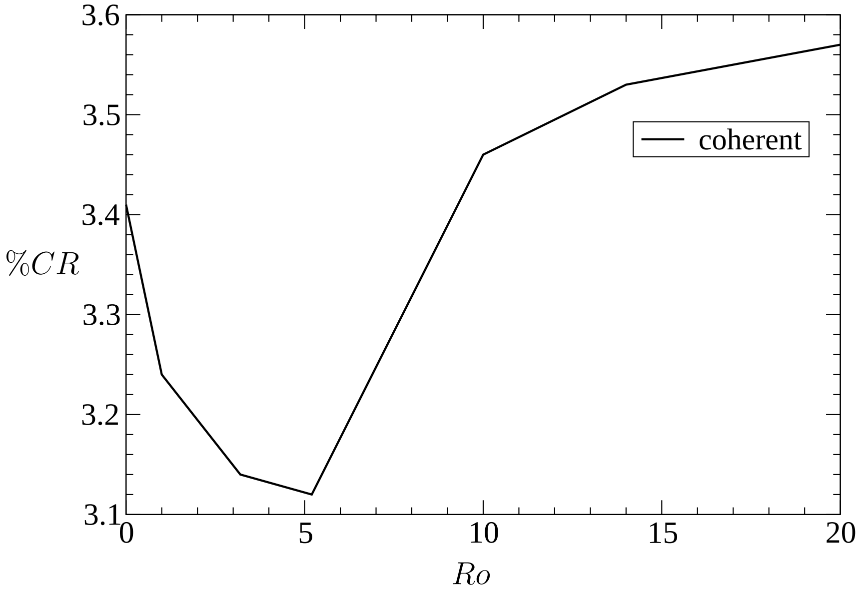

Figure 5.6: Compression rate CR as a function of the rotation rate.

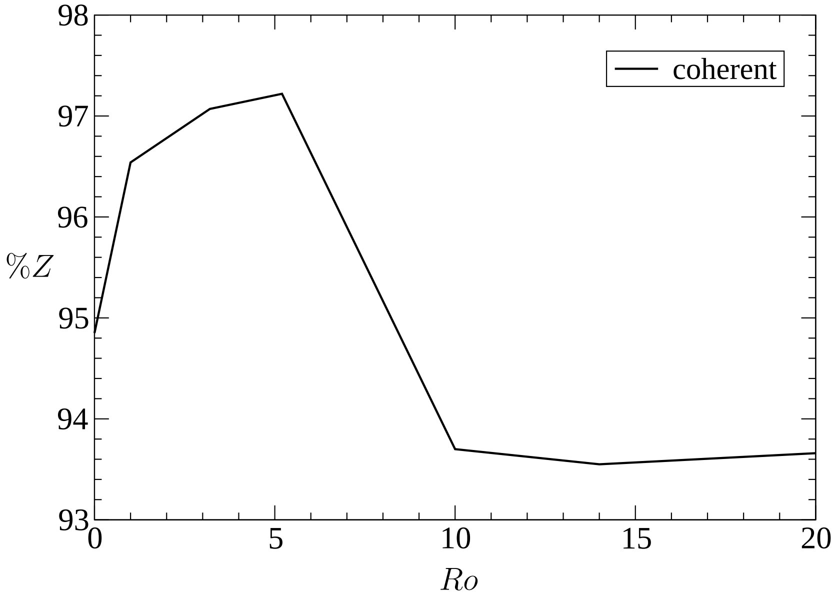

Figure 5.7: Coherent enstrophy Z as a function of the rotation rate.

Important to note that the RDE was found at about the same rotation rate where the curves of the compression rate and enstrophy reverse. This confirms a change in the flow dynamics for a specific Ro.

Figures 5.8 - 5.14 show the isosurfaces of a) the total, b) the coherent and c) the incoherent part of respectively an instantinous 3D vorticity field at different rotation rates. In every figure the isosurfaces of the modulus of $\boldsymbol{\omega'}$ are visualized at a fixed value. For all total fields and the coherent components $|\boldsymbol{\omega'}| = 2.6$ is used, while for the incoherent components amounts $|\boldsymbol{\omega'}| = 0.35$ was chosen.

For rotation rates up to $Ro = 5.2$ the whole channel is plotted, from $Ro = 10$ the box is four times larger. Therefore a quarter of the channel domain was extracted to have the same size of box and consequently to have the same zoom of the structures in every figure. Only this allows the direct comparison of the structures.

The different figures of the coherent structures look very similar. It seems that for increasing rotation rates the coherent structures are more and more diverted from the direction of motion. Unfortunately closer inspection cannot be determined in this view. More details will be given in figures (5.16) and (5.17) later on.

One more effect can be detected by the incoherent structures. From $Ro = 1$ up to $Ro = 5.2$ the incoherent wavelet coefficients are increasing, but at the same time less structures are visible than in figures (5.8), (5.12), (5.13) and (5.14). This means the vorticities are weaker in this region at $|\boldsymbol{\omega'}| = 0.35$.

To have a more detailed zoom of the coherent structures, a domain of $2\pi \times 0.24 \times \pi$ (a sketch is given in fig. (5.15) was extracted of every vorticity field near the wall region. Figure (5.15) displays a topview of the subzones by the $x_1 - x_3$-levels for the isosurfaces for every rotation rate also at $|\boldsymbol{\omega'}| = 2.6$. In general the diameter of the structures is growing up to $Ro = 5.2$, from $Ro = 10$ the structures become thinner.

The diversion of the structures due to increasing rotation rate is clearly visible in this figure. The diversion up to $Ro = 5.2$ seems to be marginally, but it becomes more and more significant at $Ro = 10, 14$ and 20. Further it was tempted to estimate the diversion angle α of the available subzones of fig. (5.15).

Illustration (5.16) shows the results at $Ro = 3.2, 5.2, 10$ and 14. In figure (5.17) the diverting averaged angle α between the orientation of coherent structures with the streamwise direction is plotted as a function of the rotation rate. Beetween $Ro = 5.2$ and $Ro = 10$ the gradient of the curve has a maximum.

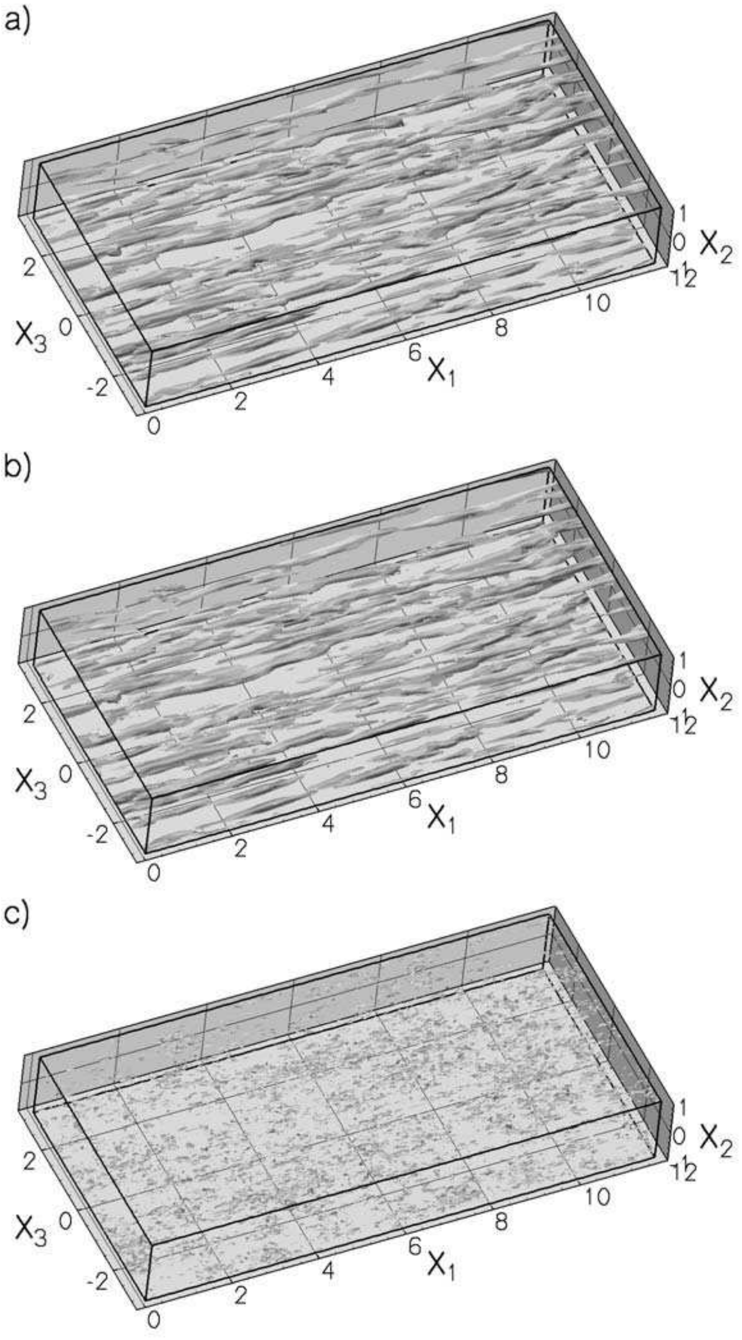

Figure 5.8: Isosurface of the vorticity field at $Ro = 0$: a) total field b) coherent component: 3.41% of the wavelet coefficients and c) incoherent component: 96.59% of the wavelet coefficients.

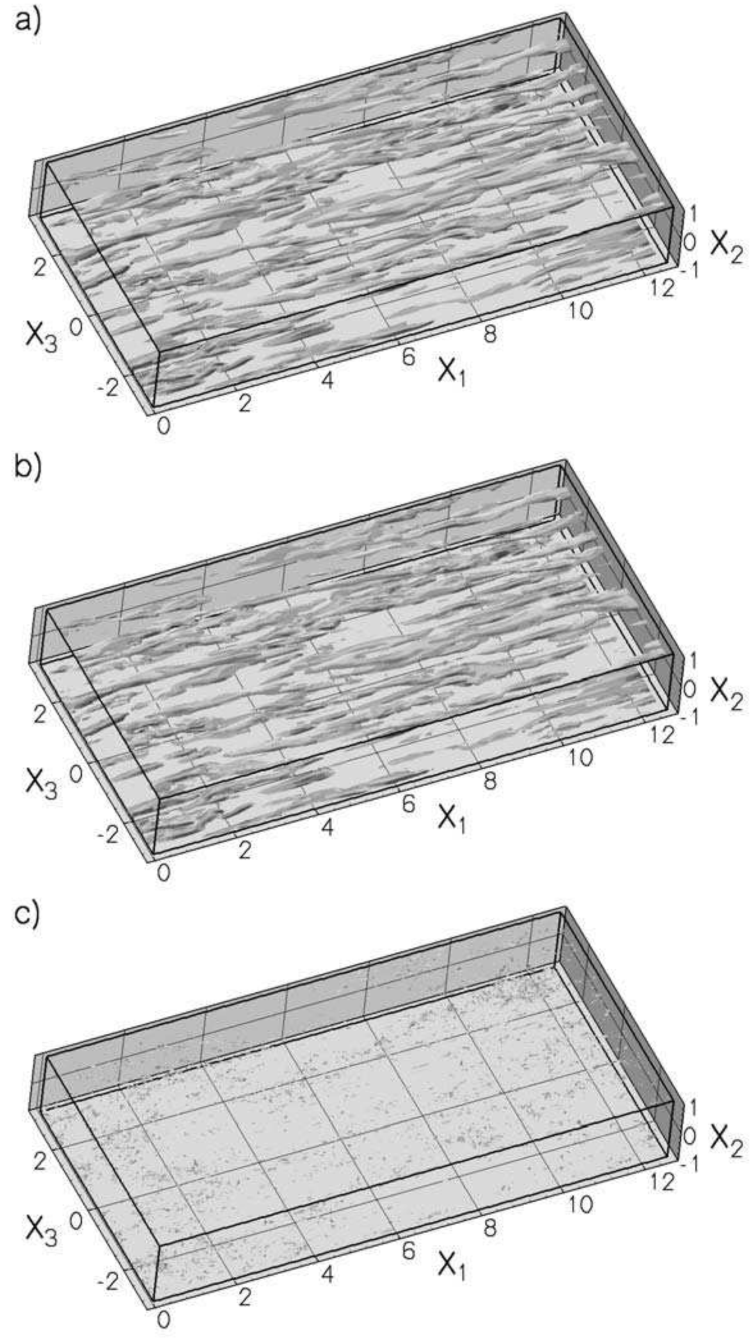

Figure 5.9: Isosurface of the vorticity field at $Ro = 1$: a) total field b) coherent component: 3.24% of the wavelet coefficients and c) incoherent component: 96.76% of the wavelet coefficients.

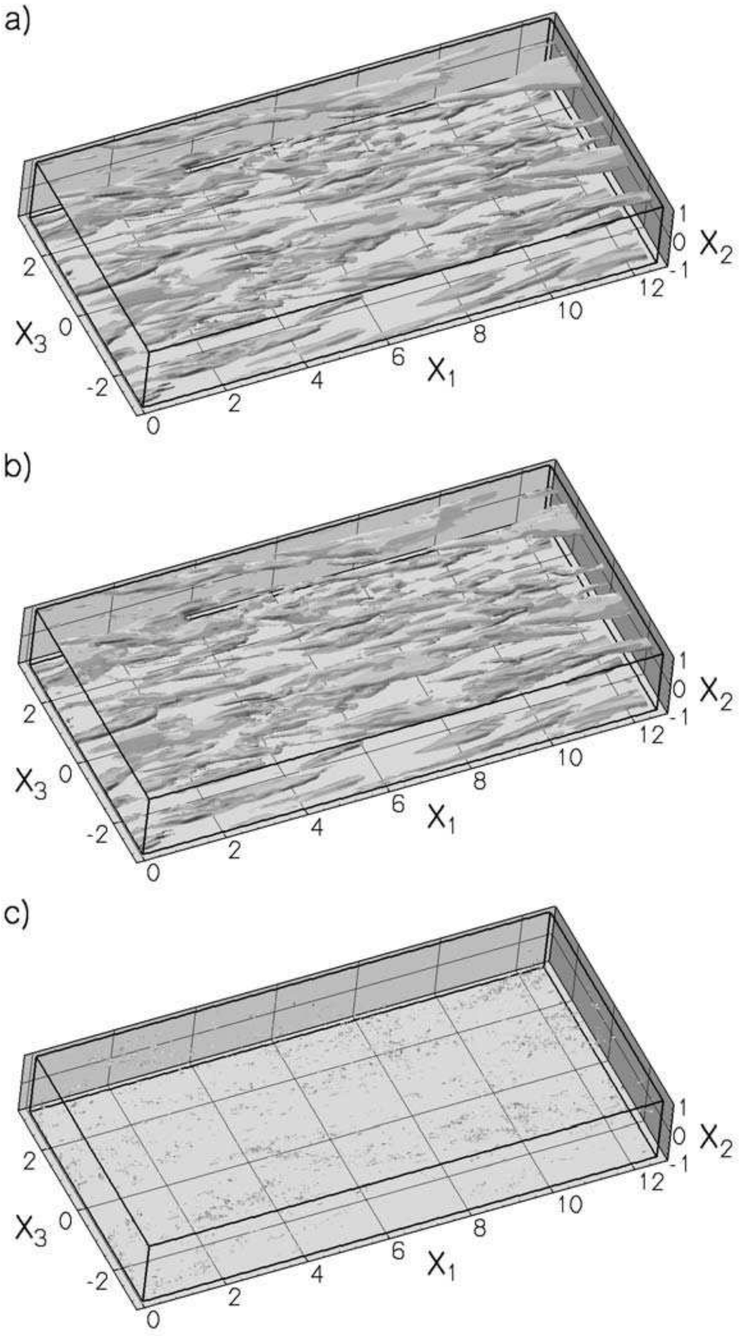

Figure 5.10: Isosurface of the vorticity field at $Ro = 3.2$: a) total field b) coherent component: 3.14% of the wavelet coefficients and c) incoherent component: 96.86% of the wavelet coefficients.

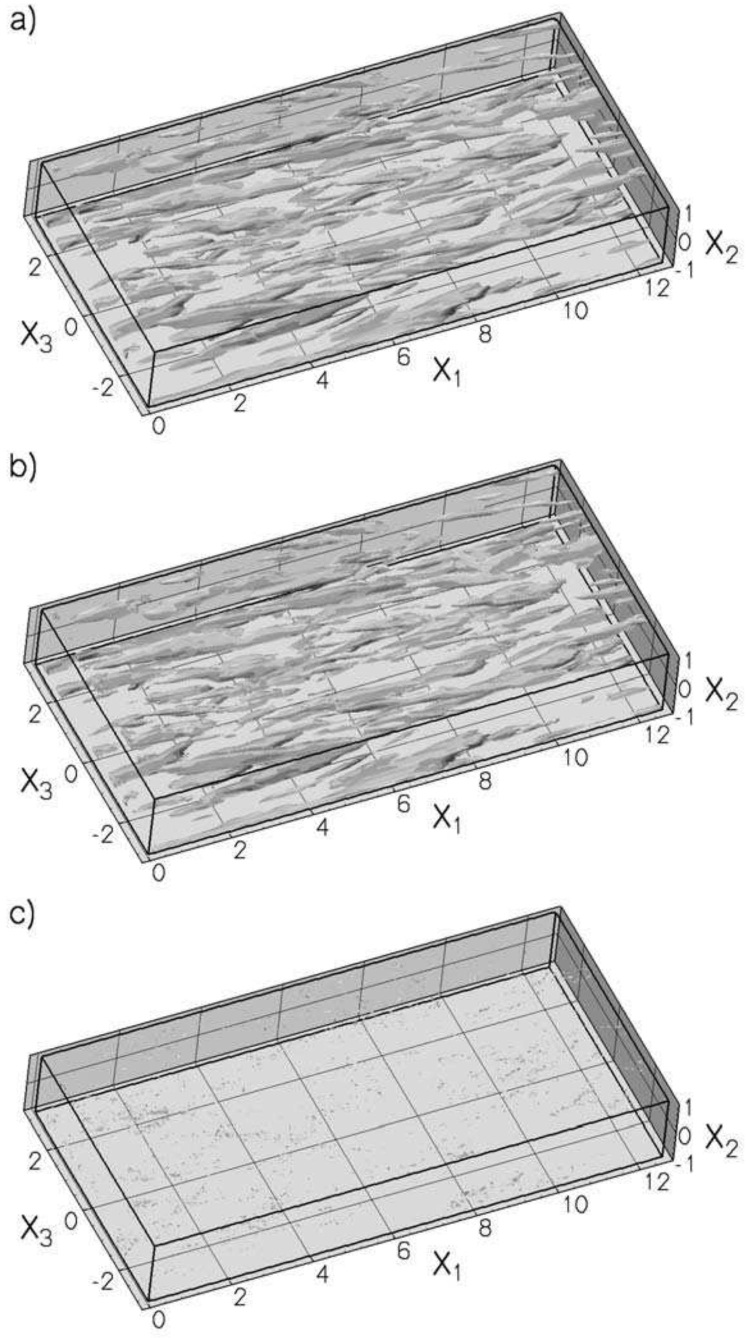

Figure 5.11: Isosurface of the vorticity field at $Ro = 5.2$: a) total field b) coherent component: 3.12% of the wavelet coefficients and c) incoherent component: 96.88% of the wavelet coefficients.

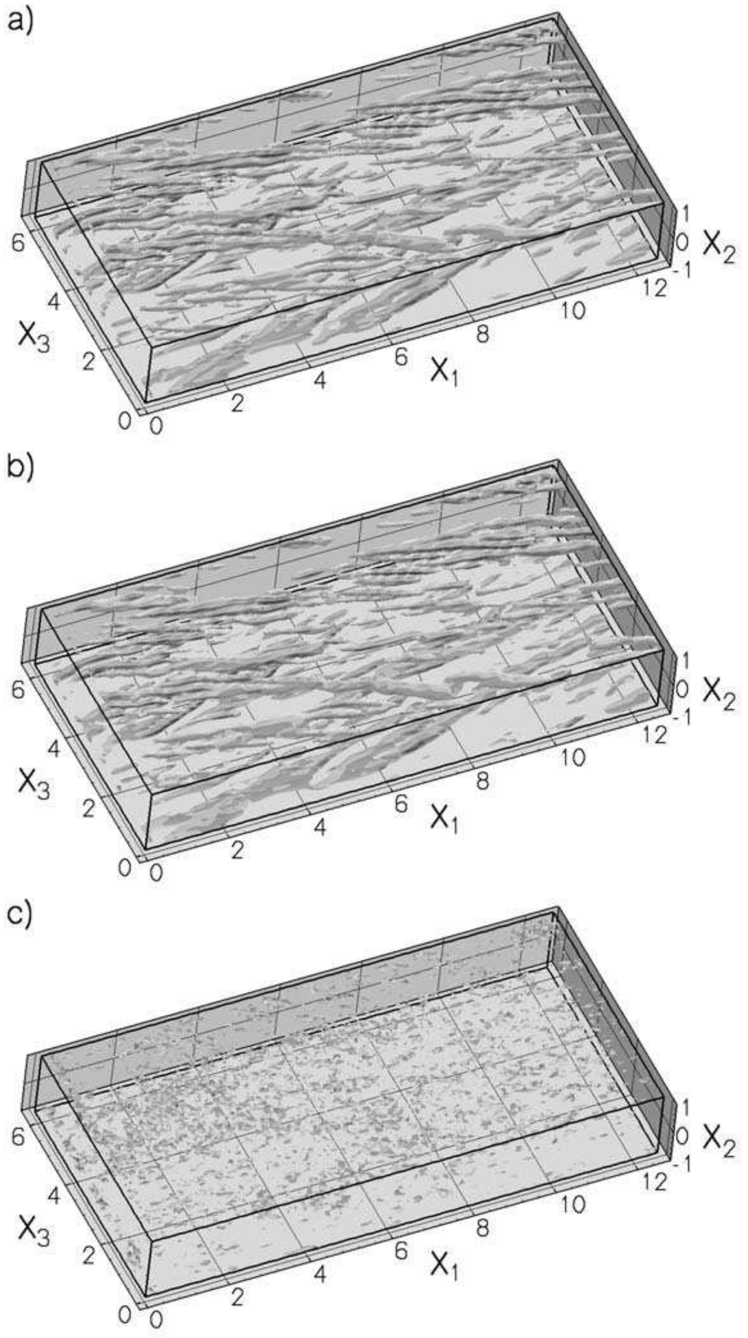

Figure 5.12: Isosurface of the vorticity field at $Ro = 10$: a) total field b) coherent component: 3.46% of the wavelet coefficients and c) incoherent component: 96.54% of the wavelet coefficients.

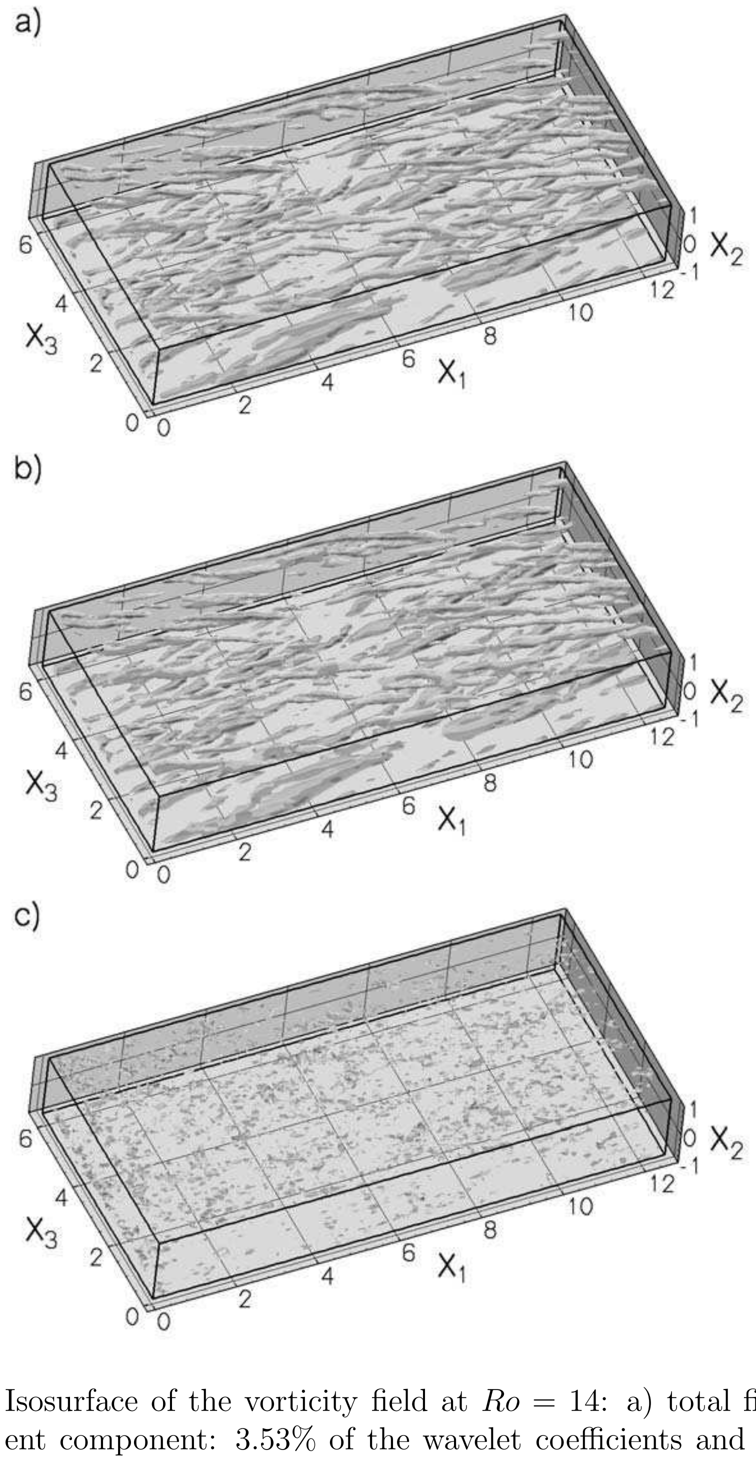

Figure 5.13: Isosurface of the vorticity field at $Ro = 14$: a) total field b) coherent component: 3.53% of the wavelet coefficients and c) incoherent component: 96.47% of the wavelet coefficients.

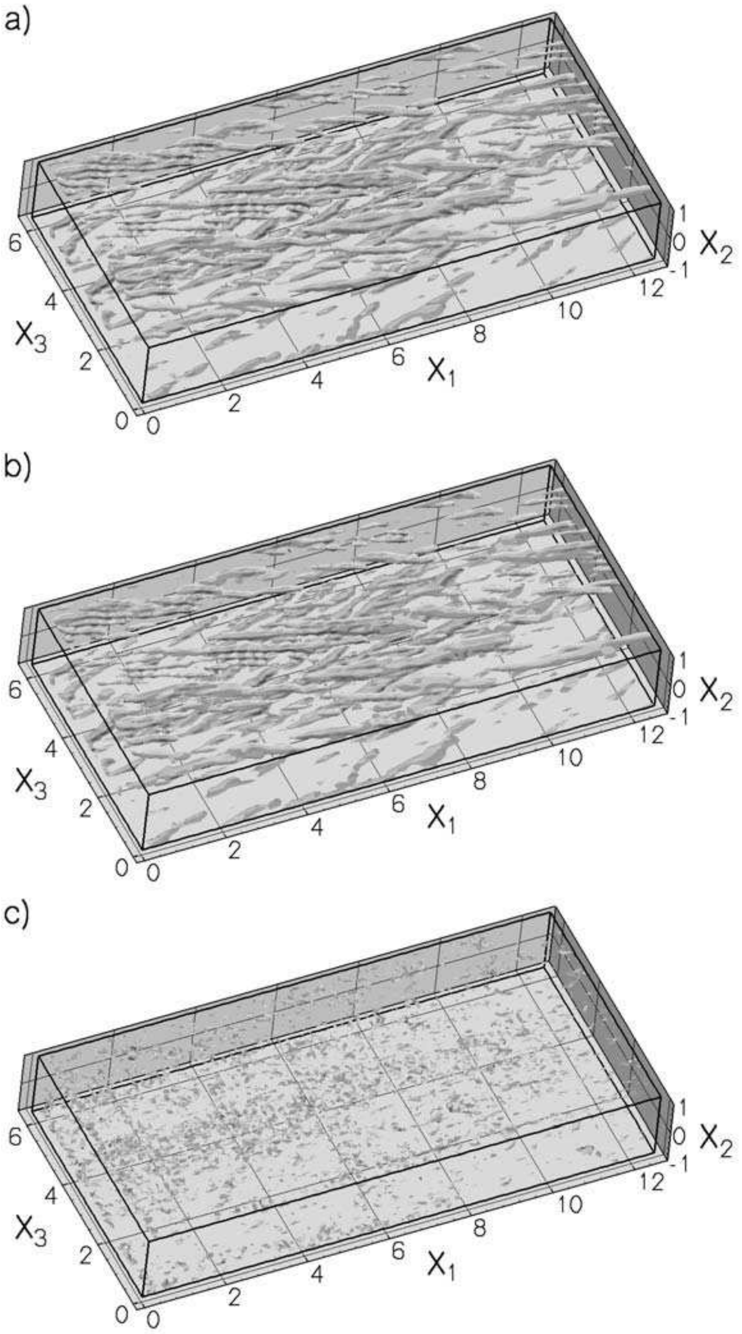

Figure 5.14: Isosurface of the vorticity field at $Ro = 20$: a) total field b) coherent component: 3.57% of the wavelet coefficients and c) incoherent component: 96.43% of the wavelet coefficients.

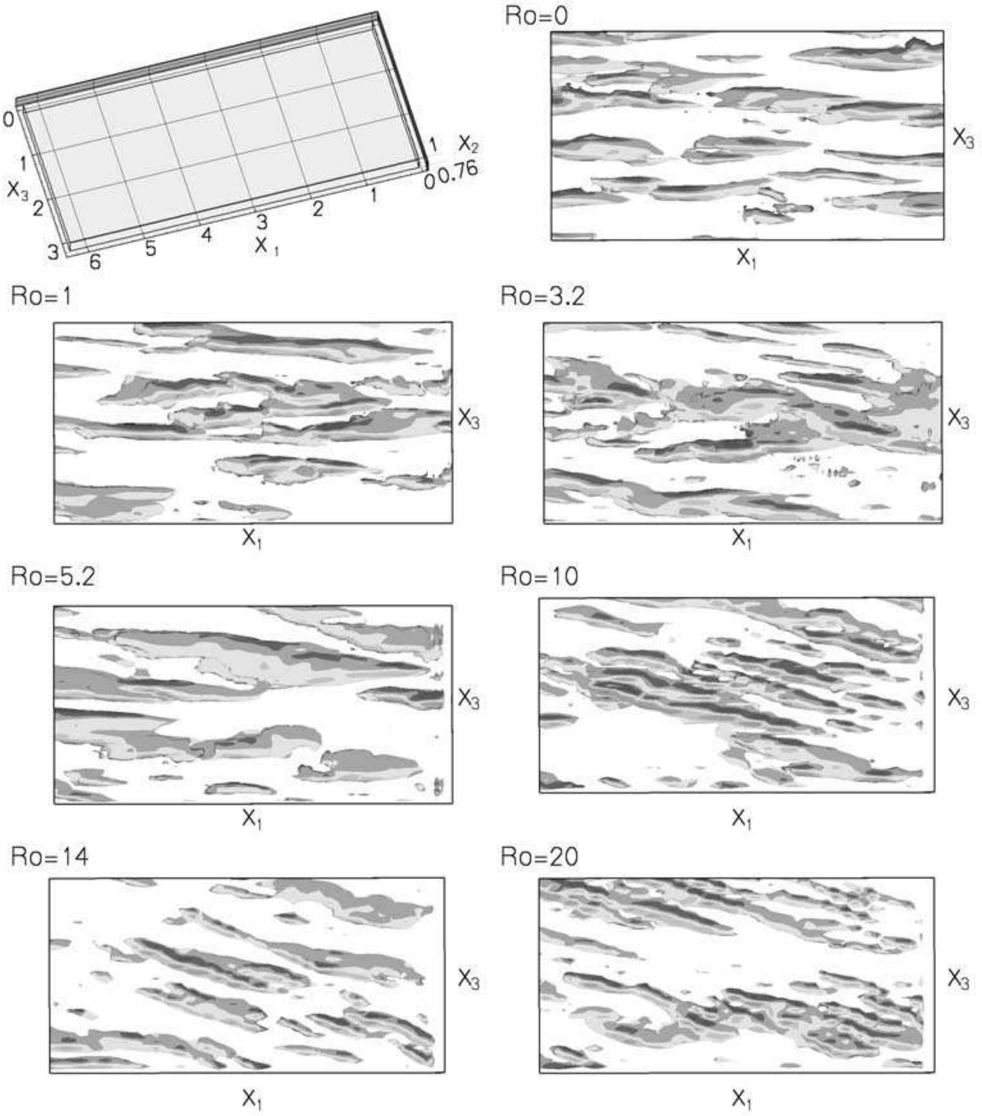

Figure 5.15: Topview of subzones by the $x_1 - x_3$-levels for the coherent components at different rotation rates. Each subzone has a size of $2\pi \times 0.24 \times \pi$.

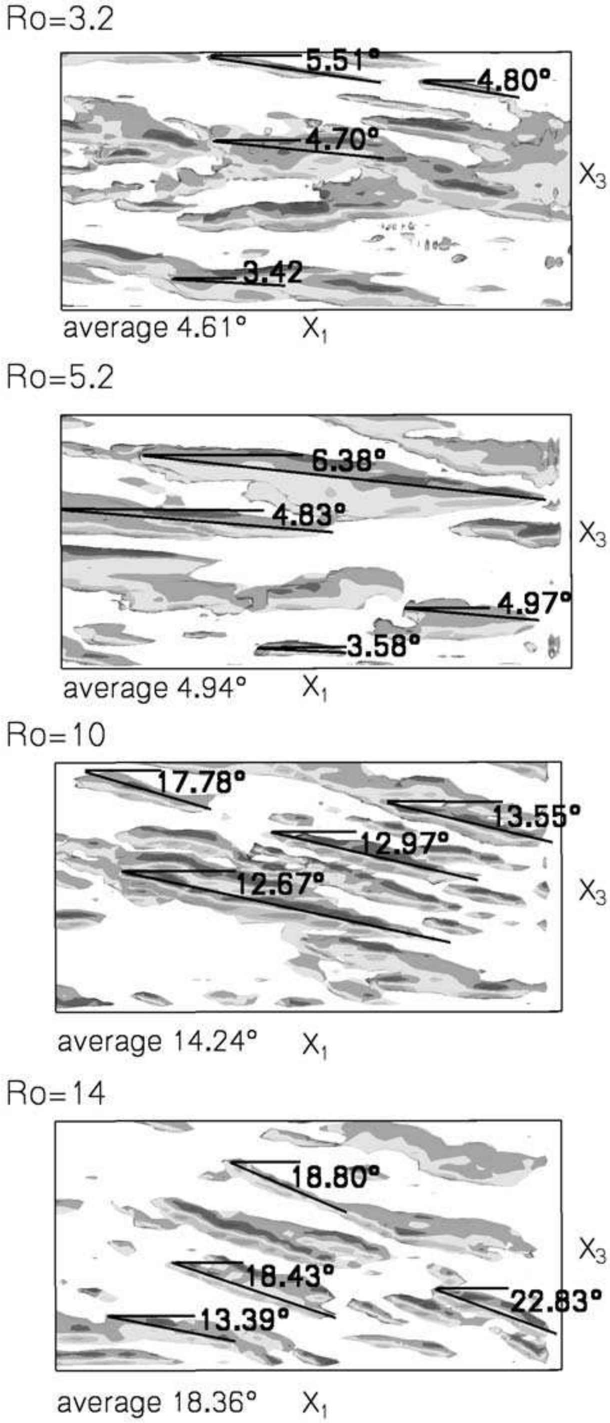

Figure 5.16: Topview of subzones by the $x_1 - x_3$-levels for the diverted coherent structures due to rotation. Each subzone has a size of $2\pi \times 0.24 \times \pi$.

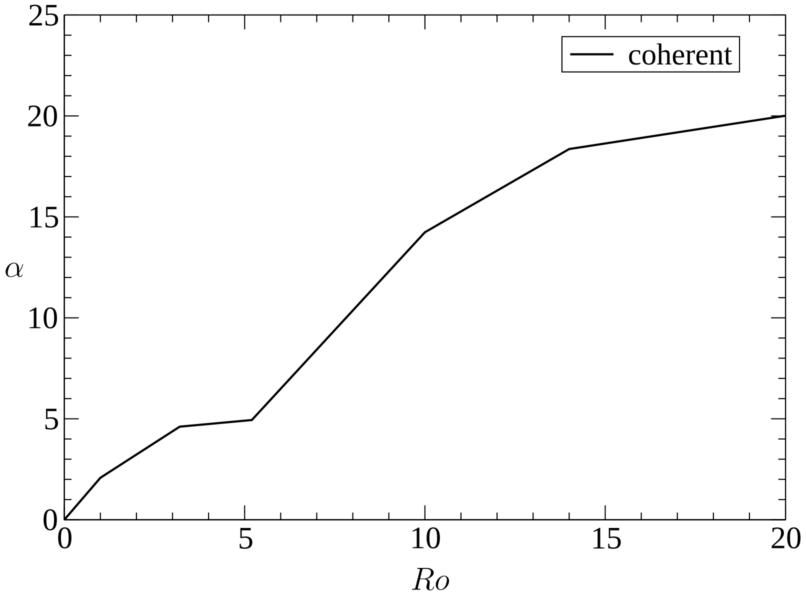

Figure 5.17: Diverting averaged angle α between the orientation of coherent structures with the streamwise direction as a function of the rotation rate.

5.7.2 Skewness and Flatness

Skewness characterizes the degree of asymmetry of a distribution around its mean. While the mean, standard deviation, and average deviation are dimensional quantities, that is, have the same units as the measured quantities ω'_j, the skewness is conventionally defined in such a way as to make it nondimensional. It is a pure number that characterizes only the shape of the distribution. The usual definition is

$$S(\omega'_1, ..., \omega'_N) = \frac{1}{N}\sum_{j=1}^{N}\left[\frac{\omega'_j - \omega'}{\sigma}\right]^3, \tag{5.50}$$

where σ is the distribution's standard deviation:

$$\sigma(\omega'_1, ..., \omega'_N) = \sqrt{Var(\omega'_1, ..., \omega'_N)}. \tag{5.51}$$

Var is the variance:

$$Var(\omega'_1, ..., \omega'_N) = \frac{1}{N-1}\sum_{j=1}^{N}(\omega'_j - \omega')^2. \tag{5.52}$$

A positive value of skewness signifies a distribution with an asymmetric tail extending out towards more positive ω'. A negative value signifies a distribution whose tail extends out more negative ω'.

The flatness is also a nondimensional quantity. It measures the relative peakedness of a distribution. A distribution with positive flatness is termed leptokurtic; the outline of the Matterhoern is an example. A distribution with negative flatness is termed platykurtic; the outline of a loaf of bread is an example. The conventional definition is

$$T(\omega'_1, ..., \omega'_N) = \left\{\frac{1}{N}\sum_{j=1}^{N}\left[\frac{\omega'_j - \omega'}{\sigma}\right]^4\right\} - 3, \tag{5.53}$$

where the -3 term makes the value zero for a normal distribution.

The skewness of the total, coherent and incoherent vorticity are depicted in figure 5.18. The total and the coherent skewness show a similar behavior, while the skewness of the incoherent vorticity is close to zero. Compared to the non-rotating case the skewness of the total and coherent vorticity is increasing up to $Ro = 3.2$. From $Ro = 3.2$ to $Ro = 5.2$ they decrease. Between $Ro = 5.2$ and $Ro = 10$ the curves exhibit a significant increase. At $Ro = 10$ the largest asymmetry of the distribution can be measured. Thereafter the curves decrease gradually.

Table 5.3: Skewness S and flatness T at different rotation rates.

	Skewness			Flatness		
Ro_τ	total	coherent	incoherent	total	coherent	incoherent
0	-0.09	-0.07	-0.02	33.71	36.18	6.72
1	0.09	0.11	-0.03	32.2	33.68	6.94
3.2	0.14	0.17	-0.03	32.6	33.93	7.31
5.2	0.01	0.02	-0.02	33.3	34.64	7.15
10	0.45	0.50	-0.01	44.77	48.79	6.73
14	0.30	0.33	-0.01	46.21	50.49	6.76
20	0.17	0.18	-0.01	50.86	55.67	6.99

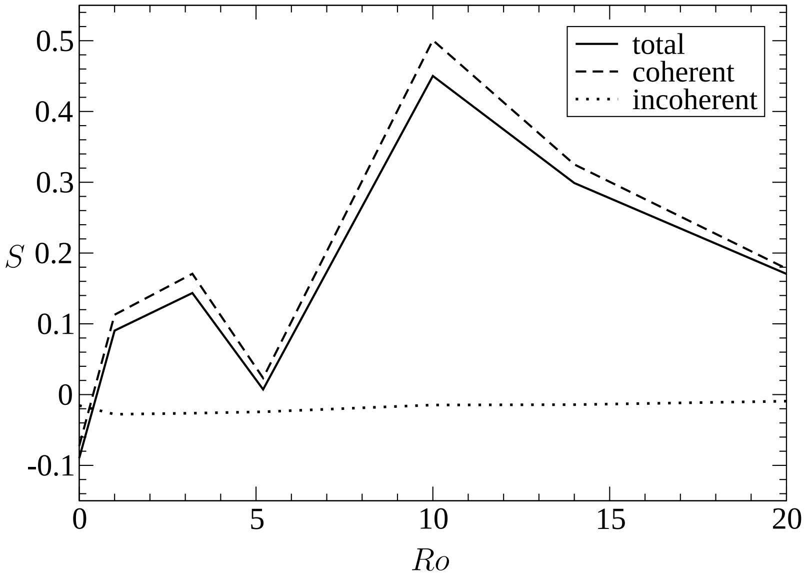

Figure 5.18: Skewness S for the total, coherent and incoherent vorticity as a function of the rotation rate.

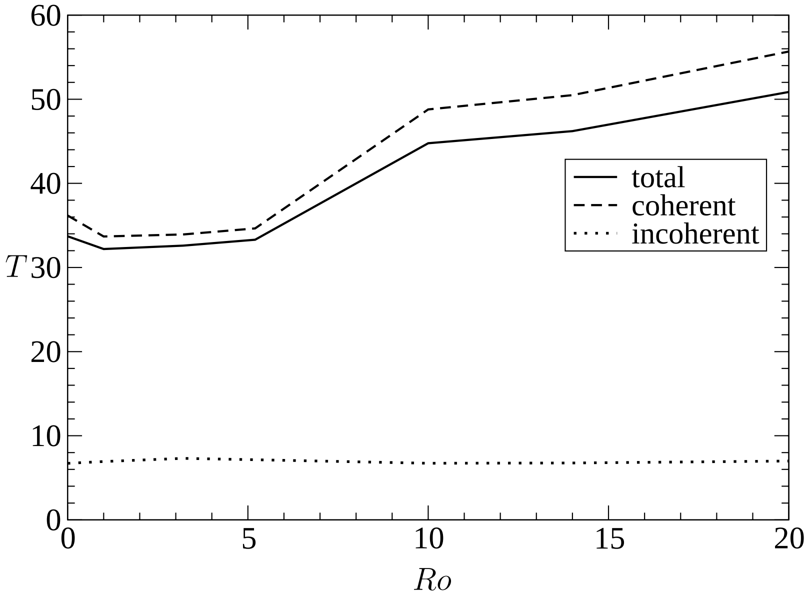

Figure 5.19: Flatness T for the total, coherent and incoherent vorticity as a function of the rotation rate.

In figure 5.19 the flatness of the total, coherent and incoherent vorticity are shown. The total and the coherent part are close to each other and the incoherent part is nearly constant with a value of 7. After a short decrease between $Ro = 0$ and $Ro = 3.2$ the total and coherent curve increase more and more. The largest gradient can be found beetween $Ro = 5.2$ and $Ro = 10$. In general the flatness for the total and coherent part is increasing with increasing rotation rate.

In table 5.3 the exactly values of skewness and flatness of the total, coherent and incoherent vorticity are given.

The significant increase in the skewness factors and the large gradient in the flatness are found in the same region, where the RDE was found. It confirms the assumption of a change in the flow dynamics.

6 Summary and Conclusions

In this thesis the influence of rotation about the streamwise direction of a turbulent channel flow was studied by using Lie group analysis and Direct Numerical Simulations. Additionally a wavelet analysis was applied to analyse coherent structures.

The turbulent channel flow rotating about the streamwise direction was studied only in recent years. First investigations in 1998 by Oberlack employing the symmetry group theory showed that there is a new turbulent scaling law related to the turbulent channel flow rotating about the mean flow direction. The induction of a cross flow in the spanwise direction is the most obvious difference compared to the classical case, rotation about the spanwise direction. Further it was shown that all six components of the Reynolds stress tensor are non-zero.

A Lie group analysis based on the two-point correlation equations was conducted. Invariant solutions were derived for the streamwise velocity $\bar{u}_1$, the predicted induced cross flow $\bar{u}_3$ and the Reynolds stress tensor $\overline{u_i'u_j'}$.

To verify these effects a Direct Numerical Simulation was performed. The influence of the rotation was studied at three different Reynolds numbers ($Re_\tau = 180$, 270 and 560) and at a variety of different rotation rates.
Both the cross flow and the fact that the six components of the Reynolds stress tensor are non-zero could be verified. Additional at $Re_\tau = 180$ a significant decay of the streamwise maximum velocity between $Ro = 5.2$ and 10 was noticed. At the same time the cross flow reaches a maximum at about $Ro = 10$ and then decreases for higher rotation rates Ro. For the shear stresses $\overline{u_1'u_3'}$ and $\overline{u_2'u_3'}$ the same effect such as for the spanwise mean velocity profiles was detected, it increases for small rotation rates and decreases for higher. These observations are called *rotation drag effect* (RDE).
Because it was not clear if the RDE is only a property of a rather lower Reynolds number $Re_\tau = 180$, further simulations at $Re_\tau = 270$ and 560 were conducted and analyzed. The results showed that the RDE is also noticeable at higher Reynolds numbers.

Additionally the results of the DNS at $Re_\tau = 180$ for the non-rotating case and three different rotation rates were compared to these of a corresponding experiment. The cross flow could be also observed in the experiment at RWTH Aachen.

In general the results are in good agreement, the same tendendies could be noticed.

Finally a wavelet analysis was performed to obtain more insight into the RDE and the corresponding structural effects. Therefore the *coherent vortex extraction* (CVE) method was applied to six selected three-dimensional DNS data sets at $Re_\tau = 180$.
The compression rate as well as the enstrophy of the coherent vorticity component show a noticeable reverse between $Ro = 5.2$ and 10. This tendency is supported by the skewness and the flatness of the coherent vorticity component.
Another effect of the rotation is that the structures are diverted from the streamwise direction. It was tempted to estimate this diversion angle at different rotations rates and to plot these as a function of the rotation rate. Beetween $Ro = 5.2$ and $Ro = 10$ the largest increase of the diversion angle was noticed. In general the results confirm the RDE.

7 Bibliography

ABE, H., KAWAMURA, H., MATSUO, Y. (2001): Direct Numerical Simulation of a Fully Developed Turbulent Channel Flow With Respect to the Reynolds Number Dependence. *Journal of Fluids Engineering 123(2)*, 382–393.

ALKISHRIWI, N., M., M., SCHRÖDER, W. (2006): Large-Eddy Simulation of rotating turbulent Channel Flow. *submitted to Comput. Fluids* .

AMTEC ENGINEERING, I. (2003): *Tecplot 10 - User's Manual.* Amtec Engineering, Inc., Bellevue, Washington.

BETA, C., SCHNEIDER, K., FARGE, M., BOCKHORN, H. (2003): Numerical study of the mixing of passive and reactive scalars in two-dimensional turbulent flows using orthogonal wavelet filters. *Chem. Eng. Sci. 58*, 1463–1477.

BLUMAN, G., ANCO, S. (2002): *Symmetry and integration methods for differential equations*, vol. 154 of *Applied mathematical sciences.* Springer-Verlag.

BLUMAN, G. W., KUMEI, S. (1989): *Symmetries and Differential Equations.* No. 81 in Applied Mathematical Sciences, Springer-Verlag.

BRADLEY, J., BRISLAWN, C., HOPPER, T. (1993): The FBI Wavelet/Scalar Quantization Standard for Gray-scale Fingerprint Image Compression. *Tech. Report LA-UR-93-1659, Los Alamos Nat'l Lab, Los Alamos, N.M.* .

CARMINATI, J., VU, K. (2000): Symbolic computation and differential equations: Lie symmetries. *J. Symbolic Comp. 29*, 95–116.

DAUBECHIES, I. (1988): Orthonormal bases of compactly supported wavelets. *Comm. Pure Appl. Math. 41*, 909–996.

DAUBECHIES, I. (1992): *Ten Lectures on Wavelets*, vol. 61 of *BMS-NSF Conference Series in Applied Mathematics.* SIAM.

DONOHO, D. (1993): Unconditional bases are optimal bases for data compression and statistical estimation. *Appl. Comput. Harmon Anal. 1*, 100–115.

DONOHO, D., JOHNSTONE, I. (1994): Ideal spatial adaption via wavelets shrinkage. *Biometrica 81*, 425–455.

Farge, M. (1992): Wavelet transforms and their application to turbulence. *Annu. Rev. of Fluid Mech. 24*, 395–457.

Farge, M., Pellegrino, G., Schneider, K. (2000): Coherent vortex extraction in 3D turbulence using wavelets. *Bull. of the Amer. Phys. Soc. 45-9.*

Farge, M., Pellegrino, G., Schneider, K. (2001a): Coherent vortex extraction in 3D turbulent flows using orthogonal wavelets. *Phys. Rev. Lett. 87(5)*, 0545011–0545014.

Farge, M., Schneider, K., Devynck, P. (2001b): Wavelet analysis and coherent structures extraction to study turbulent transport in confined hot plasmas. *Rapport interne, CEA-EURATOM, Cadarache* , 1–34.

Farge, M., Schneider, K., Kevlahan, N. (1999): Non-Gaussianity and coherent vortex simulation for two-dimensional turbulence using an adaptive orthonormal wavelet basis. *Phys. Fluids 11*, 2187–2201.

Farge, M., Schneider, K., Pellegrino, G., Wray, A., Rogallo, R. (2002): Coherent vortex extraction in 3D homogeneous isotropic turbulence: comparison between CVS and POD decompositions. *Phys. Fluids 15(10)*, 2886–2896.

Foias, C., Manley, O., Rosa, R., Temam, R. (2001): *Navier-Stokes Equations and Turbulence*, vol. 83 of *Encyclopedia of mathematics and its application.* Cambridge University Press.

Graps, A. (1995): An Introduction to Wavelets. *IEEE Computational Science and Engineering 2*, 1–18.

Grossmann, A., Morlet, J. (1984): Decomposition of Hardy functions into square integrable wavelets of constant shape. *SIAM J. Math. Anal 15*, 723–736.

Hart, J. (1971): Instability and secondary motion in rotating channel flow. *J. Fluid Mech. 45*, 341–351.

Hoyas, S., Jiménez, J. (2006): Scaling of the velocity fluctuations in turbulent channels up to Re_τ=2003. *Phys. Fluids 18*, 0011702.

Johnston, J., Halleen, R., Lezius, D. (1972): Effects of spanwise rotation on the structure of two-dimensional fully developed turbulent channel flow. *J. Fluid Mech. 56*, 533–557.

Kasagi, N., Tomita, Y., Kuroda, A. (1992): Direct numerical simulation of a passive scalar field in a turbulent channel flow. *Journal of heat transfer 114*, 598–606.

Kim, J., Moin, P., Moser, R. (1987): Turbulence statistics in fully developed channel flow at low Reynolds number. *J. Fluid Mech. 177*, 133–165.

Kristoffersen, R., Andersson, H. (1993): Direct simulations of low-Reynolds-number turbulent flow in a rotating channel. *J. Fluid Mech. 256*, 163–197.

Kuroda, A., Kasagi, N., Hirata, M. (1989): A direct numerical simulation of the fully developed turbulent channel flow at a very low Reynolds number. 3rd International Symposium on Computational Fluid Dynamics, Nagoya, Japan, 1174–1179.

Lundbladh, A., Henningson, D., Johansson, A. (1992): An efficient spectral integration method for the solution of the Navier-Stokes equations. Tech. Rep. FFA-TN 1992-28, Aeronautical Research Institute of Sweden, Bromma.

Mackenzie, D. (2001): Wavelets: Seeing the Forest and the Trees. *National Academy of Science - Beyond Discovery: The Path from Research to Human Benefit* , 1–8.

Mallat, S. (1989): A theory for multiresolution signal decomposition: The wavelet representation. *IEEE Trans. Patt. Anal. Mach. Intell. 11(7)*, 674–693.

Mallat, S. (1998): *A wavelet tour of signal processing*. Academic Press.

Moser, R., Kim, J., Mansour, N. (1999): Direct numerical simulation of turbulent channel flow up to $Re_\tau = 560$. *Physics of Fluids 11*, 943–945.

Oberlack, M. (1994): *Herleitung und Lösung einer Längenmaß- und Dissipations-Tensorgleichung für turbulente Strömungen.* PhD thesis, Inst. f. Techn. Mechanik, RWTH Aachen.

Oberlack, M. (1995): Analysis of the Two-Point Velocity Correlations in Turbulent Boundary Layer Flows. In: *Annual Research Briefs*, P. Moin, ed., Center for Turbulence Research, Stanford University/NASA Ames, CA, USA, 209–220.

Oberlack, M. (2000): *Symmetrie, Invarianz und Selbstähnlichkeit in der Turbulenz.* Habilitation, Inst. f. Techn. Mechanik, RWTH Aachen.

Oberlack, M. (2001): Unified Approach for Symmetries in Plane Parallel Turbulent Shear Flows. *J. Fluid Mech. 427*, 299–328.

Oberlack, M. (2002): *Symmetries and Invariant Solutions of Turbulent Flows and their Implications for Turbulence Modelling*, Springer Wien New York. 301–366.

Oberlack, M., Cabot, W., Petterson Reif, B., Weller, T. (2006): Group analysis, Direct Numerical Simulation and Modelling of Turbulent Channel Flow with Streamwise Rotation. *J. Fluid Mech. 562*, 383–403.

Oberlack, M., Cabot, W., Rogers, M. (1998): Group Analysis, DNS and Modeling of a Turbulent Channel Flow with Streamwise Rotation. Tech. Rep. 221-242, Studying Turbulence Using Numerical Databases – VII, Center for Turbulence Research, Stanford University/NASA Ames.

Oberlack, M., Guenther, S. (2003): Shear-free turbulent Diffusion - classical and new Scaling Laws. *Fluid Dyn. Res. 33*, 453–476.

Orlandi, P., Fatica, M. (1997): Direct Simulations of turbulent flow in a pipe rotating about its axis. *J. Fluid Mech. 343*, 43–72.

Orszag, S., Patterson Jr., G. (1972): Numerical Simulation of three-dimensional homogeneous isotropic turbulence. *Phys. Rev. Lett. 28*.

Pope, S. (2000): *Turbulent Flows*. Cambridge Unviversity Press.

Recktenwald, I., Weller, T., Schröder, W., Oberlack, M. (2006): Comparison of DNS and PIV data of turbulent channel flow rotating about the streamwise axis. *submitted to Phys. Fluids* .

Rotta, J. (1972): *Turbulente Strömungen*. Teubner, Stuttgart.

Schneider, K., Farge, M. (2003): Extraction of coherent vortex tubes in a 3D mixing layer. *Tubes, Sheets and Singularities in Fluid Dynamics, ed. K. Bajer and K.H. Moffatt, Kluwer* , 211–216.

Schneider, K., Farge, M., Pellegrino, G., Rogers, M. (2005): CVS filtering of 3D turbulent mixing layers using orthogonal wavelets. *J. Fluid Mech. 534(5)*, 39–66.

Schneider, K., Pellegrino, G., Farge, M., Rogers, M. (2003): CVS-filtered turbulent 3D mixing layers. *Bull. Amer. Phys. Soc. 48(10)*, 153.

Stephani, H. (1989): *Differential Equations: Their Solution Using Symmetries.* edited by Malcolm MacCallum, Cambridge University Press.

Tafti, D., Vanka, S. (1991): A numerical study of the effects of spanwise rotation on turbulent channel flow. *Phys. Fluids A 3*.

WELLER, T., OBERLACK, M. (2005a): DNS and Scaling Laws of a Turbulent Channel Flow with Streamwise Rotation. To appear in the Proc. of iTi Conference on Turbulence, Bad Zwischenahn, Germany.

WELLER, T., OBERLACK, M. (2005b): DNS of a turbulent channel flow with streamwise rotation -Investigations of the cross flow phenomena. To appear in the Proc. of Direct and Large-Eddy Simulation 6 (DLES6), Poitiers, France.

WELLER, T., OBERLACK, M. (2006): DNS of a Turbulent Channel Flow with Streamwise Rotation at Different Reynolds Numbers. CD Proc. Conference on Turbulence and Interactions (TI2006), Porquerolles, France, 1–4.

WELLER, T., RECKTENWALD, I., OBERLACK, M., SCHRÖDER, W. (2005): DNS and Experiment of a Turbulent Channel Flow with Streamwise Rotation - Study of the Cross Flow Phenomena. Proc. in Appl. Math. and Mech. (PAMM), Luxembourg , Luxembourg, 569–570.

WELLER, T., SCHNEIDER, K., OBERLACK, M., FARGE, M. (2006): DNS and Wavelet Analysis of a Turbulent Channel Flow Rotating about the Streamwise Direction. CD Proc. of the 5th Symposium on Turbulence, Heat and Mass Transfer (THMT-5), Dubrovnik, Croatia, 1–12.

WU, H., KASAGI, N. (2004): Effects of arbitrary directional system rotation on turbulent channel flow. *Physics of Fluids 16*, 979–990.

YOKOKAWA, M., ITAKURA, K., UNO, A., ISHIHARA, T., KANEDA, Y. (2002): 16.4-Tflops direct numerical simulation of turbulence by a Fourier spectral method on the Earth Simulator. Proc. of the 2002 ACM/IEEE Conference on Supercomputing, Baltimore, Maryland, 1–17.

Curriculum Vitae

Tanja Weller

Personal data:

Date of birth:	07. Mai 1972
Place of birth:	Mainz
Nationality:	German
Family status:	Single

Education:

07/78 - 06/82	Elementary school
07/82 - 06/91	Grammar school in Mainz Degree: Final secondary-school examinations - General qualification for university entrance

Studies:

10/91 - 09/93	Electrical engineering at the Technische Universität Darmstadt
10/93 - 06/99	Civil engineering at the Technischen Universität Darmstadt Intermediate examination: Intermediate diploma Degree: Diploma

Occupational activity:

08/99 - 05/01	Research assistant at the Technische Universität Darmstadt Department of Civil Engineering Section of Engineering Hydrology and Water Management
06/01 - 05/03	Research assistant at the Computer Graphics Center (ZGDV) Department of Visual Computing
06/03 - present	PhD student at the Technische Universität Darmstadt Department of Mechanical Engineering Chair of Fluid Dynamics